DYNAMICS OF LMC CLUSTERS

By

Philippe Fischer B.Sc., M.Sc.

A Thesis

Submitted to the Faculty of Graduate Studies

in Partial Fulfillment of the Requirements

for the Degree

Doctor of Philosophy

McMaster University

October 1992

DOCTOR OF PHILOSOPHY (1992) McMASTER UNIVERSITY
(ASTROPHYSICS) Hamilton, Ontario

TITLE: Dynamics of LMC Clusters

AUTHOR: Philippe Fischer
B.Sc. (McMaster University)
M.Sc. (University of Victoria)

SUPERVISOR: Dr. D. L. Welch

NUMBER OF PAGES: XIII,160

ABSTRACT

The dynamics of three populous Large Magellanic Cloud (LMC) star clusters, NGC 1866, NGC 1978, and NGC 1850, have been examined using a combination of BV charge-coupled device (CCD) images and high-precision radial velocities of individual member stars. This study represents the first dynamical analysis of LMC clusters employing individual radial velocities of sufficient precision to sample the cluster velocity dispersions. Abstracts for each cluster are presented below.

NGC 1866

V-band CCD images of the young LMC cluster NGC 1866 out to a projected radius R $\sim$ 100 pc were obtained using the 1.0m telescope at Las Campanas. In addition, radial velocities with a mean precision of 1.0 km s^{-1} were measured for 69 member supergiants using the echelle spectrograph on the 2.5m telescope.

The luminosity profile is well described by a power-law. The total cluster luminosity is $L_{V\infty} = 6.5 \pm 0.3 \times 10^5$ L$_\odot$. A star-subtracted, median-filtered U frame was used to determine photometric shape parameters. In the region $4 \leq R$ (pc) ≤ 12, the cluster has a mean ellipticity of $\epsilon = 0.17 \pm 0.06$ and a minor axis position angle $\alpha = 125° \pm 5°$. The stellar radial velocities indicate that NGC 1866 has a systemic velocity of $v_{ave} = 301.2 \pm 1.0$ km s^{-1} and is rotating around an axis at a position angle of 100$\pm$25° with a peak velocity of 1.3 $\pm$0.5 km s^{-1}. A comparison of the derived values for NGC 1866 and the theoretical $v_o/\sigma_o - \epsilon$ relationship indicates that the observed flattening is consistent with rotation. The cluster mass was determined using a maximum likelihood estimator to compare the observed radial velocities to various orbital models yielding $M_\infty = 1.25$ and $1.35 \pm 0.25 \times 10^5$ M$_\odot$ and $M/L_V = 0.19 - 0.21 \pm 0.04$ M$_\odot$/L$_\odot$ for models with and without a rotational component, respectively. This technique has been used to determine the nature of the orbital

anisotropies and to justify the addition of the rotation term to the cluster velocity field. The quality of the fits for models with rotation is clearly superior to those without and isotropic orbits agree best with the data in both cases. Depending on the actual age of the cluster, the best estimate for the average slope of the mass function is $x = 1.3 \pm 0.15$ ($\tau = 2.0 \times 10^8$ years) or $x = 1.82 \pm 0.1$ ($\tau = 1.0 \times 10^8$ years).

NGC 1978

BV CCD images of the elliptical LMC cluster NGC 1978 out to a projected radius R $\sim$ 100 pc were obtained using the 1.0m telescope at Las Campanas. In addition, radial velocities with a precision of 1.5 km s^{-1} were measured for 35 member giants using the echelle spectrographs and 2D-Frutti detectors on the Las Campanas 2.5m and the Cerro Tololo 4.0m telescopes.

After star-subtraction and median-filtering the ellipticity of the surface brightness distribution was determined to be $\epsilon = 0.30 \pm 0.03$ and the major axis position angle to be PA $= 152 \pm 7°$. The stellar radial velocities indicate that NGC 1978 has a systemic velocity of $\overline{v} = 293.3 \pm 1.0$ km s^{-1}. NGC 1978 appears to be several times older than its central relaxation time but considerably younger than its half-mass relaxation time.

Single and multi-mass anisotropic King-Michie models and single-mass rotating and non-rotating oblate spheroid models were fitted to both the surface luminosity profiles and the radial velocity data. The total cluster luminosity is $L_B = 3.1 - 3.7 \pm 0.2 \times 10^5$ $L_{B\odot}$ and $L_V = 3.0 - 3.5 \pm 0.2 \times 10^5$ $L_{V\odot}$ (for an assumed LMC distance of 50 kpc), where the range results from different model extrapolations of the brightness profile. The multi-mass models, while very effective at constraining the central mass-to-light ratios (hereafter, M/L's) at about $(M/L)_0 = 0.13 \pm 0.06$ $M_\odot/L_\odot$,

yielded global M/L's which ranged over a factor of 5; M/L = 0.3 - 1.5 $M_\odot/L_\odot$ for a sample of mass function slopes. The best agreement between population and dynamical M/L's is seen for the cases $x = 0.0$ for the B band [$(M/L)_0 = 0.14 \pm 0.06$ $M_\odot/L_{B\odot}$ and M/L = 0.35 ± 0.15 $M_\odot/L_{B\odot}$] and $x = 0.5$ for the V [$(M/L)_0 = 0.13 \pm 0.06$ $M_\odot/L_{V\odot}$ and M/L = 0.40 ± 0.15 $M_\odot/L_{V\odot}$]. The single-mass models tended to give better agreement with the luminosity profiles but produced M/L's (i.e. M/L = 0.20 ± 0.08 $M_\odot/L_{V\odot}$) that were difficult to reconcile with simple population studies without invoking a rather high low-mass cut-off (i.e. 0.8 $M_\odot$).

We found no significant differences between the M/L's derived with oblate spheroid models and those derived with spherical models. While the non-rotating (anisotropic) models were in better agreement with the kinematic data, it was impossible to completely rule out the rotating models. As well, there is no morphological evidence for a merger.

<center>NGC 1850</center>

In this thesis we have examined the age and internal dynamics of the young binary LMC cluster NGC 1850 using BV CCD images and echelle spectra of 52 supergiants.

Isochrone fits to a BV color-magnitude diagram revealed that the primary cluster has an age of $\tau = 90 \pm 30$ Myr while the secondary member has $\tau = 6 \pm 5$ Myr. The reddening was found to be E(B-V)=0.17 mag. BV surface brightness profiles were constructed out to R > 40 pc, and single-component King-Michie (KM) models were applied. The total cluster luminosity varied from $L_B = 2.60$ - 2.65 $\times 10^6$ $L_{B\odot}$ and $L_V = 1.25$ - 1.35 $\times 10^6$ as the anisotropy radius varied from infinity to three times the scale radius with the isotropic models providing the best agreement with the data. Simple tests were made to check for tidal truncation in the

profiles and we concluded that there was slight evidence favoring truncation. The bright background and binary nature of NGC 1850 render this conclusion somewhat uncertain.

Of the 52 stars with echelle spectra, a subset of 36 were used to study the cluster dynamics. The KM radial velocity distributions were fitted to these velocities yielding total cluster masses of 5.4 - 5.9 $\pm 2.4 \times 10^4$ $M_\odot$ corresponding to $M/L_B = 0.02 \pm 0.01$ $M_\odot/L_{B\odot}$ or $M/L_V = 0.05 \pm 0.02$ $M_\odot/L_{V\odot}$. A rotational signal in the radial velocities has been detected at the 93% confidence level implying a rotation axis at a position angle of 100°. A variety of rotating models were fit to the velocity data assuming cluster ellipticities of $\epsilon = 0.1 - 0.3$. These models provided slightly better agreement with the radial velocity data than the KM models and had masses that were systematically lower by a few percent.

Values for the slope of the mass function were determined using the derived M/L, theoretical mass-luminosity relationships, and several forms for the IMF. The preferred value for the slope of a power-law IMF is a relatively shallow, $x = 0.29$ $^{+0.3}_{-0.8}$ assuming the B-band M/L or $x = 0.71$ $^{+0.2}_{-0.4}$ for the V-band.

ACKNOWLEDGEMENTS

First I would like to acknowledge the huge contribution of Doug Welch to this thesis. His generosity, in terms of data, time, ideas, and grant money are unprecedented in my experience. Simply put, this thesis would not have been possible without his impetus and it was a pleasure to collaborate with him. Secondly I would like to acknowledge the contribution of Mario Mateo which was also essential to the success this project. I am also greatly appreciative of the generous allocations of observing time made by the LCO TAC and the hospitality of the observatory staff.

I would like to thank my office mates over the years for their tolerance: Steve Butterworth, Steve Holland, He Nan, Yuemin Qian, Pat Côté, Pat Durrell, Mark Walker, Jeff Secker, and Dean McLaughlin. I would further like to thank Pat Côté for interesting and entertaining conversations even if he is sadly misinformed on so many topics (i.e. hockey, baseball, politics, and music).

I greatly appreciate the support my family has always given me in all my endeavors even if they were as poorly conceived as the pursuit of a Ph.D. in astronomy. I would like to acknowledge Angela Punnett for being a great friend.

Finally I thank the office staff, especially Marg and Wendy for steering me through the bureaucracy.

Further acknowledgements can be found at the ends of chapters 2, 3, and 4, corresponding to specific contributions.

TABLE OF CONTENTS

TABLE OF CONTENTS *(Continued)*

TABLE OF CONTENTS (Continued)

LIST OF FIGURES

LIST OF FIGURES (Continued)

LIST OF TABLES

LIST OF TABLES (Continued)

Chapter 1

1.1 Dynamics of LMC Clusters

The populous clusters of the Large Magellanic Cloud (LMC) are much more varied than are the Galactic globular clusters (GGCs). Unlike the clusters in the Galaxy which are uniformly old (ages of typically $\tau = 15$ Gyr) and round (the largest ellipticity is $\epsilon = 0.1$) the LMC clusters range from less than 100 Myr to ages comparable with the GGCs, and have projected ellipticities as high as $\epsilon = 0.3$ (Geisler and Hodge 1980). An interesting aspect of the cluster age distribution is that it does not appear to be a continuum. There are approximately eight old (i.e.

> 10 Gyr) clusters and a large number of clusters younger than 3 Gyr, indicating at least two major epochs of star formation interrupted by a more quiescent period (Olszewski *et al.* 1991). A possible explanation is that interactions have occurred between the Small Magellanic Cloud (SMC) and the LMC in the past which have initiated bursts of star formation (Murai & Fujimoto 1980).

It is these differences in the cluster populations which have motivated this study; the LMC clusters provide potentially new insights not available through the study of the GGCs. The young LMC clusters represent a unique opportunity to study the internal dynamics of rich, resolved stellar systems in which the current ages are substantially less than the two-body relaxation timescales. This information is crucial for gaining an understanding of cluster formation and early evolution. The GGCs have had most of the information regarding their initial conditions erased.

Stellar evolution is not as far advanced as in the GGCs meaning there is a much larger mass range for stars on the main sequence. Coupled with substantially less cluster dynamical evolution, owing to both the younger age and the weaker tidal field of the LMC, the LMC clusters offer a significant advantage as probes of the initial stellar mass function (IMF). Photometric attempts to understand the IMF in the GGCs and particularly in the LMC clusters are greatly complicated by the faintness and crowding of the stars. Current photometry, with a few noteworthy exceptions, rarely extends below 0.5 $M_\odot$. Furthermore, it is not yet possible to obtain photometry for the stellar remnants (i.e., white dwarfs, neutron stars, black holes), which must exist in the clusters. This is especially problematic when one considers that the unseen components play a highly significant role in cluster dynamics and evolution. One of the best means of probing these fainter members is through the use of kinematic observations. Even though kinematic measurements can only be

obtained for the brightest cluster members, one is still seeing the contribution of the
faint objects to the clusters' gravitational potentials, and it is, therefore, possible
to infer and constrain their density distributions.

The high ellipticities seen in both the young and old clusters are an intrigu-
ing puzzle. Three possible causes are: rotation, mergers, and orbital anisotropy.
Dynamical analyses, in particular through the use of the $v_0/\sigma - \epsilon$ relation (Binney
1978), should allow us to distinguish between these possibilities, and the solution
will have interesting repercussions on our understanding of the evolution of both
the LMC and Milky Way cluster systems.

The study of LMC cluster dynamics is currently in its infancy. To date (includ-
ing work done for this thesis) there ·:ave been several dynamical studies of LMC
clusters including integrated spectra for several old and intermediate age clusters:
NGC 1835 in Elson and Freeman (1985) and Dubath *et al.* (1991); NGC 1786,
NGC 1835, NGC 1916, NGC 2005, and NGC 2019 in Mateo *et al.* (1991) and NGC
1978 in Meylan *et al.* (1991). Individual stellar radial velocity measurements of
intermediate-age clusters: NGC 1783 in Mateo *et al.* (1991), NGC 1978 in Seitzer
(1991) and Fischer *et al.* (1992b). And individual velocity measurements for young
clusters: NGC 1866, NGC 2164, and NGC 2214 in Lupton *et al.* (1989); NGC 2157
in Mateo *et al.* (1991); and NGC 1866 and NGC 1850 in Fischer *et al.* (1992a and
1993).

1.2   History of Cluster Dynamics

Attempts to understand cluster dynamics began with the use of radial star-
counts in order to derive surface density profiles (SDPs). These studies date back
to Bailey (1915) and the subsequent modelling by Jeans (1916). A renaissance in

this field occurred in the 1960's with the formulation and application of the King-Michie (KM) models (King 1966, Michie 1963). These models were a simple physical description of the the globular cluster distribution function which took into account both a tidal cut-off imposed by the Galaxy and anisotropy in the stellar orbits. The most obvious simplification was the assumption that all stars were of equal mass and hence that the mass-to-light ratio (M/L) was radially invariant. Despite this, the models appeared to fit many globular cluster SDPs very well, at least in the radial regimes in which starcounts could be obtained.

That all was not well with the single-mass KM models became increasingly apparent when SDPs with larger dynamic ranges became available. One such case was the SDP of M3 which deviated significantly from the best fit single-mass KM model (Da Costa and Freeman 1976). This motivated those authors to derive multi-mass models based upon the isotropic King models. These models divided the stellar mass spectrum into a number of mass classes (typically 10) and assumed equipartition of energy in the cluster core which drives mass segregation in the sense that low mass stars tend to migrate to larger cluster-centric radius. This results in a mass-to-light ratio which varies as a function of radius. The model was extended to the anisotropic regime in the seminal work of Gunn and Griffin (1979).

Thus far I have only discussed the modeling of SDPs without any kinematic information. While this allows one to constrain the cluster distribution function it does not allow for determinations of the cluster mass. Aside from several early studies employing low dispersion spectra of cluster giants (M92 - Wilson & Coffeen 1954, Schwarzschild & Bernstein 1955, ω Cen - Dickens & Woolley 1967, and 47 Tuc - Feast & Thackeray 1960), the first precise kinematic study of Galactic globular clusters (GGCs) was conducted by Illingworth (1976) for 10 southern objects. He

used integrated light spectra of the cluster cores in order to determine central velocity dispersions for NGC 104, NGC 362, NGC 1851, NGC 2808, NGC 6093, NGC 6266, NGC 6388, NGC 6441, NGC 6715, NGC 6864. He was thus able to scale the single-mass King velocity dispersion profiles and derive total cluster masses which lay in the range $0.17 - 1.1 \times 10^6$ $M_\odot$ corresponding to $M/L_V = 0.9$ - 2.9 in solar units. It should be noted that integrated central velocity dispersions can only be used as a means of scaling a projected profile determined by other means (i.e., a KM model of the SDP). They cannot be modeled dynamically and therefore do not yield further insight into the the dynamical state of the cluster other than its mass. Significantly, it neglects the possibility that the kinematics might differ from the model owing to poor assumptions about the form of the distribution function (i.e., such as neglecting cluster rotation or a significant dark matter component). These differences, while having only subtle effects on the SDP, may have much larger effects on the kinematics. The use of integrated spectra also made it impossible to deal with the possibility of binary and field star contamination, both of which tend to systematically bias the inferred velocity dispersion too high.

This situation was improved with the appearance of the first globular cluster study employing a large sample of high-precision (1 km s^{-1}) radial velocities of individual cluster giants (Gunn & Griffin 1979). This study utilized 144 measurements of 111 stars, which, while not particularly useful as a constraint on the dynamics, did indeed show a downturn in the dispersion as a function of radius as expected from the SDP. They were also able to quantify the cluster rotation (dynamically insignificant in this case) and did not find any binaries.

A summary of 'published' studies employing high-precision measurements of individual cluster members can be found in Table 1.1. This table will require revision in the very near future as the use of multi-object spectrographs combined with

Table 1.1
Dynamically-Studied Milky Way Clusters

Cluster	N	Ref.
NGC 104	272	7
NGC 288	30	5
NGC 362	212	8
NGC 3201	421	9
NGC 3201	91	10
NGC 5139	318	6
NGC 5139	950	14
NGC 5139	118	15
NGC 5272	111	2
NGC 5466	25	5
NGC 5466	13	12
NGC 6121	23	12
NGC 6205	136	16
NGC 6397	11	1
NGC 6397	127	11
NGC 6624	19	4
NGC 6626	23	4
NGC 6656	13	12
NGC 6681	17	4
NGC 6838	17	12
NGC 6809	21	5
NGC 7078	120	13
NGC 7078	102	17
NGC 7089	69	3

Notes: 1 Da Costa *et al.* 1977, 2 Gunn & Griffin 1979, 3 Pryor *et al.* 1986, 4 Pryor *et al.* 1989, 5 Pryor *et al.* 1991, 6 Meylan 1987, 7 Meylan 1988, 8 Welch *et al.* 1993, 9 Côté *et al.* 1993, 10 Da Costa *et al.* 1993, 11 Meylan & Mayor 1991, 12 Peterson & Latham 1986, 13 Peterson *et al.* 1989, 14 de Zeeuw *et al.* 1993, 15 Seitzer 1983, 16 Lupton *et al.* 1987, 17 Gebhardt *et al.* 1993.

echelle gratings and low-noise CCDs has caused a revolution in the field (i.e. see NGC 5139 and NGC 3201 in Table 1.1).

An alternative to radial velocities are proper motions of cluster members. Until recently this data has been of too low quality for meaningful dynamical analyses. A proper motion dynamical analysis of NGC 6205 has appeared in a preprint (Leonard

et al. 1992) based on the proper motion data of Cudworth & Monet (1979). The authors claim that the proper motion data provides a much tighter constraint on the cluster mass than the radial velocity study of Lupton *et al.* (1987b). In principle, one can derive dynamical parameters (i.e. orbital anisotropy) with fewer assumptions from proper motion studies as these yield two independent velocity dispersion profiles as needed to solve the Jeans equation. Two problems are 1) the current proper motion studies are not yet sufficiently precise to sample the cluster velocity dispersion, and 2) it is very difficult to determine proper motions in the crowded central regions of the cluster. The first problem may soon be resolved, claims of proper motions precise to 3 km s^{-1} have been reported (de Zeeuw *et al.* 1993), while the second may require HST observations with baselines of ten years or so.

As we can see, the kinematic data are currently going through a period of great improvement. The SDPs as well, are experiencing many benefits from the use of large format CCDs. This improvement in the data naturally demands an improvement in the modeling. Currently, KM models, while providing an adequate snapshot view of the globular cluster, do not really yield much physical insight. Furthermore, there is a class of globular clusters, the post core-collapse clusters, for which the KM models are completely inadequate. At best, they provide a common set of parameters by which globular clusters can be compared. A more sophisticated approach involves Fokker-Planck modeling of the cluster evolution. In this way, one can attempt to derive the dynamical effects which play a leading role in the cluster evolution, such as the presence of primordial binaries, the formation of binaries later on, the role of the Galactic tidal field, stellar evolution, evaporation, etc. It is possible to follow the evolution right to the core-collapse phase and beyond. Some recent examples of the application of Fokker-Planck models to clusters are: M71 in Drukier *et al.* (1992), and M15 and NGC 6624 in Grabhorn *et al.* (1992).

1.3   Division of Labour

The thesis is arranged as follows: chapters two, three, and four are reprints of three papers on the clusters NGC 1866, NGC 1978, and NGC 1850, respectively. These papers appeared in the Astronomical Journal (NGC 1850 was in press at the time of this writing) and the bibliography is as follows:

P. Fischer, D.L. Welch, P. Côté, M. Mateo, and B.F. Madore 1992, "Dynamics of the Young LMC Cluster NGC 1866", Astronomical Journal, 103, 857-870.

P. Fischer, D.L. Welch, and M. Mateo 1992, "Dynamics of the Intermediate-Age Elliptical LMC Cluster NGC 1978", Astronomical Journal, 104, 1086.

P. Fischer, D.L. Welch, and M. Mateo 1992, "Dynamics of the Young Binary LMC Cluster NGC 1850", submitted to Astronomical Journal.

1.3.1   NGC 1866

The original telescope proposal to study the dynamics of NGC 1866 was written by Dr. Welch and Dr. Madore in the fall of 1988. The first observing run occurred at Las Campanas Observatory (LCO) in Dec. 1988 and was carried out by Dr. Welch, Dr. Mateo, and Mr. Côté. The data was reduced in early 1989 by Dr. Welch and Mr. Côté. A subsequent observing run at LCO, attended by Dr. Mateo, took place in Nov. - Dec 1989. I joined the collaboration in Jan 1989. I reduced all the data from the 1989 run and partially re-reduced the 1988 run. I also reduced most of the photometric data used in the analysis. All subsequent analysis and writing was carried out by me. The paper was edited by all of the listed co-authors.

1.3.2   NGC 1978

I was the principal investigator on the CTIO observing proposal for the NGC 1978 observing run. The co-investigators were Dr. Welch and Dr. Mateo. The CTIO observing run was attended by Dr. Welch and me. Subsequent observing was carried out at LCO by me. Thereafter, I did all the data acquisition, data reduction (photometric calibration provided by Dr. Mateo), analysis and writing.

1.3.3   NGC 1850

The radial velocity data was obtained over two observing runs, the first by me in Jan. - Feb. 1991 and the second in Dec 1991 by Dr. Mateo. Photometry data from a Jan. 1991 run attended by Dr. Welch and me was also used. All the data reduction (photometry calibrations provided by Dr. Welch), analysis, and writing was carried out be me.

Chapter 2

2.1 INTRODUCTION

Globular clusters present an attractive dynamical challenge to observational astronomy. They are very nearly spherically symmetric and are highly resolved out to distances of ~ 100 kpc allowing spectroscopy of individual stars and a detailed analysis of the internal dynamics. Through these observations one can extract details of the cluster velocity field including velocity dispersions, rotation, and the degree of orbital anisotropy. Another goal of such work is to derive dynamical

masses and mass-to-light (M/L) ratios which are important probes of star formation and evolution. In the Milky Way, these studies can be broken down into two subsets: 1) those which utilize measurements of central radial velocity dispersions from integrated spectra (c.f., Illingworth 1976), and 2) radial velocity measurements of individual member stars (c.f., Gunn and Griffin 1979, Meylan and Mayor 1986, Lupton, Gunn, and Griffin 1987, Pryor, McClure, Fletcher, and Hesser 1989 and others). The latter method is favored (assuming individual stars can be resolved right into the core) as it allows for an analysis of the radial distribution of the cluster velocity dispersion and rotation.

The Large Magellanic Cloud (LMC) clusters can supply two types of information not available from studies of their Milky Way counterparts. Unlike the Galactic globulars, the LMC clusters are not uniformly old (i.e., $\tau \sim 10^{10}$ years); its cluster population is dominated by much younger objects. Many are younger than their central relaxation times and hence the stellar orbits should be relatively unchanged since the time of star formation. Theoretical models have shown that after several relaxation times have passed most information about the initial velocity distribution has been wiped out (Spitzer and Thuan 1972). Hence, LMC clusters may be the only practical targets where initial dynamical conditions can be observed. Secondly, because of the larger range in stellar masses on the LMC cluster main sequences it should be possible to derive slopes for the initial mass functions (IMFs) much more reliably than is possible for Galactic globular or sparse open clusters. LMC clusters differ from Galactic globulars in another important sense: many have large projected ellipticities. From dynamical studies, one should be able to discern whether this is a result of rotation or mergers by measuring the relative importance of random versus ordered motions.

Several LMC clusters have already been studied dynamically. These include integrated spectra for several old clusters (Elson and Freeman 1985; Dubath, Meylan, Mayor, and Magain 1990; and Mateo, Welch, and Fischer 1991) and individual stellar velocity measurements (Lupton, Fall, Freeman, and Elson 1989 and Mateo, Welch, and Fischer 1991). The work by Lupton *et al.* involved measurements of individual stellar velocities within three young clusters, including NGC 1866. Unfortunately, due to large radial velocity measurement uncertainties (i.e., $v_{err} \approx 3$ km s^{-1}), the authors were only able to place upper limits on the cluster mass. The present work utilizes higher precision radial velocities, and a larger sample of stars, including many stars within the cluster core.

In §II the observations, reductions, and results of the surface photometry will be discussed, followed by a similar treatment for the radial velocity measurements in §III. §IV deals with the 2 different techniques used to estimate the cluster mass and in §V we discuss the slope of the IMF.

2.2   SURFACE PHOTOMETRY

2.2.1   Observations and Reductions

In order to derive a surface brightness profile for NGC 1866, four V-band CCD frames were obtained on the Las Campanas 1.0 m telescope. The TI 800^2 chip was used (readout noise = 11 e$^-$, gain = 2.1 e$^-$/ADU, and angular scale = 0.45"/pix), and the integration times were 300s per image.

Following a background normalization, the four frames were mosaiced together giving coverage out to a projected radius of R $\approx$ 110 pc (for this study, the distance to the cluster is taken to be D = 51 kpc Welch *et al.* 1991). Surface photometry was performed in a manner similar to Djorgovski (1988). The frames were broken up into a series of concentric annuli centered on the cluster. The annuli

were further divided into eight azimuthal sectors. The average pixel brightness was determined for each sector in a given annulus and the *median* of the eight separate measurements was taken as the representative brightness at the area-weighted average radius of the annulus. The standard error of the median of the eight sectors is equal to the standard error of the mean multiplied by $\sqrt{\pi/2}$ and this was adopted as the photometry uncertainty in each annulus (we thank Dr. R. H. Lupton for pointing this out to us). A single background was determined for all four frames using the region $80 \leq R \leq 110$ pc and is comprised of a combination of sky light and Galactic foreground and LMC field stars. The background level was found to be fairly constant for subsections within this region and therefore we are confident that the cluster contribution in these outer areas is negligible. Typically starcounts are used to construct cluster surface density profiles for regions beyond several core radii (Djorgovski 1988). The starcounts are generally considered superior in this region because they are not as strongly affected by noise in the background light. The FIND command in the DAOPHOT (Stetson 1987) photometry package was employed to determine stellar positions, and stellar densities were tabulated in concentric annuli (the background was determined in the same region as above). The starcounts were then scaled to best correspond to the luminosity measurements at intermediate R. The upper panel of Fig. 2.1 has the luminosity profile represented by open squares, and the starcounts by filled squares. The agreement is excellent for $R > 15$ pc, however, the starcounts appear to be deficient for smaller R, ostensibly resulting from incompleteness due to crowding. Because of this agreement, the luminosity measurements were adopted for the entire profile. Photometric standardization was accomplished through the use of several local standards located on the frames (Welch *et al.* 1991) and E(B-V) = 0.06 was adopted (Brocato *et al.* 1989).
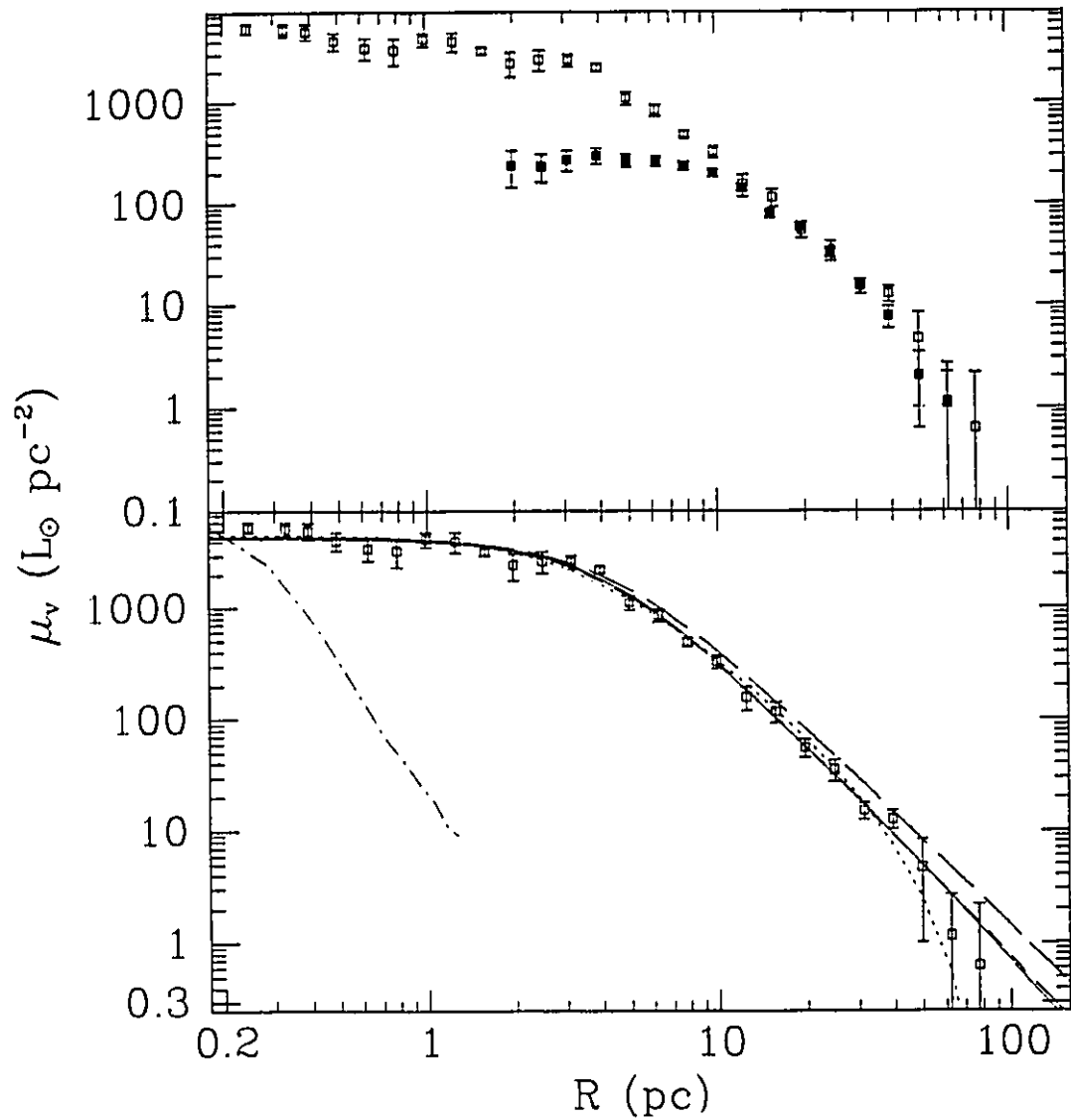
Fig. 2.1 - CCD V band luminosity profile for NGC 1866. The upper panel shows a comparison between brightness measurements (open squares) and starcounts (filled squares). In the lower panel the solid line is the best fit King-Michie model profile ($r_a = 3.0\ r_s$) while the dotted line is the isotropic model. An unbound power-law model is represented by short dashes and the model of Elson, Fall, and Freeman (1987) is shown as long dashes. A typical stellar profile is shown as the dash-dot line.

The background-subtracted surface photometry data for R ≤ 80 pc is presented in Table 2.1. Columns 1 and 3 are the projected radii, while columns 2 and 4 are the luminosity surface densities ($M_{V\odot} = 4.83$ mag, Mihalas and Binney 1981). For R > 40 pc the brightness is within 1.5σ of the background light and therefore highly uncertain.

Table 2.1
Surface Photometry

R (pc)	μ_V ($10^3 L_\odot$ pc^{-2})	R (pc)	μ_V ($10^3 L_\odot$ pc^{-2})	
0.24	5.6 ± 0.6	4.97	1.2	± 0.2
0.33	5.4 ± 0.8	6.25	0.88	± 0.1
0.39	5.2 ± 0.9	7.87	0.50	± 0.04
0.49	4.2 ± 0.8	9.91	0.34	± 0.04
0.63	3.6 ± 0.9	12.48	0.16	± 0.04
0.79	3.4 ± 1.0	15.71	0.12	± 0.02
0.99	4.4 ± 0.7	19.78	0.057	± 0.01
1.25	4.1 ± 0.9	24.90	0 035	± 0.008
1.57	3.4 ± 0.2	31.35	0.015	± 0.002
1.97	2.5 ± 0.7	39.46	0.013	± 0.002
2.49	2.8 ± 0.6	49.68	0.0047	± 0.004
3.13	2.7 ± 0.4	62.54	0.0012	± 0.002
3.94	2.3 ± 0.2	77.56	0.00063	± 0.002

2.2.2   King-Michie Models for the Surface Photometry

Attempts were made to fit projected single-component King-Michie models (King 1966 and Michie 1963) to the photometry data. These models have an energy (E) angular momentum (J) distribution function given by

$$f(E, J) \propto e^{-[J/(2v_s r_a)]^2}\left(e^{-0.5v^2 + W} - 1\right), \tag{2.1}$$

where v_s is the scale velocity, r_a is the anisotropy radius (both described below), and W is a reduced potential. The shape of the density distribution, $\rho_K(r)$, is

determined by solving Poisson's equation and is dependent on two parameters; the central potential W_o, and r_a, beyond which stellar orbits become increasingly radial. Scaling is applied in both the radial (r_s) and luminosity (ρ_{Ko}) dimensions to give the best fit. For a complete description of the models (albeit for the more complex multi-component case) the reader is directed to Gunn and Griffin (1979). Model density profiles with r_a values ranging from 2 r_s to infinity (i.e. an isotropic distribution function) were generated, and projected on to the observational plane. These were binned identically to the observed data and fit using a maximum likelihood technique.

Table 2.2 shows, for each r_a, the best *fitted* King-Michie parameters. Column 1 contains r_a, column 2 is the reduced central potential, column 3 is r_s and column 4 is $c = r_s/r_t$ (r_t is the tidal radius). Column 5 is the reduced chi-square for the fit. Column 6 is the probability that the observed luminosity profile was drawn from the specified King-Michie model. These were derived from 1000 simulations of the surface photometry data per model. Each simulation used a surface profile generated from the best fit model with errors, drawn from the uncertainties shown in Table 2.1. The same fitting procedure originally applied to the real data was utilized and in this way we found the uncertainties in each fitted parameter as well as the distribution of χ^2_ν ($\chi^2_\nu = \chi^2/\nu$, where $\nu = 23$ is the number of degrees of freedom). The remaining columns of Table 2.2 will be discussed in §2.4.1.

Table 2.3 has a summary of the *derived* King-Michie parameters corresponding to the models specified in Table 2.2. Column 1 is the anisotropy radius while column 2 is the central luminosity density, ρ_{Ko}. Column 3 is the dimensionless mass

$$\mu = 4\pi \int \frac{\rho_K}{\rho_{Ko}} r^2 dr \tag{2.2}$$

(King 1966) and column 4 is the cluster luminosity, $L_V = \rho_{Ko} r_s^3 \mu$. Columns 5 and 6 will be discussed in §2.4.1.

Table 2.2
King-Michie - Fitted Parameters

r_a (r_s)	W_o	r_s (pc)	c	χ_ν^2	$P(\chi_\nu^2)$	v_s (km s^{-1})	ζ^2	$P(\zeta^2)$
		Photometry				Velocities		
ISO	6.8 ± 0.15	3.1 ± 0.15	29. ± 3.	1.43	0.06	3.1 ± 0.3	71.16	0.05
50	6.8 ± 0.15	3.1 ± 0.15	29. ± 3.	1.43	0.06	3.1 ± 0.3	71.16	0.05
30	6.8 ± 0.15	3.1 ± 0.15	29. ± 3.	1.41	0.07	3.1 ± 0.3	71.18	0.05
20	6.7 ± 0.15	3.1 ± 0.15	30. ± 3.	1.39	0.08	3.2 ± 0.3	71.19	0.05
10	6.7 ± 0.15	3.2 ± 0.15	33. ± 5.	1.32	0.14	3.2 ± 0.3	71.30	0.04
7	6.6 ± 0.20	3.2 ± 0.15	38. ± 10.	1.24	0.16	3.2 ± 0.3	71.46	0.04
5	6.5 ± 0.20	3.4 ± 0.15	50. ± 30.	1.16	0.22	3.3 ± 0.3	71.72	0.03
4	6.3 ± 0.15	3.5 ± 0.15	70. ± 50.	1.13	0.25	3.4 ± 0.3	71.95	0.02
3	6.0 ± 0.05	3.7 ± 0.40	210. ± 100.	1.08	0.34	3.5 ± 0.4	72.02	0.02
2	5.2 ± 0.05	4.2 ± 0.40	160. ± 70.	1.10	0.29	3.8 ± 0.4	72.57	0.01

Table 2.3
King-Michie - Derived Parameters

r_a (r_s)	ρ_{Ko} (L$_\odot$ pc^{-3})	μ	L_V (10^5L$_\odot$)	Mass (10^5M$_\odot$)	M/L_V (M$_\odot$/L$_\odot$)
ISO	800. ± 70.	22.6 ± 1.5	5.5 ± 0.20	1.20 ±0.25	0.20 ±0.04
50	800. ± 70.	22.6 ± 1.5	5.5 ± 0.20	1.20 ±0.25	0.20 ±0.04
30	800. ± 70.	22.5 ± 1.5	5.5 ± 0.20	1.20 ±0.25	0.20 ±0.04
20	800. ± 70.	22.4 ± 1.5	5.5 ± 0.20	1.20 ±0.25	0.20 ±0.04
10	800. ± 70.	21.8 ± 1.3	5.6 ± 0.20	1.20 ±0.25	0.20 ±0.04
7	780. ± 70.	21.0 ± 1.5	5.7 ± 0.20	1.20 ±0.25	0.21 ±0.04
5	760. ± 60.	19.8 ± 1.5	5.8 ± 0.25	1.20 ±0.25	0.21 ±0.04
4	740. ± 60.	18.5 ± 1.4	5.8 ± 0.30	1.20 ±0.25	0.21 ±0.05
3	640. ± 90.	17.7 ± 0.7	6.0 ± 0.35	1.25 ±0.30	0.22 ±0.05
2	570. ± 90.	13.4 ± 0.7	6.0 ± 0.35	1.40 ±0.30	0.24 ±0.05

The solid line in Fig. 2.1 shows the highest probability model ($r_a = 3r_s$) which, qualitatively, agrees well with the data except at the faint end where the photometry is the most uncertain. It would appear that this model is highly suspect as it predicts a tidal radius of $r_t \approx 800$ pc. However, when r_a becomes sufficiently small, the value of c is *very* poorly constrained as is demonstrated by the large uncertainty terms in Table 2.2. Further, the simulations showed that there is a tendency for r_t to be

overestimated for small r_a. Clearly, if r_t were better determined observationally, we could go a long way towards constraining the distribution function unambiguously. If the orbits really do have this value for r_a then it is relatively small compared to some of the well-studied older clusters (c.f. Gunn and Griffin 1979, Pryor et al 1989, and Dubath et al. 1990). This may not be a surprising result as NGC 1866 is a relatively young cluster and the relaxation timescales (see §2.3.5) support the results of the profile-fitting, indicating that the orbits may not have yet had sufficient time to shed their anisotropy.

The isotropic model, which is the lowest probability model, is shown as the dotted line. In the intermediate regions ($10 \leq R$ (pc) ≤ 30) the model overestimates the luminosity, and in the outermost regions, the model appears to drop off too rapidly. Also shown in Fig. 2.1 as a dash-dot line is a typical stellar profile which is sufficiently narrow such that it will not bias the inferred value of r_a.

Quantitatively, as shown in column 6 of Table 2.2, the worst of the models can be rejected at the 94% confidence level while the best agrees with the model profile at the 34% confidence level. Of course, the probability values are sensitive to the size of the adopted photometry errors and are perhaps best viewed in the relative sense even though these uncertainties are measured directly from the data. Although the best King-Michie models give adequate fits to the surface photometry data, there is some evidence that they may not be an accurate description of the NGC 1866 distribution function. As we will show in §2.3.4, from an analysis of the radial velocities, there is a very high probability that NGC 1866 is rotating, something that was neglected when we constructed the orbital distribution functions. Clearly rotation will have a strong effect upon the density distribution and consequently upon the azimuthally-averaged surface density profile. Hence, application of the King-Michie models is suspect.

While we could add a rotational component to the above models (see Lupton and Gunn 1987 for an example), that would still leave us with a fundamental problem arising from the use of surface photometry to constrain the dynamical nature of the cluster, that of uniqueness. A fairly large range in parameters can give adequate agreement with the data and this is increasingly true when more parameters are added. As mentioned above, the problem could be lessened somewhat if the entire surface density profile (i.e. out to r_t, assuming it exists) could be accurately measured. In the case of NGC 1866 there is an *indication* of a truncation in the surface density profile but this is found at a point where the cluster luminosity density (or equivalently starcounts) is less than a few percent of the background. Previous surface density measurements for this cluster, consisting of a combination of aperture photometry and photographic starcounts out to R $\approx$ 125 pc (Elson, Fall, and Freeman 1987) and CCD photometry out to R $\approx$ 25 pc (Elson 1990) do not feature tidal cut-offs leading those authors to conclude that the cluster is not tidally relaxed (i.e. a tidally imposed radius has not yet been established). The arguments are based on rough theoretical calculations of the expected r_t relying on estimates of the LMC's tidal field and the radius of the cluster's orbit, both of which are highly uncertain. Lupton *et. al.* (1989) present the supposition that NGC 1866 may not have had sufficient time to shed its unbound halo which can result from mass-loss early in the cluster's evolution. If this is in fact the case, then it would be improper to conclude that there is anisotropy present in the stellar orbits from King-Michie models of the surface photometry alone.

2.2.3   *Empirical Model of the Density Distribution*

In light of the possibility that NGC 1866 deviates significantly from the King-Michie models, it is helpful to use a smooth empirical model (i.e. one not based on a

distribution function) in order to approximate the spatial density distribution. This leaves the way clear to create models of the orbits (including anisotropy and rotation if desired) consistent with the density distribution and use the radial velocity data as a constraint. Following the lead of Elson, Fall, and Freeman (1987) an unbound power-law model was applied to the surface photometry data

$$\mu_V(R) = \mu_0[1 + (R/a)^2]^{-\gamma/2} + S, \qquad (2.3)$$

using a weighted least squares fit. S is the background level and the parameter a is related to the scale radius by $r_s = a(2^{2/\gamma} - 1)^{1/2}$. The best-fit model had $\chi^2_\nu = 1.16$ (marginally higher than the best fit King-Michie model) with parameters: $\mu_0 = 4.6 \pm 0.2 \times 10^3$ $L_\odot$ pc^{-2}, a = 4.05 $\pm$0.25 pc and $\gamma = 2.72 \pm 0.1$ (which implies $r_s = 3.3$ pc). The power-law model is plotted as the short dashed line in the lower panel of Fig. 2.1. Elson, Fall, and Freeman's (1987) model is the long dashed line; it appears to overestimate the amount of light at large radii. In order to derive the empirical density function $\rho_E(r)$, μ_V must be deprojected;

$$\rho_E(r) = \rho_{E0}[1 + (r/a)^2]^{-(\gamma+1)/2}, \qquad (2.4)$$

where $\rho_{E0} = 6.8 \pm 0.6 \times 10^2$ $L_\odot$ pc^{-3}. Integrating the density out to infinity yields

$$L_{V\infty} = 2\pi\rho_{E0}a^3\Gamma(\tfrac{3}{2})\Gamma(\tfrac{\gamma-2}{2})/\Gamma(\tfrac{\gamma+1}{2}) = 6.5 \pm 0.3 \times 10^5 L_\odot \qquad (2.5)$$

with approximately 87% of this being contained within r $\leq$100 pc. This value is about 40% smaller than that found by Elson, Fall and Freeman which is consistent with the shallower drop-off exhibited by their model.

2.2.4   Ellipticity

On Dec. 19 1986 a U-band CCD image was obtained of NGC 1866 on the CTIO 0.9m and was used to estimate both the magnitude and position angle (α) of the cluster ellipticity. LMC globular clusters contain many resolved stars and, therefore, do not exhibit a smooth light distribution, greatly complicating attempts to derive ellipticities. The bright giants tend to skew the apparent ellipticities towards high values and one often finds that the ellipticity changes very rapidly as a function of projected radius possibly even rotating by $90°$. After considerable experimentation, the procedure adopted was to first subtract out the resolved stars using DOPHOT (Mateo and Schecter 1989) and then median filter the star-subtracted image (a circular median filter with a $6''$ radius was used). The result was a relatively smooth light distribution with the contribution from the bright giants largely eliminated. It was then possible to use the ELLIPSE task in the IRAF STSDAS package which uses the technique of Jedrzejewski (1987) to fit elliptical contours to a smooth light distribution. Even after removing the bright stars, we were only able to apply the technique in the range $4 \leq R$ (pc) ≤ 16. For $R < 4$ pc the degree of crowding is too large to allow for effective star subtraction while $R > 16$ pc there is insufficient light on the U frame. The upper panel of Fig 2.2 displays ellipticity ($\epsilon = 1 - b/a$) as a function of R and the lower panel shows α. The value for α is very stable for $R \leq 12$ pc at $\alpha = 125° \pm 5°$. Beyond this radius there is an increase in α with a corresponding drop in ϵ. Given the uncertainties the results are consistent with a constant value for α. Previously Frenk and Fall (1982) derived $\alpha = 131° \pm 20°$ and $\epsilon = 0.08 \pm 0.05$ using starcounts in the region $12 \leq R$ (pc) ≤ 50. The two values of α are in excellent agreement and in the region of overlap (i.e. 12 - 16 pc) the values for ϵ are consistent.
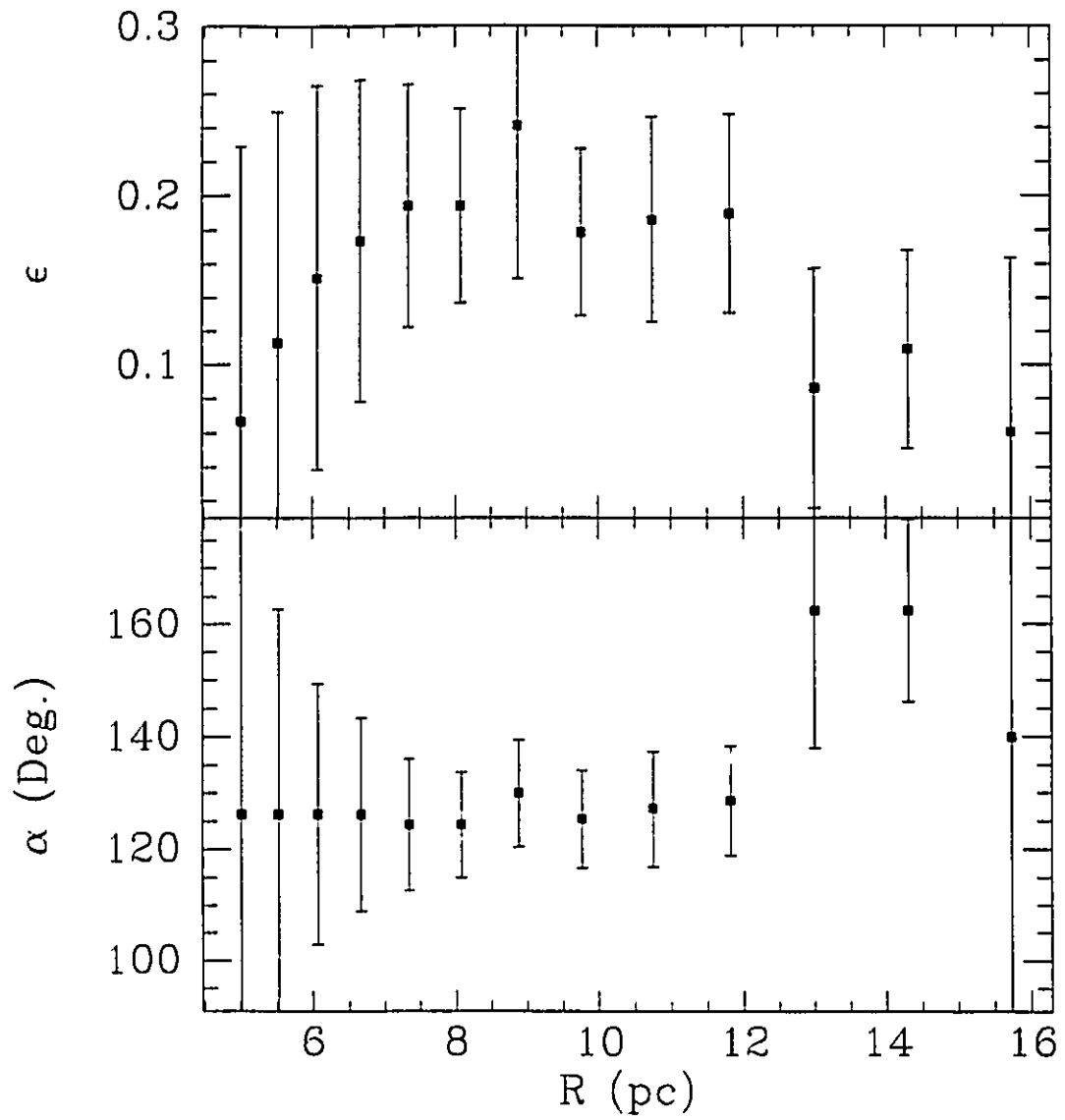
Fig. 2.2 - Plots of ellipticity (upper panel) and position angle of the minor axis (lower panel) vs. projected radius.

2.3   RADIAL VELOCITIES

2.3.1   Observations and Reductions

Spectra of 63 supergiants and 6 Cepheids (Cepheids are from Welch *et al.* 1991) in NGC 1866 were obtained during two runs (1988 December 16-24 and 1989 November 30 - December 17) using the photon-counting echelle spectrograph on the 2.5m Dupont reflector, designed and built by Steve Shectman. A discussion of the observations and reductions can be found in Welch *et al.* but will be repeated here for convenience.

Spectra were reduced to radial velocities entirely within the IRAF [1] environment (see Tody 1986). Orders were identified, traced, and extracted using the APSUM task in the ECHELLE package. The continuum was subtracted from each order using the ONEDSPEC task CONTINUUM and then dead pixels at the end of each order were zeroed using the IMREPLACE task in the PROTO package. The dispersion solution for each object spectrum was obtained by first extracting the apertures determined for the stellar spectrum and then using the ECIDENTIFY or ECREIDENTIFY task in the ECHELLE package. Typically, 320 lines would be reidentified and the rms scatter for a xorder=6, yorder=4 fit would be 0.022-0.035 Å . The spectra were rebinned logarithmically and dispersion-corrected using the task ECDISPCOR which produced one dimensional spectra of length 8192 pixels for use in the cross-correlation routines. Four orders spanning 5120-5460 Å were used because of the large number of strong, sharp absorption lines available. The final step was the cross-correlation using the task RVXCOR in the new RV package (Beta Test Version 2.0). Before cross-correlation, the spectra were filtered with a

---

[1] IRAF is distributed by the National Optical Astronomy Observatories, which is operated by the Association of Universities for Research in Astronomy, Inc., under contract to the National Science Foundation.

ramp filter cutting on 20 wavenumbers, reaching full value at 30, starting to decrease at 1024, and reaching zero at 2048. The position of the cross-correlation peak was fit with a Gaussian and the error in the velocity determined using the method of Tonry and Davis (1979). Fig. 2 of Côté et al. (1991) shows a reduced spectrum for one of the Cepheids (HV 12198) and the corresponding cross-correlation function.

The exposure times ranged from 600 - 800s and frequent Th-Ar lamp spectra were obtained in order to ensure an accurate dispersion correction. In the orders used for cross-correlation, the pixel size is approximately 0.17 Å, which corresponds to about 11 km s^{-1}. The radial velocities obtained in this manner are of high precision; the mean uncertainty for an individual observation is $v_{err} \approx 1.0$ km s^{-1}.

Of concern is the potential for velocity zero-point drifts between observations taken on different nights and particularly between the different observing runs. During the 1988 observing run, higher signal-to-noise (S/N) spectra of a late-type local velocity standard were obtained and used as cross-correlation templates for each of the nights. When the templates were cross-correlated against one another the night-to-night variation was 0.5 km s^{-1}. For the 1989 run the same star was observed each night along with 1 to 5 other local standards corresponding to other program clusters. Unfortunately, these were of insufficient S/N to use as templates so a star from the first run was used instead. The second-run local standards were used to determine a nightly zero-point correction which had a mean magnitude of ≈ 0.5 km s^{-1} over 17 nights. After the correction, the NGC 1866 velocity standards had a night-to-night variation of 0.4 km s^{-1}. The IAU radial velocity standard 33 Sex ($v_r = 42.8$ km s^{-1}) was observed repeatedly during both runs and served to determine the velocity zero-point. After corrections, the difference in mean velocities for the NGC 1866 program stars between the two runs was less than 0.1 km s^{-1}.

The heliocentric radial velocities are biased by two systematic effects: 1) the transverse velocity of NGC 1866 will impose a radial component which varies as a function of position and 2) the rotation velocity of the Galaxy plus the velocity of the local standard of rest with respect to the Galactic rotation will have differing components towards stars with differing positions within the cluster. The velocity corrections due to the first effect never exceed 0.2 km s^{-1} for any star, and only 7 out of 69 program stars have corrections larger than 0.1 km s^{-1}. The second effect resulted in completely negligible velocity corrections. Hence neither were applied.

2.3.2   Positions, Velocities, and Non-Members

Identifications, positions (projected radius (R) in pc and position angle Θ), and velocities are presented in columns 1 through 4, respectively in Table 2.4. Superscripts of c or 2 on the identifications indicate that the star is a Cepheid with multiple observations or that the star has been observed twice, respectively. Repeated measurements of stars indicate that the RVXCOR-generated uncertainty estimates are good to 10-20% (Welch et al. 1991). Column 5 will be discussed in §2.3.4. Based on their radial velocities, some of these stars are clearly foreground Galactic stars and are easily removed. More subtle is the problem of field LMC stars. There are two relatively high residual velocity stars, 2 and 8, but because of their position (R $\leq$ r$_s$ for both), there is a high probability that they are cluster members so they have been kept. It is, however, possible that they are binaries. (As an aside: several other clusters have high residual velocity stars observed near their centers. Gunn and Griffin (1979) found two stars in M3 with residual velocities of 3.5σ and 4.5σ which they rejected. Lupton et al. (1987) see an increase in M13's velocity dispersion for R < 10 r$_s$ and Meylan and Mayor (1986) see central velocity cusps in both 47 Tuc and Omega Centaurus.) Star 27 has an anomalously low

velocity. This star has R ≈ 2.3r, and is therefore quite likely an LMC field star so it has been rejected.

2.3.3   Velocity Dispersion

Finder charts for all stars with names beginning with B or C can be found in Robertson (1974), and Fischer *et al.* 1992a. Welch *et al.* (1991) has positions for all the Cepheids. Fig. 2.3 shows the positions, relative to the cluster center (0,0), of the NGC 1866 member stars with measured velocities. Fig. 2.4 shows a velocity histogram (bin width = 1 km s^{-1}) of the stars and a Gaussian which has been fit to the data by weighted non-linear least squares. It has $\sigma = 2.3$ km s^{-1} and $v_{ave} = 301.2 \pm 1.0$ km s^{-1}. Fig. 2.5 displays a plot of individual velocities versus position angle (lower panel) and versus projected radii (upper panel). The mean velocity derived here is significantly higher than the values derived in previous studies which yield an average of 281 ±6 km s^{-1} (see Baird and Flower 1987 for a summary). All previous radial velocity work has utilized lower reciprocal dispersion spectra and we suspect that systematic errors in calibration and/or reduction account for the difference.

2.3.4   Rotation and Ellipticity

If we can get an estimate of the relative importance of systematic versus random motions within the cluster then we can explore the consequence for the mass estimate and test the relationship to the cluster ellipticity. The advantage of studying a young cluster such as NGC 1866 is that evolutionary processes would have had less opportunity to affect the original cluster rotation. Unfortunately, it is not a trivial matter to detect and especially to quantify the cluster rotation with such a small sample of stellar radial velocities and this is worth keeping in mind throughout the following discussion.

Table 2.4
Positions and Radial Velocities

Star	R (pc)	Θ (Deg.)	v_x (km s^{-1})	$v_x - v_{rot\ x}$ (km s^{-1})
1	0.1	291.0	302.9 ± 1.9	302.9
2	1.2	50.2	309.9 ± 0.9	309.6
3	1.5	21.0	301.6 ± 0.7	301.1
4	1.9	174.8	303.0 ± 0.7	303.5
5	2.5	323.0	301.7 ± 0.7	301.2
6[2]	2.5	93.8	301.4 ± 0.9	301.3
7	2.6	339.1	302.4 ± 0.7	301.8
8	3.4	17.8	308.1 ± 1.5	307.3
9	3.8	137.6	300.2 ± 1.1	300.8
10	4.1	215.6	295.5 ± 0.7	296.4
11	4.3	310.8	302.4 ± 0.9	301.8
12	4.4	251.9	303.1 ± 0.8	303.7
13	4.5	293.4	298.9 ± 0.2	298.5
14	5.3	347.6	298.2 ± 0.7	297.2
15	5.4	36.3	302.1 ± 1.5	301.1
16	5.5	72.4	300.1 ± 1.1	299.4
17	5.6	138.7	304.1 ± 1.0	304.9
18	5.8	221.3	298.9 ± 0.6	299.8
19	5.9	97.6	302.6 ± 0.6	302.5
20	6.2	358.6	306.8 ± 1.1	305.7
21	6.3	173.2	304.4 ± 1.3	305.4
22	6.4	253.0	299.7 ± 0.9	300.3
23	6.7	85.1	303.2 ± 1.2	302.8
V7[c]	7.7	44.4	300.2 ± 0.5	299.2
24	7.8	202.1	300.0 ± 1.2	301.0
25	7.8	290.7	301.5 ± 0.8	301.1
26	7.9	117.4	302.0 ± 1.6	302.6
27	8.0	286.3	285.6 ± 1.6	
28	8.3	63.3	304.1 ± 0.6	303.2
BIV-25	8.3	15.0	300.0 ± 0.6	298.9
29	8.8	339.1	302.1 ± 1.4	301.1
BIV-27	9.1	28.8	303.1 ± 1.3	302.1
BI-23	9.1	93.4	299.3 ± 1.2	299.0
V4[c]	9.3	354.1	303.0 ± 0.6	301.9
30	10.0	154.3	296.0 ± 1.6	297.0
BIV-61	10.1	69.1	300.7 ± 1.1	299.8
BIV-70	10.3	51.0	303.8 ± 1.6	302.8
31	10.6	290.6	304.6 ± 0.6	304.2

Table 2.4 (cont.)
Positions and Radial Velocities

Star	R (pc)	Θ (Deg.)	v_r (km s^{-1})	$v_r-v_{rot\ x}$ (km s^{-1})
BII-64	10.7	221.7	301.4 $\pm$ 1.1	302.4
BIII-4	11.4	283.9	301.8 $\pm$ 0.7	301.6
BII-16	11.6	198.1	295.9 $\pm$ 1.3	297.0
BIII-1	12.0	352.9	299.1 $\pm$ 1.4	298.0
BIV-55[2]	12.1	78.8	302.1 $\pm$ 0.4	301.3
BI-49	12.2	162.2	297.3 $\pm$ 1.0	298.3
BII-39	12.5	255.0	303.6 $\pm$ 0.9	304.5
BIII-2	12.8	334.5	301.8 $\pm$ 1.0	300.7
BIV-50	13.2	66.9	298.7 $\pm$ 1.1	297.7
BIV-36	13.7	45.1	302.5 $\pm$ 1.3	301.4
BIV-8	14.1	15.8	304.8 $\pm$ 1.4	303.7
BIV-38	14.1	49.0	300.8 $\pm$ 1.1	299.8
BIV-9	14.3	1.9	299.0 $\pm$ 1.5	297.9
BI-16	14.9	105.2	299.6 $\pm$ 0.8	299.9
BI-15	15.5	113.5	297.6 $\pm$ 0.9	298.2
BIV-39[2]	15.6	47.5	299.4 $\pm$ 0.3	298.3
BII-41	15.6	242.8	299.6 $\pm$ 0.7	300.5
BII-5	15.8	189.4	299.1 $\pm$ 0.5	300.2
BIV-7	15.9	16.1	301.2 $\pm$ 0.9	300.2
BIV-45	16.0	69.7	302.9 $\pm$ 0.8	302.0
BI-17	16.7	104.7	63.2 $\pm$ 0.9	
BIV-6	17.8	19.2	303.2 $\pm$ 1.2	302.1
BIII-35	19.2	290.3	303.0 $\pm$ 0.9	302.4
BII-23	19.9	226.0	300.4 $\pm$ 1.1	301.4
BIII-3	21.4	308.0	305.9 $\pm$ 1.3	305.0
BIII-5	21.5	315.3	305.0 $\pm$ 1.3	304.0
HV12198[c]	22.1	300.5	299.8 $\pm$ 0.2	299.0
HV12203[c]	26.3	136.2	302.9 $\pm$ 0.7	303.8
CI-21	26.9	146.5	301.2 $\pm$ 0.6	302.1
HV12199[c]	32.2	219.8	300.8 $\pm$ 0.4	301.7
CI-3	32.9	100.8	302.0 $\pm$ 1.1	302.2
CII-12	36.8	206.1	298.4 $\pm$ 0.8	299.3
HV12197[c]	43.6	115.0	299.0 $\pm$ 0.6	299.8

The first step was to derive a reliable means of determining the probability that rotation exists, and the position angle of the rotation axis. This was accomplished
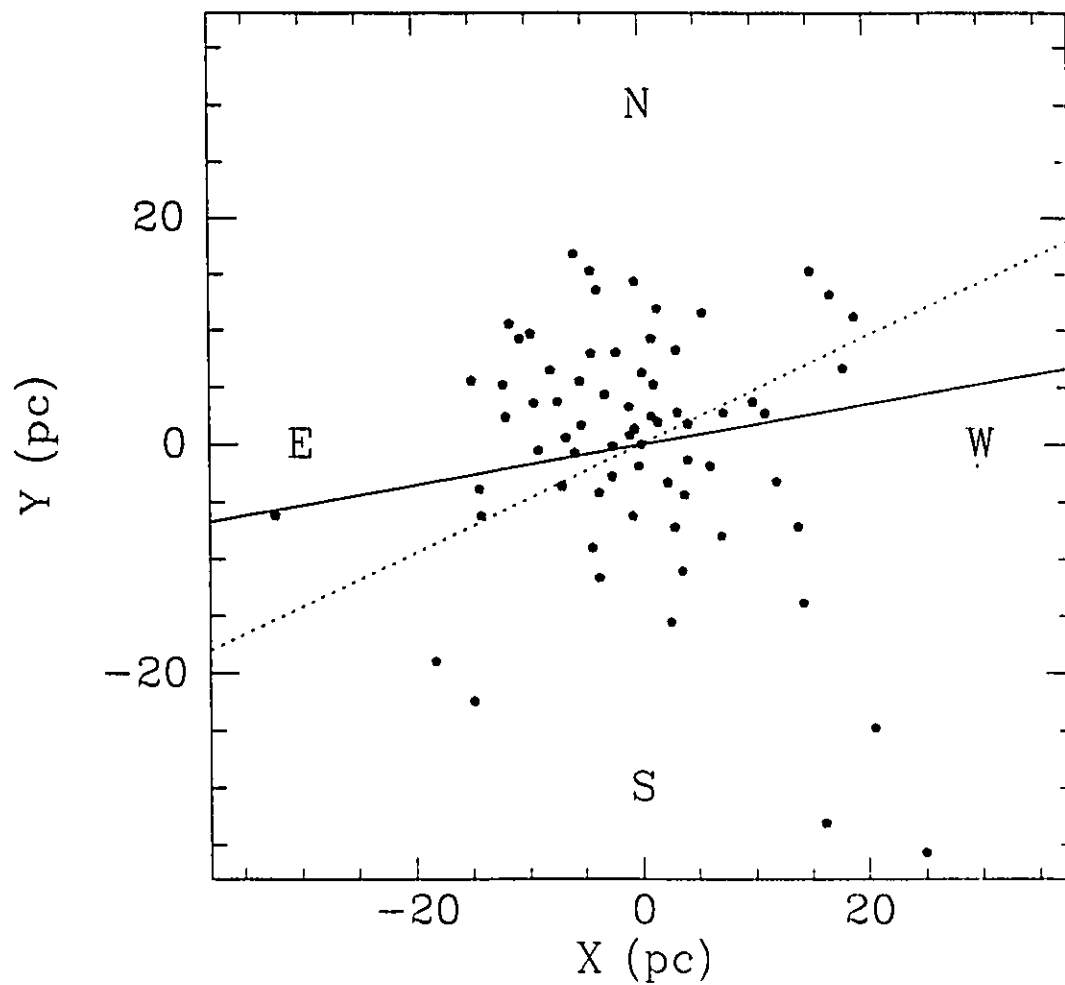
Fig. 2.3 - Positions with respect to the cluster center for stars with measured radial velocities. The straight line indicates the rotation axis while the dotted line is the photometric minor axis.
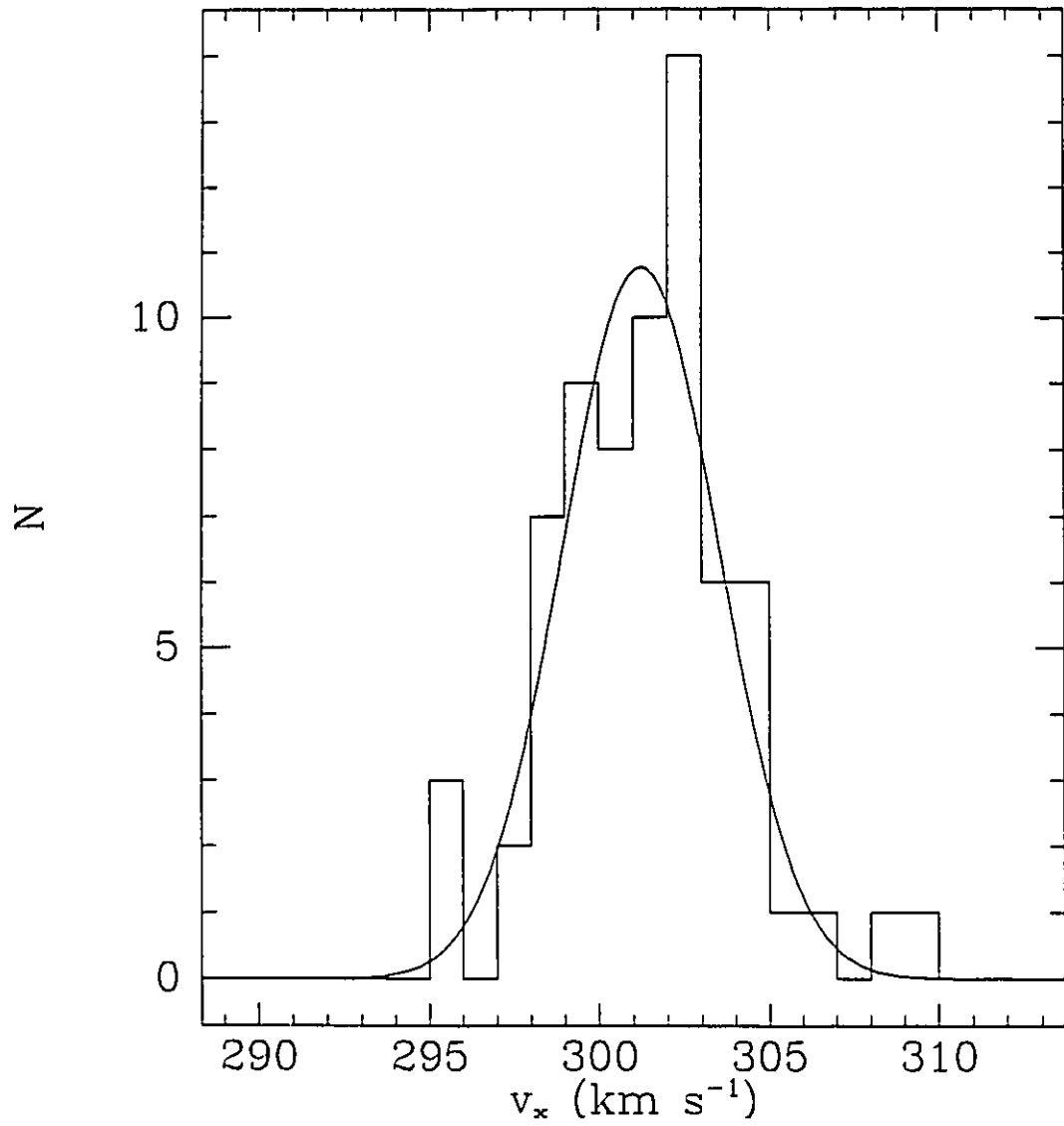
Fig. 2.4 - A histogram of the radial velocities with 1 km s^{-1} bin widths. Shown as a solid line is the best-fit Gaussian with mean velocity 301.2 km s^{-1} and $\sigma = 2.3$ km s^{-1}. The velocities are consistent with this distribution at the 90% confidence level.
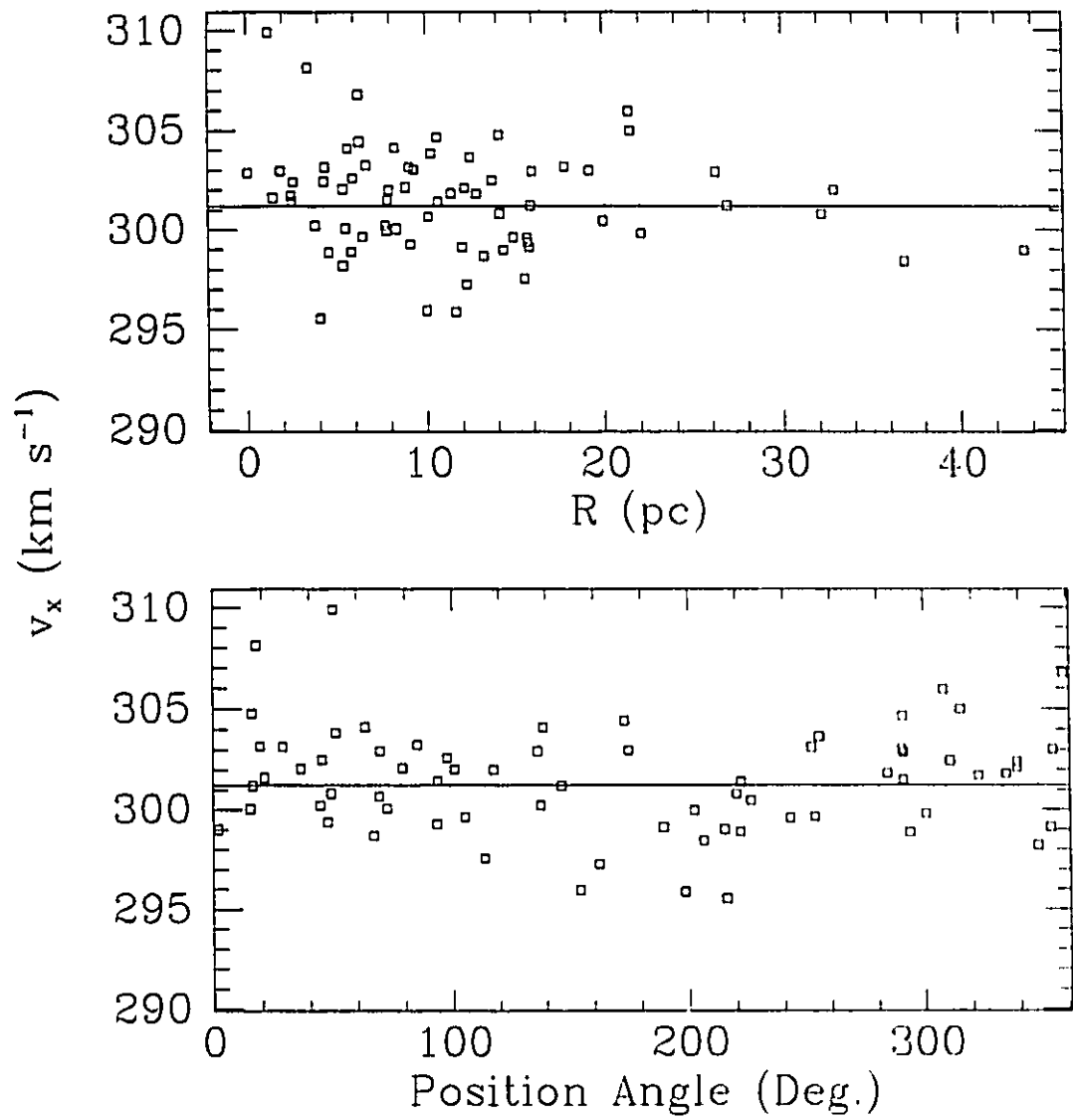
Fig. 2.5 - Plot of observed radial velocity versus position angle (lower panel) and projected radius (upper panel). The solid lines indicate the cluster mean.

by measuring the difference in median velocities on either side of an imaginary axis which is stepped around the cluster center at 1° intervals. The velocity difference is maximized when the axis corresponds to the projected rotation axis. The top panel of Fig 2.6 shows a plot of the velocity differences versus the position angle of the axis. The best-fit sine curve has an amplitude of $A = 1.8$ km s^{-1} and the implied rotation axis is $100° \pm 25°$ which is in fairly good agreement with the value of α derived in §2.2.4 and is almost exactly perpendicular to the *apparent* rotation axis which would arise solely as a result of the transverse motion of the LMC.

In order to check the significance of this rotation detection, 10000 sets of artificial data were constructed. Each set had the same projected stellar positions as the real data, and the velocities were drawn at random from a distribution defined by Jeans' equation with the rotational term set to zero (see §2.4.1 for a lengthier discussion). The artificial data were tested for rotation in the same manner as the observed data. The upper panel of Fig. 2.7 displays histograms of the amplitudes of the best-fit sine functions for the artificial data sets with the arrow indicating the value from the observed data. Fewer than 300 out of 10000 had an amplitude higher than the original data set implying that rotation has been detected at better than the 97% confidence level.

Considering the sparsity of the radial velocity data, quantifying the rotation at all positions within the cluster is a difficult task which is necessarily complicated by ignorance of the cluster inclination. In order to fit a rotation law to the velocity data we assumed a cluster inclination of i = 90°. For the rotation law $v_{rot}(\vec{r})$, $v_x(\vec{r})$ = $v_{rot}(\vec{r})\sin\theta\sin i$ (i=90°) is the velocity component along the line of sight ($\theta = 0.$ is the rotation axis and x points along the line of sight). For a star at a projected radius R, one can use the known luminosity distribution, to derive an average value
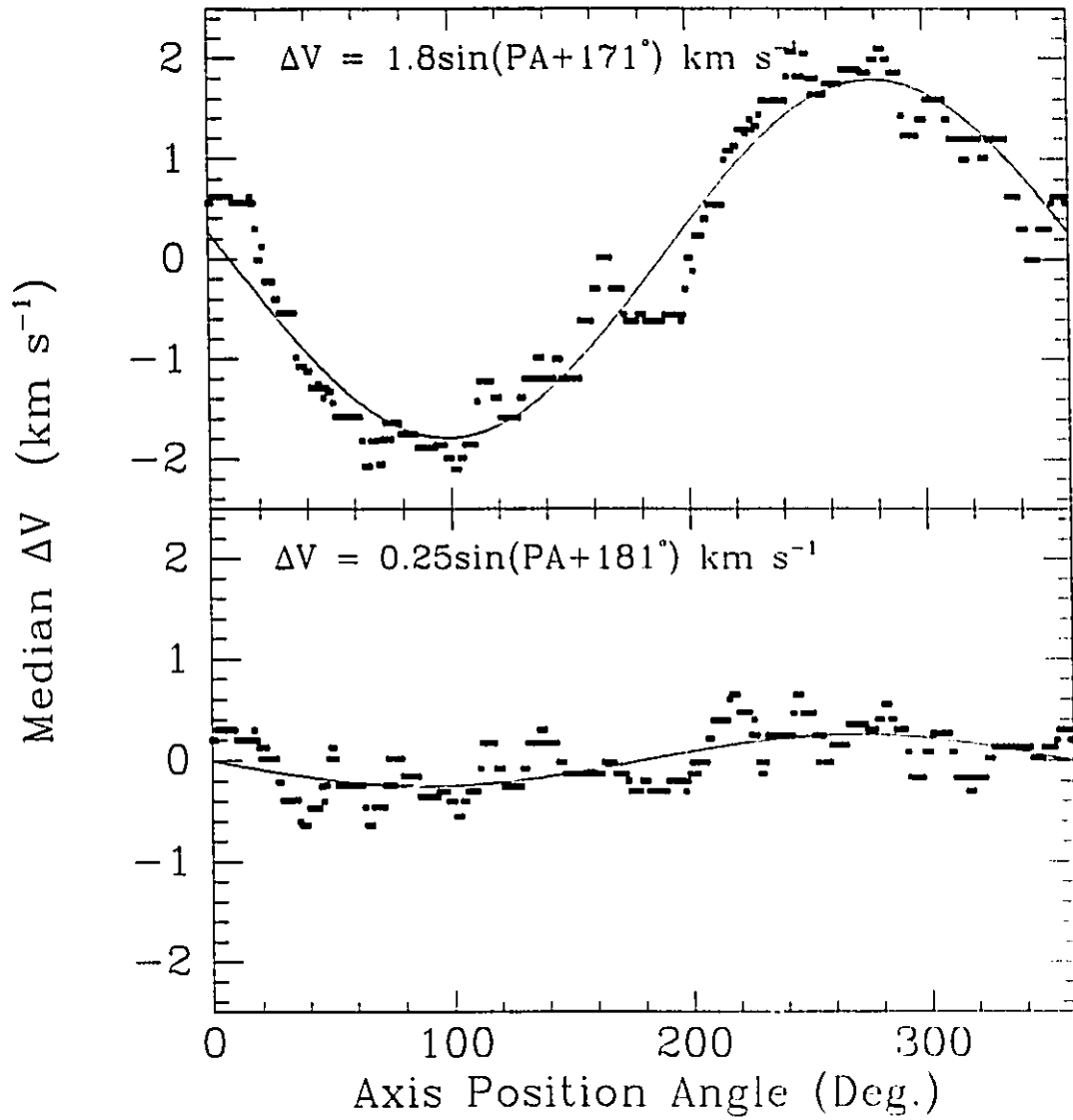
Fig. 2.6 - The upper panel displays the difference in median velocity for stars on either side of an axis at the specified position angle. Also shown is the best fit sine function corresponding to a rotation axis with position angle 100°. The lower panel is the same but for rotation-subtracted data.
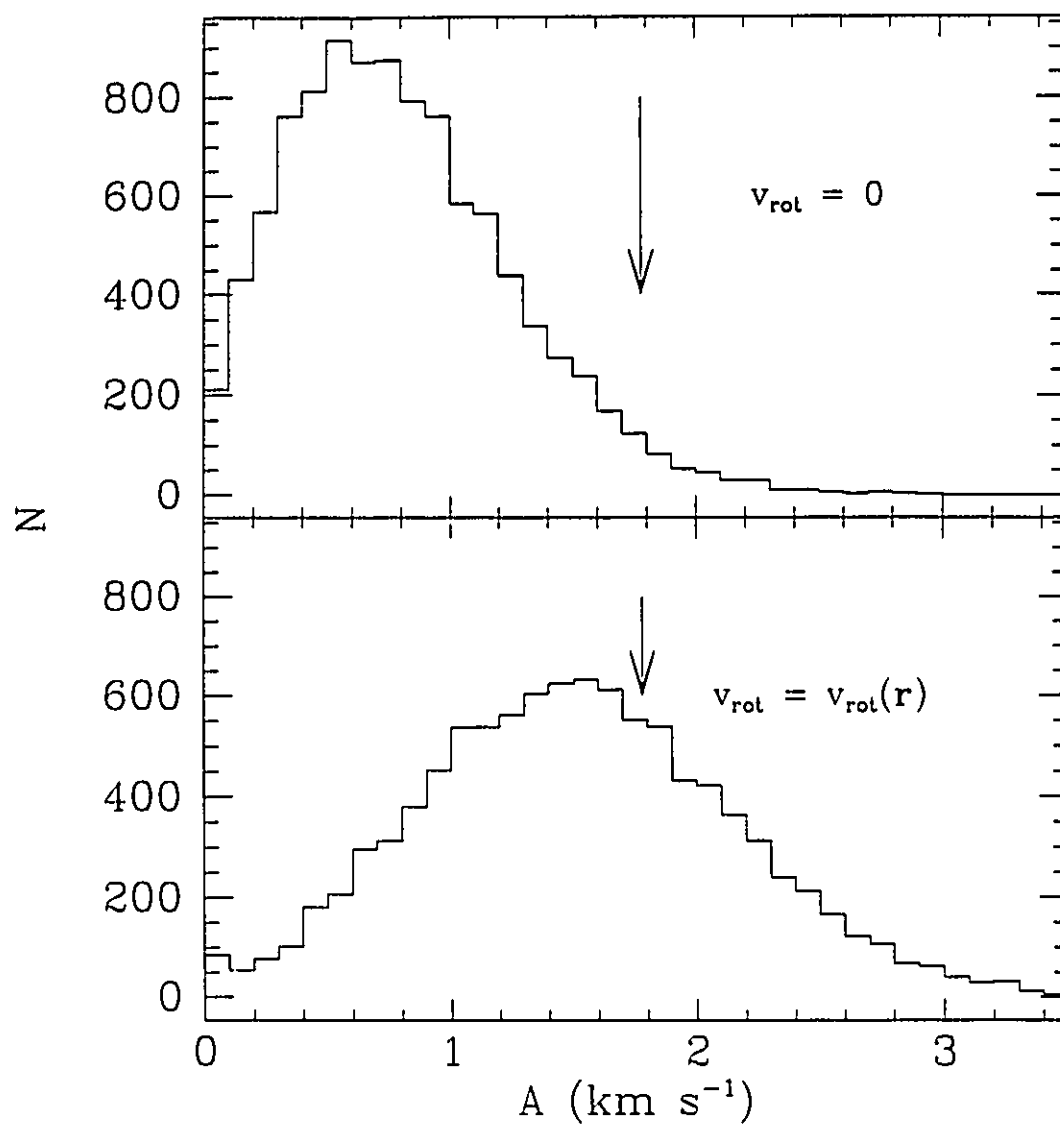
Fig. 2.7 - The upper panel is a histogram of the amplitudes of the best fit sine curves for 10000 Monte Carlo simulations of the data with no rotation. The observed amplitude is above the 97th percentile (marked by arrow). The lower panel is the same but for models with rotation added.

for the projected rotation velocity

$$V_{rot}(R, \Theta) = \frac{\int_0^\infty \rho_E(\sqrt{R^2 + x^2})v_x dx}{\int_0^\infty \rho_E(\sqrt{R^2 + x^2})dx}.$$ (2.6)

The last step is to minimize χ^2 by adjusting the parameters of $v_{rot}(\vec{r})$.

The rotation law used had the form

$$v_{rot} = a_1 \sqrt{\frac{M(a_2 r_{xy})}{a_2 r_{xy}}} e^{-z^2/a_3^2},$$ (2.7)

where r_{xy} is the distance from the rotation axis, $M(r)$ is the mass contained within r, and z is the height above the equatorial plane. This law has solid body rotation at small r_{xy} which peaks at some r_{xy} determined by a_2, at a maximum value determined by a_1 beyond which it declines. The parameters a_1, a_2 and a_3 are varied in order to minimize χ^2. This model does not have any physical significance but does produce a *reasonable* family of rotation curves with a minimum of free parameters. The model was applied to the data from Table 2.4 with three stars removed; the two stars with the highest residual velocities and the star with the smallest projected radius. Unfortunately, due to the small number of stars with measured radial velocities, it is difficult to constrain the parameters using only χ^2. A fairly large range in the parameters can yield *equally* good *overall* fits but may in fact fit subsets of the data somewhat differently and result in considerably different models in the regions beyond the measured range. Therefore, once the optimal range in the parameters had been determined through a χ^2 minimization, another criterion was invoked. The different best-fit rotation curves were subtracted from the radial velocities and a rotation check was performed on the residuals using the velocity difference technique explained above. The set of parameters resulting in the smallest amplitude sine curve was then chosen as the "best" model. This model had a peak rotation velocity of 1.3 ± 0.5 km s^{-1} at a radius between $10.0 - 15.0$

pc, $\chi^2/\chi^2_{v_{rot}=0} = 0.87$, where the errors are derived from Monte-Carlo simulations (see below). The position of the rotation peak is rather uncertain due to the lack of data at large R and we cannot rule out the possibility that the peak is actually further out. As a check on the fitting procedure, the rotation laws were applied to the same data but with the rotation axis rotated by 90°. No significant rotation was seen for this case.

For the rotation-subtracted velocities (see Column 5 of Table 2.4) the amplitude of the sine curve was reduced to $A = 0.25$ km s^{-1}, less than 15% of the amplitude for the original data (shown in the bottom panel of Fig. 8). A second look at the upper panel of Fig. 2.7 shows that when models of the velocity measurements for a cluster with *no* rotation were simulated over 90% had amplitudes exceeding $A = 0.25$ km s^{-1}. Further, when we generate models with no rotation and then attempt to subtract rotation as described above we find that about 75% of the models had residual amplitudes exceeding $A = 0.25$ km s^{-1}. Therefore we conclude that there is no significant residual rotational component left in the rotation-subtracted velocities.

Finally, knowing the rotation law and the distribution of velocity dispersions it is possible to construct Monte-Carlo simulations of the radial velocity measurements, this time containing a rotational component, and apply identical reduction techniques to the artificial data. In this manner the accuracy of the techniques used to constrain the rotation can be quantified. The results are: 1) the derived position angle of the rotation axis does not suffer from systematic errors but it has an uncertainty of ±25°. 2) The value of A is a bit less than $\frac{1}{2}\sigma$ above the mean value for the simulations implying that perhaps the magnitude of the rotation curve has been underestimated. However, 3) the mean value of the magnitude of the rotation curve for the models is within 6% of the input value and the standard deviations is

about 40%. The simulations, however, do not take into account possible mismatches between the model and the true cluster rotation law.

The derived rotation parameters all have substantial uncertainties which are compounded by the lack of information regarding the inclination. Therefore, in the subsequent analyses both the cases with and without rotation were considered.

2.3.5   Evolutionary Timescales

The stars with measured velocities are all supergiants, with masses very close to the current turn-off mass ($m_{to} = 4.9$ M$_\odot$ Brocato *et al.* 1989, or $m_{to} = 4.2$ M$_\odot$ Chiosi *et al.* 1990). If equipartition of energy has occurred these stars, being the most massive, would have a velocity dispersion below the mean value for all mass classes. This is true even in the case where post main-sequence evolution results in significant mass loss as the stellar evolutionary timescales are insufficiently long to result in large stellar velocity changes for the evolved stars. Therefore, it is necessary to determine the timescales for equipartition of energy (and mass segregation). Two important timescales are the central relaxation time

$$t_{ro} = (1.55 \times 10^7 \text{yr}) \left(\frac{r_s}{\text{pc}}\right)^2 \left(\frac{v_s}{\text{km s}^{-1}}\right) \left(\frac{M_\odot}{\langle m \rangle}\right) [\log(0.5M/\langle m \rangle)]^{-1} \qquad (2.8)$$

$$= 1.3 - 6.9 \times 10^8 \text{yr}$$

(Lightman and Shapiro 1978) and the half mass relaxation time

$$t_{rh} = (8.92 \times 10^8 \text{yr}) \left(\frac{M}{10^6 M_\odot}\right)^{1/2} \left(\frac{r_h}{\text{pc}}\right)^{3/2} \left(\frac{M_\odot}{\langle m \rangle}\right) [\log(0.4M/\langle m \rangle)]^{-1} \qquad (2.9)$$

$$= 3.3 - 17.0 \times 10^9 \text{yr}$$

(Spitzer and Hart 1971). In the above two equations $\langle m \rangle = 0.12 - 0.74M_\odot$ is the mean stellar mass (see §2.5) , $M = 1.25 \times 10^5$M$_\odot$ is the total cluster mass (see §2.4), and $r_h = 11$ pc is the radius containing half the cluster mass. The best

current age estimates for NGC 1866 vary from $\tau \approx 0.5 - 2.0 \times 10^8$ years depending on which stellar models are employed. Clearly, there has not been enough time (except perhaps in the very center) for significant mass segregation or equipartition to occur. We can, therefore, conclude that no large systematic errors are being introduced into the velocity dispersions.

Another possible problem is primordial mass segregation. This would occur if star formation in the dense core region favored a different ratio of high-to-low mass stars than at larger radii. While this should not effect the velocity dispersion greatly, it would mean that the assumption of a uniform M/L is incorrect. Consequently the derived luminosity density profile would not be an adequate representation of the mass density profile. There is marginally significant evidence for mass segregation based on an examination of photographic star counts with different cut-off luminosities (Elson, Fall and Freeman 1987). The effect, if real, is not large and therefore for the rest of this study we assume no mass segregation.

2.4   MASS DETERMINATIONS

2.4.1   King-Michie Models

The mass of a King-Michie model is given by

$$M = 167 r_s \mu v_s^2 \qquad (2.10)$$

Illingworth (1976), where r_s and μ are given in Tables 2.2 and 2.3, respectively, and v_s is the scale velocity. The run of $\sigma_r^2(r)$ and $\sigma_t^2(r)$ are determined from

$$\sigma_{r,t}^2(r) = \frac{\int_{|\sigma| \leq W(r)} f(\sigma, W) \sigma_k^2 d^3\vec{\sigma}}{\int_{|\sigma| \leq W(r)} f(\sigma, W) d^3\vec{\sigma}}, \qquad (2.11)$$

where W is the potential (W = 0 at the tidal radius) and $\sigma_k = \sigma\cos\theta$ or $\sigma\sin\theta$ for σ_r or σ_t, respectively. Comparisons were made between the observed velocities and

the model velocity dispersion projected along the line of sight,

$$\sigma_p^2(R) = \frac{2}{\mu(R)} \int_R^\infty \frac{\rho_K(r)[(r^2 - R^2)\sigma_r^2(r) + R^2\sigma_t^2(r)]dr}{r(r^2 - R^2)^{1/2}}, \qquad (2.12)$$

(Binney and Tremaine 1987, p. 208), yielding the optimal value for v_s. The comparison was accomplished using the maximum likelihood technique outlined in Gunn and Griffin (1979). Simply put, the probability density function for v_{xi}, an observed stellar velocity, is a Gaussian with standard deviation equal to the model dispersion plus the velocity uncertainty added in quadrature:

$$P_i \sim \frac{1}{\sqrt{v_{err\ i}^2 + v_s^2 v_{p\ i}^2}} e^{-(v_{x\ i} - v_{ave})^2/2(v_s^2 v_{p\ i}^2 + v_{err\ i}^2)}. \qquad (2.13)$$

One minimizes this function with respect to v_s and v_{ave} resulting in two equations which can be solved simultaneously for the most probable values of the two parameters.

The values of v_s thus obtained are displayed in column 7 of Table 2.2. The corresponding masses and M/L_V ratios are in columns 5 and 6 of Table 2.3. The model which was shown to be in best agreement with the surface photometry ($r_a = 3r_s$, see §2.2.2) has $M = 1.25 \pm 0.25 \times 10^5$ $M_\odot$ and $M/L_V = 0.23 \pm 0.05$ $M_\odot/L_\odot$. From Table 2.3, one can see that the total cluster mass and M/L_V are fairly insensitive to assumptions about r_a.

Monte-Carlo orbit simulations were used to determine the uncertainties implicit in the maximum likelihood technique and to search for any possible systematic effects. We started with the known projected radii (R) of the program stars. The true radius is in the range $R \leq r \leq r_{max}$, where r_{max} can extend to infinity for an unbound distribution. If x is the displacement from the mean cluster position along the line-of-sight such that $r = \sqrt{R^2 + x^2}$ then the probability that the star is at x is

$$p(x) \sim \rho_K(\sqrt{R^2 + x^2}). \qquad (2.14)$$

A three-dimensional position along with corresponding model-dependent radial and tangential velocities were drawn at random from their respective probability distributions. The velocity component along the line-of-sight was then determined, and an error term, drawn from a Gaussian distribution with standard deviation equal to the velocity error, as tabulated in Table 2.4, was added. This process was repeated, producing 10000 sets of data each with a given mass and r_a and the same projected positions and velocity measurement errors as the original data set. Finally the maximum likelihood technique was applied to each of the artificial data sets and the results compared to the input values for the models. Systematic biases for the mass determinations were all less than 5%, testifying to the soundness of the technique. The scatter in v_s for a particular model was at the 10% level resulting in a 20% uncertainty in cluster mass as this is the dominant contribution to the mass uncertainty.

A goodness-of-fit statistic

$$\zeta^2 = \sum \frac{(v_{x\ i} - v_{ave})^2}{(v_s^2 v_{p\ i}^2 + v_{err\ i}^2)} \tag{2.15}$$

was generated for each value of r_a and is shown in column 8 of Table 2.2 (67 degrees of freedom). While this is not a true χ^2 in the conventional sense, the distribution of this statistic can be extracted from the Monte Carlo simulations. Column 9 shows the probability of exceeding the observed ζ^2 assuming that the cluster velocities are specified by the model parameters indicated and have the uncertainties tabulated in Table 2.4. In other words, *if the velocity errors are well estimated*, it is the probability that the cluster velocities are drawn from the specified distribution. As with the surface photometry, these probabilities are sensitive to the assumed uncertainties, and since no attempt was made to model in non-members or binaries they are potentially underestimated. Therefore, the probabilities are perhaps best

regarded in the relative sense. Models with $r_a \geq 20r_s$ provide the best agreement with the velocity data in contradiction to the surface photometry results which prefer a greater degree of anisotropy.

As an alternative to the King-Michie models, which may not adequately describe NGC 1866 and do not incorporate cluster rotation, we turn to a more general model for the distribution function.

2.4.2 Empirical Density Models

Initially, the empirical model yields only the relative density distribution for the cluster (assuming a constant M/L). It is necessary to assume a mass for the cluster and generate a velocity dispersion distribution consistent with the density profile. For a rotating spherical system, Jeans' equation (the velocity moment of the collisionless Boltzmann equation) has the form

$$\frac{1}{\rho_E}\frac{\partial}{\partial r}[\rho_E(r)\sigma_r^2(\vec{r})] + \frac{2}{r}[\sigma_r^2(\vec{r}) - \sigma_t^2(\vec{r})] + \frac{\rho_E v_{rot}^2(\vec{r})}{r} = -\frac{GM(r)}{r^2} \qquad (2.16)$$

where σ_r and σ_t are the radial and tangential velocity dispersions, respectively, and v_{rot} is the rotation velocity. A rotating model implies a non-spherical mass distribution in general, however, because of the fairly small values measured for the ellipticity, we make the simplifying assumption of spherical symmetry. Due to the large uncertainty in the rotation parameters, models were constructed both with and without the rotation term.

2.4.3 Non-Rotating Models

Merritt (1985) has shown that for *spheroidal* systems, that is, systems that have surfaces of constant f (the distribution function) defined by

$$\text{constant} = E + \frac{J^2}{2r_a'^2}, \qquad (2.17)$$

the relationship between the two components of the velocity dispersion is

$$\sigma_t^2(r) = \frac{\sigma_r^2(r)}{1 + (r/r_a')^2},$$
(2.18)

where r_a' is the anisotropy radius. Qualitatively, this is similar to r_a for the King-Michie models in the sense that the orbits are fairly isotropic for $r < r_a'$ and become increasingly radial at large r. This enables us to rewrite the Jeans' equation as an integral,

$$\sigma_r^2(r) = \frac{G}{\rho_E(r)(r^2 + r_a'^2)} \int_r^\infty [1 + (\frac{r_a'}{r'})^2]\rho_E(r')M(r')dr',$$
(2.19)

(Binney 1980). As in the case with the King-Michie models the projected velocity dispersion is proportional to the square root of the mass. Thus, it is possible to use maximum likelihood and Monte Carlo techniques similar to those used above to determine the cluster masses and the uncertainties. The results for a range of r_a' are shown in Table 2.5. Column 1 has r_a', and column 2 is the corresponding mass. Column 3 is ζ^2 while column 4 shows the probability (subject to the previously mentioned constraints) that the NGC 1866 velocities are drawn from the specified model velocity distribution. Column 5 is the mass-to-light ratio.

Table 2.5
Empirical Density Models

r_a' (pc)	M_∞ ($10^5 M_\odot$)	ζ^2	$P(\zeta^2)$	M/L_V ($M_\odot/L_\odot$)	M_∞ ($10^5 M_\odot$)	ζ^2	$P(\zeta^2)$	M/L_V ($M_\odot/L_\odot$)
	$v_{rot} = 0$				$v_{rot} = v_{rot}(\bar{r})$			
ISO	1.35 ± 0.3	70.91	0.07	0.21 ± 0.04	1.25 ± 0.3	69.76	0.26	0.19 ± 0.04
100	1.35 ± 0.3	70.95	0.07	0.21 ± 0.04	1.25 ± 0.3	69.77	0.26	0.19 ± 0.04
35	1.35 ± 0.3	71.?8	0.04	0.21 ± 0.04	1.25 ± 0.3	69.95	0.22	0.19 ± 0.04
18	1.40 ± 0.3	72.56	0.01	0.22 ± 0.05	1.30 ± 0.3	70.64	0.12	0.20 ± 0.04
10	1.55 ± 0.3	74.05	0.01	0.24 ± 0.05	1.40 ± 0.3	71.68	0.06	0.22 ± 0.05
5	1.80 ± 0.4	75.09	0.01	0.27 ± 0.06	1.60 ± 0.3	72.93	0.04	0.25 ± 0.05

The results are similar to the King-Michie models in terms of the derived mass and the best values of the anisotropy radii: once again the more isotropic models

are favored yielding $M_\infty = 1.35 \pm 0.25 M_\odot$ and $M/L_V = 0.21 \pm 0.04 \ M_\odot/L_\odot$. They
are also similar in terms of quality of the fits.

2.4.4   Rotating Models

For the rotational case, Jeans' equation cannot be reduced to a simple integral
and must instead be solved as a differential equation. Further, σ_p is no longer
exclusively a function of r, nor does it scale directly with the square root of the mass.
It is now dependent on the height above the rotation axis, z, and the magnitude
of the rotation curve. Consequently, it is not sufficient to generate a single set of
dispersion curves for each r'_a and scale them until the probability density function
(modified such that $v_{ave} = v_{ave} + v_{rot}$) is minimized. Instead, curves must be
generated for a set of masses and each checked to see which produces the most
likely fit.

As has been mentioned in §2.3.4 the rotation law is not well determined with
our limited sample of stars but it is still interesting to see the effect of the assumed
rotation on the cluster mass estimate. The results are shown in Table 2.5; Column
6 is the most probable mass, column 7 is ζ^2 and Column 8 once again shows the
probability that the observed velocities were drawn from the specified distribution.
Column 9 is the mass-to-light ratio.

Qualitatively, the results for the rotating models are similar to the non-rotating
models; the best agreement is seen for the large r'_a models and there is a general
trend towards increasing mass with decreasing r'_a. Quantitatively, however, there
are two major differences. The quality of the fits are considerably higher for all r'_a,
especially for the three largest values. Secondly, the derived masses, are all smaller
than the zero-rotation masses by approximately 10% with a best value of $M = 1.25$
$\pm 0.25 M_\odot$ and $M/L_V = 0.19 \pm 0.04 M_\odot/L_\odot$, consistent with naive arguments.

In order to check the dependence of the derived mass on the two highest residual velocity stars, masses were redetermined with these two stars eliminated. The results were a reduction in derived cluster mass of between 10% - 20% as r'_a varied from 5 pc to infinity. Clearly, the derived mass is quite sensitive to these two stars and will be biased too high if these are non-members or binaries. Conclusions concerning isotropy are probably not greatly affected by these two stars since removing them would result in orbits which appear even more isotropic than currently observed (i.e. highly anisotropic orbits produce a sharp rise in the projected core velocity dispersion). Another possible source of systematic error could arise from either an under or overestimate of the velocity uncertainties. Varying v_{err} by $\pm 50\%$ causes the derived mass to change by $\mp$ 20 - 35% as r'_a ranges from infinity to 5 pc.

2.4.5   Rotational Flattening

We are now in a position to calculate two dynamically interesting parameters: the mass-weighted mean-square rotation speed;

$$v_o^2 = \frac{\int \rho_E(r)[v_{rot}(\vec{r})]^2 d^3\vec{r}}{\int \rho_E(r)d^3\vec{r}} = 1.1 \pm 0.4 \ (\text{km s}^{-1})^2, \tag{2.20}$$

and the mass-weighted mean-square random velocity along the line of sight,

$$\sigma_o^2 = \frac{\int \rho_E(r)\sigma_x(\vec{r})^2 d^3\vec{r}}{\int \rho_E(r)d^3\vec{r}} = 5.5 \pm 1.1 \ (\text{km s}^{-1})^2, \tag{2.21}$$

(Binney and Tremaine 1987, p. 216). The values given are for the range $4 \leq r$ (pc)$\leq$ 12 as this is the region with the best determined values of ϵ ($\epsilon = 0.17 \pm 0.06$, see §2.2.4). Fig 2.8 shows a plot of v_o/σ_o vs ϵ. The solid line is the relationship for an edge-on oblate spheroid with ellipticity resulting exclusively from rotation (Binney 1978). Unfortunately, the uncertainties are quite large (particularly for v_o) and the most we can say is that NGC 1866 is consistent with being rotationally flattened.
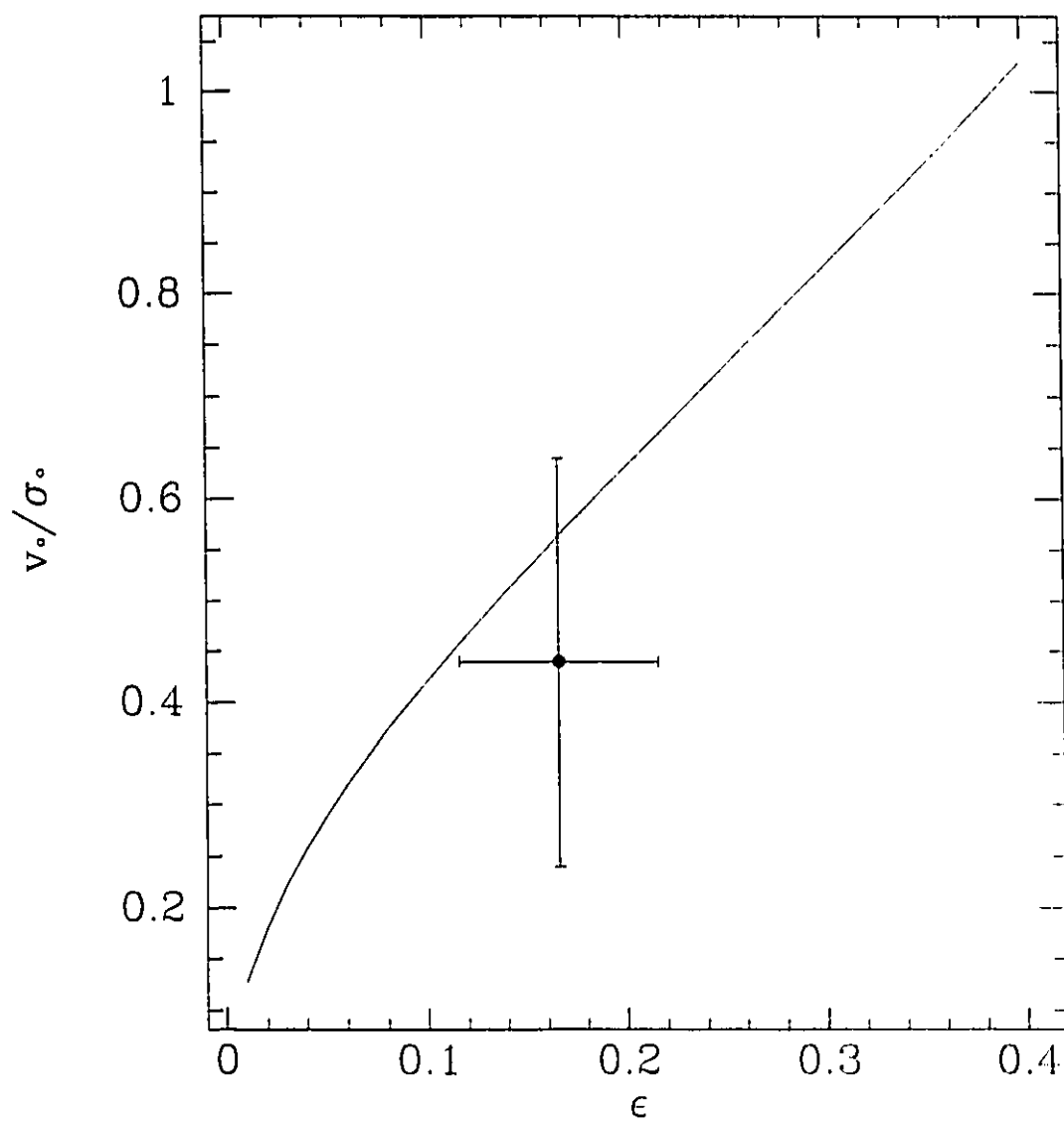
Fig. 2.8 - The solid line represents the $v_0/\sigma_0 - \epsilon$ relationship for rotationally-flattened oblate spheroids. The point represents the ratio for NGC 1866.

2.5   CONSTRAINTS ON THE MASS FUNCTION

The cluster M/L_V estimate can be used to constrain the slope of the initial mass function (IMF). In this study we used two forms for the IMF. The first is just a straight power-law given by

$$\phi(m) \propto m^{-(1+x)}, \tag{2.22}$$

which is useful to find the *average* IMF slope and the second is a more realistic two component power-law similar to the Miller-Scalo IMF for the solar neighborhood (Miller and Scalo 1979). This model uses the above $\phi(m)$ for $m > m_d$ and

$$\phi(m) \propto m^{-(1)}, \tag{2.23}$$

below m_d. This is not the exact form of the Miller-Scalo IMF but it does have a drop-off at the low mass end.

The theoretical cluster M/L_V is given by

$$\frac{M}{L_V} = \frac{\int_{m_l}^{m_u} m\phi(m)dm}{\int_{m_l}^{m_u} l(m)\phi(m)dm}, \tag{2.24}$$

where $l(m)$ is the luminosity of a star of mass m given by a theoretical mass-luminosity relationship for main-sequence and evolved stars. It is, therefore, necessary to find a mass-luminosity relationship which is applicable to this cluster. There have been two recent photometric studies of NGC 1866. Both used B, V stellar photometry to construct a color-magnitude diagram, and both use stellar models employing convective overshoot with X = 0.7, Y = 0.28, and Z=0.02 to determine cluster age. Brocato *et al.* (1989) obtain an age of $\tau = 1.1 \times 10^8$ years and Chiosi *et al.* (1989) obtain $\tau = 2.0 \times 10^8$ years, each using an independent set of isochrones. The turn-off masses, m_{to}, are 4.9 $M_\odot$ and 4.2 $M_\odot$, respectively. Although this is a large difference, perhaps it is not surprising as different evolutionary models were

used and, as pointed out by Welch *et al.* (1991), there is a zero point difference in the two sets of photometry of around $\Delta V = 0.15 - 0.20$ magnitudes. We, therefore, have a choice of two mass-luminosity relationships.

If $m_u > m_{to}$ then it is necessary to estimate masses for the stellar remnants. We consider only two cases: 1) Stars with initial masses $m_{to} \leq m_i \leq 8 M_\odot$ become white dwarfs with $m_{hr} = 1.2\ M_\odot$ and stars with $8\ M_\odot \leq m_i \leq m_u$ are ejected from the cluster as is consistent with the high velocities seen for pulsars in the disk (Gunn and Griffin 1979). Therefore, the choice of m_u is not important except for estimating the amount of mass lost from the cluster due to stellar evolution.

Table 2.6 shows the derived values of x (column 3 and 5) for 3 different m_l (column 1), and 5 different m_d (column 2). The 1 refers to the Brocato mass-luminosity relationship ($\tau = 1.0 \times 10^8$ years was the nearest available data), supplemented with the Vandenberg (1985) values in the range $0.7 \leq m\ (M_\odot) \leq 1.5$, and the 2 refers to the Chiosi values (found in Bertelli *et al.* 1990). Columns 4 and 6 contain the implied mean stellar mass for the given model. All values for x correspond to $M/L = 0.19 \pm 0.04$. The slopes for relationship 1 are consistently steeper than for relationship 2 because the younger age estimate results in a greater number of bright high-mass stars. In both cases, for all IMF slopes, the mass in white dwarfs comprises less than 2% of the total cluster mass. To give an idea of the amount of mass-loss experienced by the cluster due to stellar evolution we consider the $m_l = 0.1 M_\odot$ case. The mass lost for relationships 1 and 2, respectively, is 4 - 1 % and 20 - 2 % as m_d varies from 0 to $1.5_\odot$.

Elson, Fall, and Freeman (1989) have estimated the mass function slope using starcounts on photographic plates. They obtained an average slope of $x = 0.0$, a result which is clearly inconsistent with our findings. As can be seen from Table

Table 2.6

Mass Functions

m_l (M$_\odot$)	m_d (M$_\odot$)	1		2	
		x	$< m >$ (M$_\odot$)	x	$< m >$ (M$_\odot$)
0.05	0.0	1.64 ± 0.1	0.12	1.22 ± 0.1	0.17
0.05	0.3	2.00 ± 0.1	0.23	1.46 ± 0.15	0.29
0.05	0.5	2.28 ± 0.1	0.30	1.67 ± 0.15	0.35
0.05	1.0	3.04 ± 0.2	0.43	2.32 ± 0.25	0.47
0.05	1.5	4.08 ± 0.3	0.53	3.41 ± 0.5	0.55
0.1	0.0	1.82 ± 0.1	0.21	1.35 ± 0.1	0.28
0.1	0.3	2.05 ± 0.1	0.30	1.50 ± 0.15	0.37
0.1	0.5	2.32 ± 0.15	0.37	1.71 ± 0.2	0.44
0.1	1.0	3.07 ± 0.2	0.52	2.35 ± 0.2	0.57
0.1	1.5	4.11 ± 0.3	0.63	3.47 ± 0.5	0.66
0.15	0.0	1.96 ± 0.1	0.29	1.47 ± 0.15	0.37
0.15	0.3	2.10 ± 0.1	0.35	1.56 ± 0.15	0.43
0.15	0.5	2.36 ± 0.15	0.43	1.76 ± 0.2	0.50
0.15	1.0	3.10 ± 0.2	0.59	2.41 ± 0.3	0.64
0.15	1.5	4.15 ± 0.3	0.71	3.54 ± 0.5	0.74

2.6, it would take a rather extreme modification in the parameters or in the mass-luminosity relationship to achieve this value. More recently, Mateo (1990), using CCD images and profile-fitting photometry, has derived an *average* mass-function slope of $x = 1.4$ which is consistent with the dynamically derived value.

2.6 CONCLUSIONS

In this paper we have examined the internal dynamics of the young LMC cluster NGC 1866 using V-band CCD images and echelle spectra of 69 supergiants. Projected radii for the stars range from $0.1 \leq$ R (pc) ≤ 44.0 and the mean estimated velocity error is $v_{err} \approx 1.0$ km s^{-1}. The mean cluster velocity is $v_{ave} = 301.2 \pm 1.0$ km s^{-1} where the uncertainty is primarily due to the definition of the standard system.

1) A V-band luminosity profile was constructed out to projected radii of R > 100 pc. Single component King-Michie models were applied to this data in order to determine the most favorable value for the anisotropy radius and the total cluster luminosity. The luminosity varied from L = 5.5 - 6.0 $\times 10^5$ $L_\odot$ as r_a went from $2r_s$ to infinity (isotropic) and the best fit occurred for $r_a = 3r_s$. This model provides a better fit than an isotropic model, but the validity of all the models is suspect as there is strong evidence for cluster rotation which has not been incorporated into the King-Michie distribution functions.

2) A power-law model was applied to the surface photometry resulting in the functional form

$$\mu_V(R) = 4.6 \times 10^3 [1 + (R/4.05(pc))^2]^{-2.72/2} \ L_\odot pc^{-2},$$

and the total integrated V luminosity is $L_{V_\infty} = 6.5 \pm 0.3 \times 10^5$ $L_\odot$. The quality of the fit was similar to that of the best King-Michie model. This model can be deprojected to derive an empirical spatial density distribution.

3) A star-subtracted, median-filtered U frame was used to determine photometric shape parameters. In the region $4 \leq R$ (pc) ≤ 12 The cluster has an mean ellipticity of $\epsilon = 0.17 \pm 0.06$ and a minor axis position angle $\alpha = 125° \pm 5°$

4) The rather small number of stellar radial velocities hindered our ability to quantify the rotation, however, it appears that the rotation axis has a position angle of $100° \pm 25°$ and that the peak rotation is 1.3 ± 0.5 km s^{-1} at R $\approx$ 10 - 15 pc.

5) A value of $v_0/\sigma_0 = 0.4 \pm 0.2$ was obtained. Within the rather large uncertainty, this is consistent with NGC 1866 being a rotationally-flattened, oblate spheroid.

6) Two separate techniques were employed in order to estimate the cluster mass.

    a) King-Michie models with anisotropy radii ranging from 2 r_s to infinity yielded M = 1.20 - 1.40 $\pm 0.25 \times 10^5$ $M_\odot$ resulting in a $M/L_V = 0.20 - 0.24$

± 0.04 $M_{\odot}/L_{\odot}$. The photometric data were in best agreement with low values for r_a while large r_a values gave the best fits to the velocity data. Perhaps this is an indication that the King-Michie models do not describe the data well.

b) The empirical model of the density distribution was coupled to Jeans' equation to generate velocity distributions for models with anisotropy radii ranging from $5 \le r'_a$ (pc)$\le \infty$. Values of $M_{\infty} = 1.25 \pm 0.25 \times 10^5 M_{\odot}$ and $M_{\infty} = 1.35 \pm 0.25 \times 10^5 M_{\odot}$ were obtained for models with and without rotation, respectively, corresponding to $M/L_V = 0.19 \pm 0.04$ or 0.21 ± 0.05 in solar units. Models with isotropic orbits or perhaps a slight degree of anisotropy were in best agreement with the data and models with rotation resulted in significantly superior fits.

7) Values for the slope of the mass function were determined using the derived M/L_V, artificial mass-luminosity relationships, and several forms for the IMF. The best values for the average slope are $x = 1.35 \pm 0.1$ for $\tau = 2.0 \times 10^8$ years and $x = 1.82 \pm 0.1$ for $\tau = 1.0 \times 10^8$ years.

ACKNOWLEDGEMENTS

CHAPTER 3

DYNAMICS OF THE INTERMEDIATE-AGE ELLIPTICAL LMC CLUSTER NGC 1978

3.1 INTRODUCTION

Globular clusters present a unique opportunity to study the internal dynamics of resolved stellar systems in which the two-body relaxation timescales are similar to the current ages. One can kinematically examine clusters to dynamically determine masses and mass-to-light ratios (hereafter, M/L's) in order to constrain the initial mass function (IMF). Attempts can also be made to determine the internal cluster dynamics at various stages in their evolution to try to form a coherent picture of

formation, energy equipartition, and mass segregation. At later evolutionary stages, gravothermal catastrophe and the resulting core collapse can be studied.

In the Milky Way, these studies can be broken down into two subsets: 1) those which utilize measurements of central radial velocity dispersions from integrated spectra (c.f., Illingworth 1976), and 2) radial velocity measurements of individual member stars (c.f., Gunn and Griffin 1979, Meylan and Mayor 1986, Lupton *et al.* 1987, Pryor *et al.* 1989 and 1991 and others).

The Large Magellanic Cloud (LMC) clusters occupy a much wider range in parameter space (i.e. age, metallicity, morphology, etc., see Olszewski *et al.* 1991) than their Milky Way counterparts and, hence, provide a more complete cluster sample. To date there have been several dynamical studies of LMC clusters including integrated spectra for several old clusters (Elson and Freeman 1985; Dubath *et al.* 1990; and Mateo *et al.* 1991) and individual stellar velocity measurements of mostly young clusters (Lupton *et al.* 1989, Mateo *et al.* 1991, Fischer *et al.* 1992a).

An interesting aspect of the cluster age distribution is that it does not appear to be a continuum. There are approximately eight old (i.e. $> 10^{10}$ yrs) clusters and then a large number of clusters younger than 3×10^9 yrs, possibly indicating two major epochs of star formation interrupted by a more quiescent period (Olszewski *et al.* 1991). Another interesting feature of some LMC clusters is the existence of projected ellipticities as large as $\epsilon \approx 0.3$ (Geisler and Hodge 1980) - a feature not restricted to the young clusters. For this reason, we have embarked upon a project to dynamically study a sample of LMC clusters covering a range of ages and ellipticities.

NGC 1978 is an intermediate age cluster ($\tau = 2 \times 10^9$ years, Olszewski 1984 and Mould and Da Costa 1988) which also happens to be among the most highly elliptical clusters known ($\epsilon = 0.3$, Geisler and Hodge 1980). Three explanations for this

ellipticity immediately suggest themselves: rotation, an anisotropic velocity dispersion tensor, or a recent cluster-cluster merger. In this paper we will investigate the relative likelihoods of these three scenarios and attempt to constrain the dynamics of this largely unrelaxed object (except, perhaps, in the innermost regions).

A discussion of the the surface photometry data and reductions will be presented in §2, with the modeling results appearing in §3. §4 contains a description of the spectroscopic observations and reductions and in §5 we calculate evolutionary timescales. §6 details the M/L determinations and constraints on the internal dynamics, and in §7 we compare our findings with two previous studies.

3.2   SURFACE PHOTOMETRY

3.2.1   Observations and Reductions

In order to derive a surface brightness profile for NGC 1978, BV CCD frames were obtained on the Las Campanas Observatory (LCO) 1.0 m telescope on 1991 January 22. The TEK2 1024^2 chip was used (readout noise $= 6$ e$^-$, gain $= 2$ e$^-$/ADU, and angular scale $= 0.61''$ pix^{-1}). The integration times were 200s and 100s for the B and V frames, respectively.

There are two complications to measuring the surface brightness profile of NGC 1978. First, the cluster is in an area densely populated with LMC field stars, and second, elliptical apertures are necessary.

To maximize the surface brightness intensity range, it is necessary to get an accurate estimate of the field contribution. The apparent BV color-magnitude diagram (Fig. 3.1) illustrates the richness of the NGC 1978 field. One can see a clearly delineated red giant branch consisting of both cluster and LMC field stars. However, there are also a similar number of blue, main sequence LMC field stars. The presence of these bright stars complicates the background determination and

therefore it is advantageous to remove them. This was accomplished using the profile-fitting photometry package DAOPHOT (Stetson 1987). All stars bluer than $B-V = 0.48$ and all stars brighter than $V = 15.1$ were removed (above and to the left of the solid line in Fig. 3.1). We found that after star-subtraction the mean background brightness was only reduced by about 10-15% but that its uncertainty decreased by more than a factor of ten.

Because NGC 1978 is one of the most elliptical clusters known, it requires the use of elliptical annuli for surface photometry which in turn requires knowledge of the mean cluster ellipticity and major axis position angle. The many resolved stars greatly complicate attempts to derive ellipticities, tending to skew them towards high values and yielding rapidly varying position angles as a function of radius. Therefore, we first subtracted out the resolved (both background and cluster) stars using DAOPHOT and then median filtered the star-subtracted image using a $9''$ radius circular filter. The result was a relatively smooth light distribution with the contribution from the bright giants largely eliminated. It was then possible to use the ELLIPSE task in the IRAF[1] STSDAS package, which uses the technique of Jedrzejewski (1987), to fit elliptical contours to a smooth light distribution. We were only able to employ this technique reliably in the range $2.5 \leq R$ (pc) ≤ 25 (Throughout this paper, we assume a distance to NGC 1978 of 50 kpc and hence an angular scale of $4.12''$ pc^{-1}) due to crowding at smaller radii and a lack of light at larger radii.

Table 3.1 lists the ellipse parameters as a function of major axis radius. Column 1 is the radius of the projected major axis in pc, while columns 2 and 4 are the projected ellipticities and columns 3 and 5 are the major axis position angles (PA) for

---

[1]   IRAF is distributed by the National Optical Astronomy Observatories, which is operated by the Association of Universities for Research in Astronomy, Inc., under contract to the National Science Foundation.
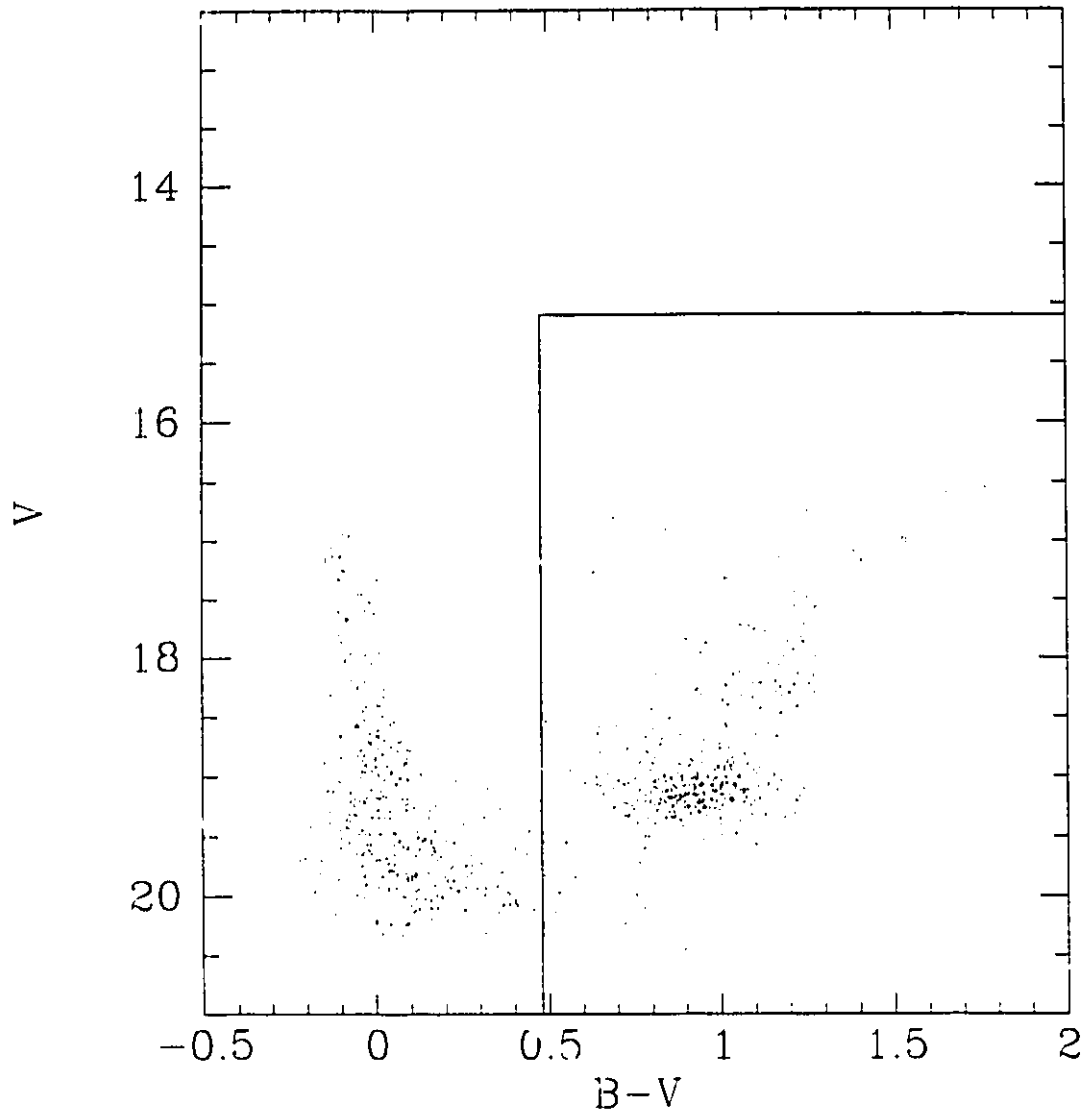
Fig. 3.1 - Apparent BV color-magnitude diagram for NGC 1978. Stars above and to the left of the solid line were subtracted prior to surface brightness measurements.

the B and V frames, respectively. The tabulated uncertainties represent the formal

fitting errors. Fig. 3.2 shows isophotal contour diagrams for the star-subtracted

median-filtered BV frames. Superimposed on the contours are the best-fit ellipses.

The ellipses appear to provide very reasonable models for the isophotes in the range

shown. There is no evidence for subclustering, indicating that NGC 1978 is unlikely

to be a recent merger of two clusters. Finally, 14 stars from the Guide Star Catalog

(Lasker *et al.* 1990, Russell *et al.* 1990, and Jenkner *et al.* 1990) that appeared on

the V frame were used to accurately align the frames to the J2000.0 equinox. The

rms residuals for the positional fit were less than 0.8 arcsec. The cluster center is

located at $\alpha(2000) = 5{:}28{:}44.8$ and $\delta(2000) = -66{:}14{:}09.9$.

Table 3.1

Ellipticity and Position Angle

a (pc)	B		V	
	ϵ	PA (°)	ϵ	PA (°)
2.9	0.33 ± 0.01	164.0 ± 2.0	0.29 ± 0.01	161.0 ± 2.0
5.2	0.33 ± 0.02	147.0 ± 2.0	0.28 ± 0.02	158.0 ± 3.0
7.6	0.25 ± 0.03	151.0 ± 4.0	0.20 ± 0.03	154.0 ± 4.0
10.1	0.28 ± 0.02	148.0 ± 2.0	0.25 ± 0.02	148.0 ± 2.0
13.4	0.31 ± 0.04	146.0 ± 4.0	0.30 ± 0.02	148.0 ± 3.0
17.8	0.31 ± 0.04	146.0 ± 4.0	0.33 ± 0.03	148.0 ± 3.0
21.6	0.34 ± 0.03	147.0 ± 3.0	0.34 ± 0.03	147.0 ± 3.0
Mean	0.32 ± 0.02	151.0 ± 7.0	0.29 ± 0.03	153.0 ± 6.0

For both frames, a mean representative ellipticity and position angle were de-

termined and these are shown at the bottom of Table 3.1. These values agree

well with those obtained photographically by Geisler and Hodge (1980) $'\epsilon = 0.30\pm$

0.06 and PA = $159° \pm 7.0°$) and were used to construct the elliptical annuli for

the flux measurements. Surface photometry was performed in a manner similar
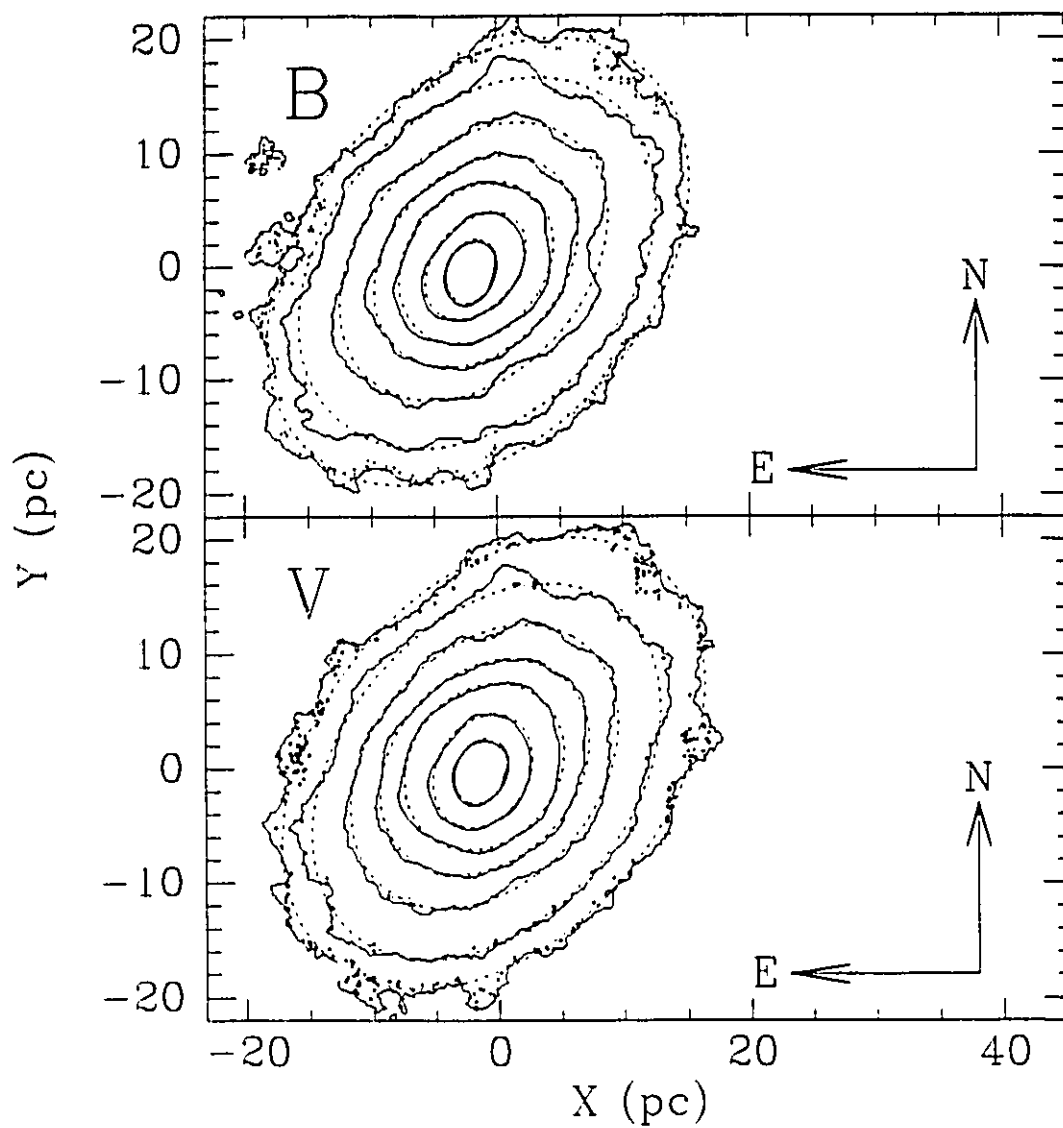
Fig. 3.2 - Plot of elliptical contours fit to star-subtracted and median-filtered BV CCD images. The solid lines are the isophotes and the dashed lines are the best fit ellipses. The elliptical parameters are tabulated in Table 3.1.

to Djorgovski (1988). The frames were broken up into a series of concentric el-
liptical annuli centered on the cluster. The annuli were further divided into eight
azimuthal sectors. The average pixel brightness was determined for each sector in a
given annulus and the *median* of the eight separate measurements was taken as the
representative brightness at the area-weighted average radius of the annulus (i.e.,
the mean radius of all the pixels within the annulus which is approximately equal
to the geometric mean). The standard error of the median of the eight sectors is
equal to the standard error of the mean multiplied by $\sqrt{\pi/2}$ and this was adopted
as the photometry uncertainty in each annulus. Comparisons between photome-
try measured with elliptical and circular apertures revealed that, while the circular
apertures did not introduce significant systematic errors, they tended to have sub-
stantially higher sector-to-sector variations which resulted in greater scatter in the
surface photometry.

A background level (a combination of sky light and Galactic foreground and
remaining LMC field stars) was estimated from regions at large projected distances
from the cluster. We found that the surface brightness profiles tended to level out
beyond 65 pc for the B frame and about 55 pc for the V (both of these distances
are along the major axis). By "levelling out" we don't necessarily mean that the
cluster light does not extend beyond this point but simply that fluctuations in the
background dominate to such an extent that it is no longer possible to observe the
profile declining in intensity. Therefore, it was this region that was used for the
background determinations.

The cluster was reobserved on 1991 Dec 7 in order to calibrate the photome-
try. Fourteen BV observations of 8 E-region standards (Menzies *et al.* 1989) were
observed on the same night covering an airmass range of 1.1 - 2.0 and a color range
of 0.1 mag $\leq$ B-V $\leq$ 1.6 mag. The rms of the adopted solution was less than 0.02

mag and the zero point had a similar accuracy. $E_{B-V} = 0.06$ mag, consistent with Olszewski (1984), was adopted. The background-subtracted surface photometry data is presented in Table 3.2 [assuming $M_{V\odot} = 4.83$ and $(B\text{-}V)_\odot = 0.65$, Mihalas and Binney 1981, p. 60]. Columns 1 and 4 are the projected area-weighted radii, columns 2 and 5 are the projected major axis radii and columns 3 and 6 are the B and V surface profiles, respectively. The background values for the B and V frames were, respectively, $134.3 \pm 0.4 \ L_{B\odot} \ \text{pc}^{-2}$ and $148.1 \pm 0.7 \ L_{V\odot} \ \text{pc}^{-2}$. Fig. 3.3 is a plot of the B and V surface brightness profiles. Also shown is a typical stellar profile which has a FWHM approximately a factor of ten smaller than the core radius (see §3.2.2); hence seeing will have a negligible effect on measurements of this quantity (Mihalas and Binney 1981, p. 315). We looked for a radial B-V color gradient in the cluster but concluded that no significant effect is present within our measurement uncertainties.

3.2.2   King-Michie Models

Despite the fact that the highly elliptical shape of NGC 1978 is a clear indication that its dynamics cannot be adequately described within the standard framework of the King-Michie (KM) formulation (King 1966 and Michie 1963), we fitted multi-component KM models to the photometry data. The reasons for this are: 1) These models provide us with classification parameters adhering to a widely used scheme and thus enable potentially fruitful comparisons to other clusters. 2) The fit provides for a reasonably accurate means of determining the total cluster light and 3) the fit, in conjunction with the radial velocity data (§3.3), gives a first approximation to the cluster mass. Alternate models will be discussed in §3.5.2.

For the KM models, the stellar mass spectrum is sub-divided into mass classes; nine were used for NGC 1978 (see Table 3.3). Each mass class has an energy and

Table 3.2

Surface Photometry

R (pc)	a (pc)	L_B ($L_{B\odot}$ pc^{-2})	R (pc)	a (pc)	L_V ($L_{V\odot}$ pc^{-2})
0.4	0.5	1886.0 ± 140.0	0.4	0.5	2406.0 ± 305.0
0.6	0.7	1668.0 ± 137.0	0.6	0.7	2142.0 ± 199.0
0.8	1.0	1697.0 ± 92.0	0.8	0.9	1813.0 ± 141.0
1.0	1.2	1599.0 ± 88.0	1.0	1.2	1678.0 ± 88.0
1.3	1.5	1479.0 ± 107.0	1.3	1.4	1469.0 ± 189.0
1.6	1.9	1429.0 ± 121.0	1.6	1.8	1674.0 ± 146.0
2.0	2.4	1478.0 ± 72.0	2.0	2.3	1806.0 ± 170.0
2.6	3.0	1195.0 ± 58.0	2.5	2.9	1266.0 ± 77.0
3.2	3.8	1018.0 ± 38.0	3.2	3.6	1049.0 ± 38.0
4.1	4.8	829.0 ± 47.0	4.0	4.6	910.0 ± 73.0
5.1	6.0	687.0 ± 24.0	5.0	5.8	755.0 ± 41.0
6.5	7.6	496.0 ± 22.0	6.3	7.3	507.0 ± 30.0
8.2	9.5	320.0 ± 11.0	7.9	9.1	324.0 ± 27.0
10.3	12.0	201.0 ± 8.2	10.0	11.5	213.0 ± 15.0
12.9	15.1	134.0 ± 9.6	12.6	14.5	136.0 ± 12.0
16.3	19.0	73.0 ± 2.5	15.8	18.2	78.0 ± 7.4
20.5	24.0	35.0 ± 5.4	20.0	23.0	38.0 ± 7.7
25.8	30.2	15.0 ± 3.1	25.1	28.9	15.0 ± 3.7
32.4	38.0	8.6 ± 3.7	31.6	36.4	7.2 ± 3.3
40.9	47.8	3.5 ± 2.3	39.8	45.8	3.6 ± 1.6
51.4	60.2	0.2 ± 1.9			

angular momentum per unit mass (E and J, respectively) distribution function given by

$$f_i(E = -0.5v^2 + W, J) \propto e^{-[J/(2v_a r_a)]^2}[e^{A_i E} - 1], \qquad (3.1)$$

where v_a is the scale velocity, W is the reduced gravitational potential, and r_a is the anisotropy radius beyond which stellar orbits become increasingly radial. The A_i are constants discussed below. The details are thoroughly described in Gunn and Griffin (1979), but briefly, the shape of the density distribution for the KM models, $\rho(r)$, is determined by solving Poisson's equation and is dependent on three parameters: the reduced central potential W_0, the anisotropy radius r_a, and the
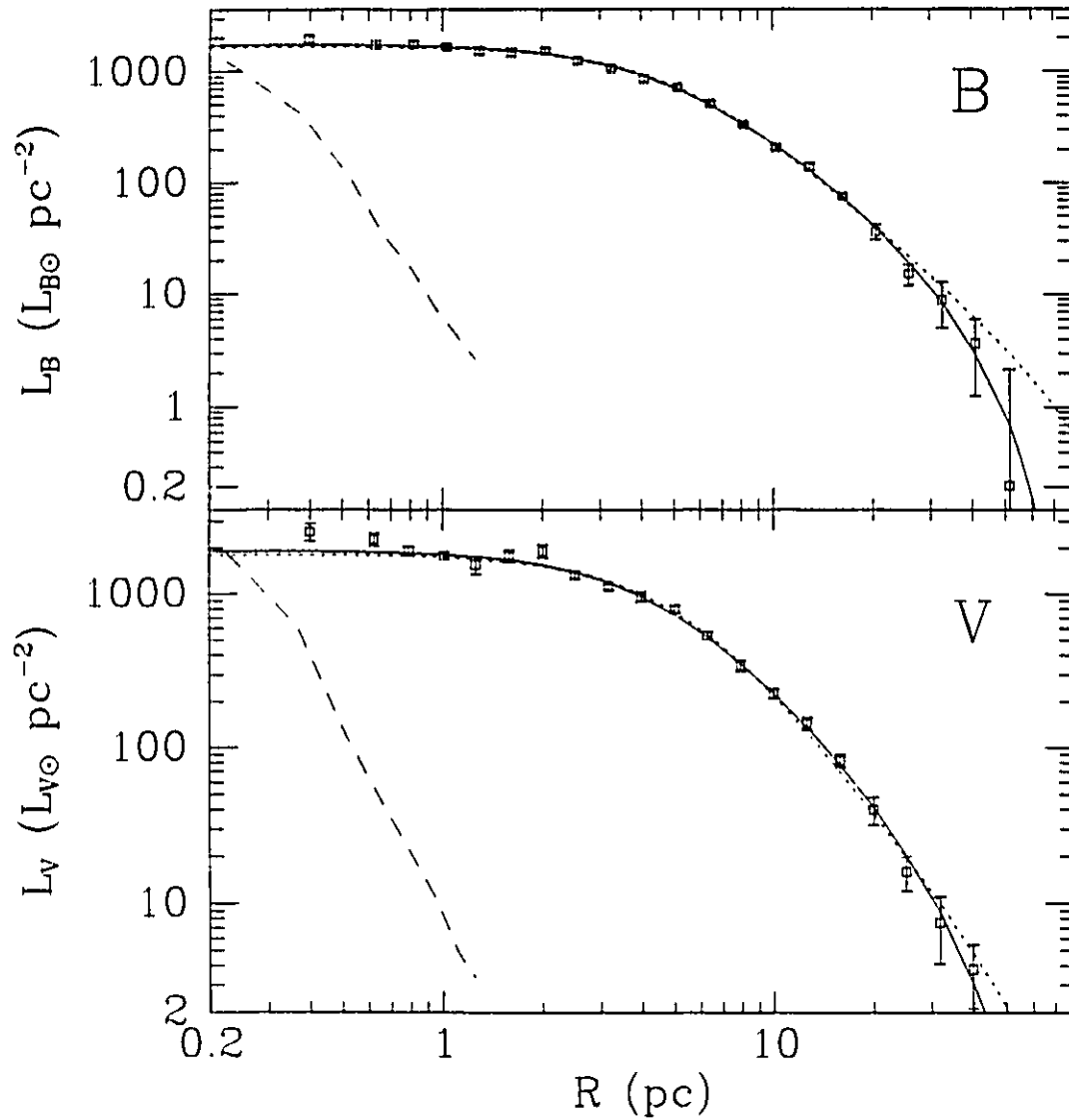
Fig. 3.3 - CCD BV luminosity profiles for NGC 1978. The solid lines are the single-mass isotropic KM models, while the short-dashed lines are the multi-mass $x = 1.0$ isotropic models. The long-dashed lines are typical stellar profiles (FWHM approximately one tenth the cluster core radius).

slope of the mass function, x, given by

$$\phi(m) = m^{-(x+1)} \; dm \qquad\qquad m \geq 0.3 M_\odot, \qquad\qquad (3.2)$$

$$\phi(m) = m \; dm \qquad\qquad m < 0.3 M_\odot.$$

Scaling is applied in both the radial (r_s) and luminosity dimensions to yield the best fit to the surface photometry data. A_i is forced to be proportional to the mean mass of stars in the ith mass class, which approximates equipartition of energy in the cluster center.

Table 3.3
Mass Bins

Bin	m_{min} $(M_\odot)$	m_{max} $(M_\odot)$
1	0.16	0.30
2	0.30	0.45
3	0.45	0.60
4	0.60	0.75
5	0.75	0.90
6	0.90	1.05
7	1.05	1.20
8	1.20	1.43
9	1.43	1.65

The reason that choosing the A_i in the above manner does not yield true equipartition of energy is that the lower mass stars are more affected by the energy cut-off implicit in the model than are the higher mass stars (Pryor *et al.* 1986). It turns out that the deviations in equipartition seen in the KM models are qualitatively similar to what is calculated in theoretical multi-mass evolutionary models. That is, they both exhibit a tendency for the high-mass stars to have higher kinetic energies. For example, in the $x = 0.0$ isotropic KM model described below, the lowest mass class has roughly one-third the kinetic energy of the highest mass class

at the cluster center. In Fokker-Planck models, the cluster relaxes and equipartition begins to occur. Specifically, the kinetic energy of the higher mass stars decreases while that of the lower mass stars remains fairly constant. This results in mass segregation, with the high mass stars migrating to smaller radii and hence an effective decoupling of the different mass classes. With the greatly lowered rate of interactions, it becomes difficult for energy exchange between different mass stars to occur and core equipartition cannot be fully achieved (Inagaki and Saslaw 1985, see also Spitzer 1969 for an analytical treatment of a two-mass system).

In order to apply the multi-mass KM models to the NGC 1978 data we adopted stellar BV mass-luminosity relationships which were a combination of Bergbusch & VandenBerg (1992) in the range $0.15 \leq m$ ($M_\odot$) ≤ 0.70 and Bertelli et al. (1990) in the range $0.70 \leq m$ ($M_\odot$) ≤ 1.65. We assumed an age of 2×10^9 years and a metallicity of $z = 0.004$ (Mould and Da Costa 1988, and Olszewski 1984). The models of Bertelli et al. incorporate convective overshooting and mass-loss, both associated with high mass stars, while the VandenBerg models incorporate neither of these and should be valid in the low mass regime. The treatment of Pryor et al. 1986 was adopted for remnants: stars with initial masses of 1.65 - 4.0 $M_\odot$ and 4.0 - 8.0 $M_\odot$ become white dwarfs with masses of 0.7 $M_\odot$ and 1.2 $M_\odot$, respectively. These objects are added to the corresponding mass bins. More massive stars, which have presumably evolved into neutron stars, are assumed to be ejected from the cluster in agreement with the typically large velocities observed for these objects in the field (Gunn and Griffin 1979). Clearly, this assumption is not strictly correct as pulsars have been detected in several galactic globular clusters.

Tables 4 and 5 (B and V, respectively) contain the fitted KM parameters for models with parameters ranging from isotropic orbits to $r_a = 5$ r_s and $0.0 \leq x \leq 2.0$. Column 1 is the anisotropy radius, column 2 is the mass function slope,

column 3 is the reduced central potential, column 4 is the scale radius, column 5 is the ratio of the tidal radius to the scale radius and columns 6 and 7 are the reduced chi-squared for the fit (B has 18 and V has 17 degrees of freedom) and the probability of exceeding this value, respectively. These probabilities are based on 1000 Monte Carlo simulations for each parameter set, each using a surface profile generated from the best fit model with errors drawn from the uncertainties shown in Table 3.2. Hence, the probabilities are somewhat dependent on the accuracy of the photometry uncertainties and for this reason it is safer to view them in the relative sense. All the KM parameters are based on using surface brightness profiles expressed as a function of area-weighted radius (from columns 1 and 4 of Table 3.2). The remaining columns of the two tables will be discussed in §3.5.1.

Tables 6 and 7 contain the derived model parameters: columns 1 and 2 specify the anisotropy radius and mass function slope, while columns 3 and 4 contain the central luminosity density and total cluster luminosity, respectively. Columns 7 and 8 are the central and global *population* M/L's given by

$$\frac{M}{L_V} = \frac{\int_{m_l}^{m_u} m\phi(m)dm}{\int_{m_l}^{m_u} l(m)\phi(m)dm},$$
(3.3)

where $l(m)$ is the luminosity of a star of mass m given by a theoretical mass-luminosity relationship for main-sequence and evolved stars and m_l and m_u are the lower and upper mass cut-offs, respectively. The remaining columns will be discussed in §3.5.1.

We have plotted two of the KM models in Fig. 3.3; isotropic single-mass models and isotropic $x = 1.0$ models. The difference in the quality of the fits results from the tendency of the multi-mass models to have shallower density fall-offs which is not seen in the data.

<div align="center">

Table 3.4
King-Michie - B Band Fitted Parameters

</div>

r_a x (r_a)		Photometry					Velocities		
		W_0	r_a (pc)	c	χ^2_ν ($\nu = 18$)	$P(\chi^2_\nu)$	v_s (km s^{-1})	ζ^2	$P(\zeta^2)$
ISO		5.9 ± 0.2	4.6 ± 0.2	17.0 ± 2.0	0.75	0.74	2.33 ± 0.5	33.79	0.71
10		5.9 ± 0.2	4.6 ± 0.2	18.0 ± 2.0	0.78	0.70	2.34 ± 0.5	33.85	0.70
5		5.8 ± 0.2	4.8 ± 0.2	22.0 ± 4.0	0.90	0.53	2.38 ± 0.5	33.99	0.67
ISO	0.0	6.9 ± 0.4	5.6 ± 0.2	21.0 ± 4.0	1.21	0.20	2.31 ± 0.5	33.00	0.84
10	0.0	6.9 ± 0.4	5.5 ± 0.2	24.0 ± 6.0	1.27	0.16	2.32 ± 0.5	33.07	0.83
5	0.0	7.4 ± 0.1	5.7 ± 0.1	68.0 ± 30.0	1.32	0.17	2.31 ± 0.5	33.20	0.81
ISO	0.5	7.5 ± 0.4	5.7 ± 0.2	24.0 ± 4.0	1.33	0.13	2.28 ± 0.5	32.89	0.85
10	0.5	7.6 ± 0.4	5.7 ± 0.2	29.0 ± 8.0	1.36	0.12	2.28 ± 0.5	32.96	0.85
5	0.5	7.8 ± 0.1	5.7 ± 0.1	90.0 ± 30.0	1.34	0.16	2.30 ± 0.5	33.15	0.82
ISO	1.0	9.0 ± 0.4	5.6 ± 0.2	33.0 ± 6.0	1.47	0.09	2.22 ± 0.5	32.77	0.87
10	1.0	9.3 ± 0.2	5.4 ± 0.1	61.0 ± 13.0	1.39	0.17	2.22 ± 0.5	32.85	0.86
5	1.0	8.4 ± 0.1	5.9 ± 0.1	95.0 ± 35.0	1.48	0.09	2.29 ± 0.5	33.07	0.83
ISO	1.5	11.0 ± 0.2	5.5 ± 0.1	51.0 ± 4.0	1.51	0.11	2.18 ± 0.5	32.71	0.87
10	1.5	10.6 ± 0.2	5.6 ± 0.1	93.0 ± 26.0	1.30	0.20	2.19 ± 0.5	32.81	0.86
5	1.5	9.1 ± 0.1	6.3 ± 0.1	101.0 ± 30.0	1.94	0.01	2.31 ± 0.5	33.01	0.84
ISO	2.0	13.4 ± 0.2	5.4 ± 0.1	72.0 ± 5.0	1.40	0.21	2.16 ± 0.5	32.70	0.87
10	2.0	11.8 ± 0.3	6.0 ± 0.1	105.0 ± 36.0	1.54	0.10	2.23 ± 0.5	32.78	0.86
5	2.0	9.9 ± 0.1	6.8 ± 0.1	102.0 ± 15.0	2.97	0.00	2.35 ± 0.5	32.95	0.84

The results of the KM surface brightness modeling can be summarized as follows: 1) The parameters derived from the two surface profiles are, in general, consistent. The B band profile, despite having smaller tabulated uncertainties, appears to yield substantially lower χ^2_ν. Clearly, the B profile is much less sensitive to local luminosity fluctuations caused by cluster giants. 2) The single-mass models give the best quality fits to the data for all values of r_a with the best agreement observed for the isotropic model. 3) For the multi-mass models there is a trend toward poorer quality fits with steeper mass functions but the surface brightness distributions are not sufficiently well-determined to confidently choose a specific model. 4) The surface photometry is inadequate to unambiguously discriminate between models with

Table 3.5

King-Michie - V Band Fitted Parameters

| r_a (r$_s$) | x | \multicolumn{5}{c}{Photometry} | \multicolumn{3}{c}{Velocities} |
		W_0	r_s (pc)	c	χ^2_ν ($\nu=17$)	$P(\chi^2_\nu)$	v_s (km s^{-1})	ζ^2	$P(\zeta^2)$
ISO		6.0 ± 0.2	4.3 ± 0.2	18.0 ± 2.0	1.27	0.18	2.35 ± 0.5	33.84	0.70
10		5.9 ± 0.2	4.4 ± 0.2	19.0 ± 3.0	1.29	0.17	2.35 ± 0.5	33.91	0.69
5		5.7 ± 0.2	4.6 ± 0.2	21.0 ± 6.0	1.37	0.12	2.40 ± 0.5	34.10	0.65
ISO	0.0	6.7 ± 0.4	5.5 ± 0.2	20.0 ± 4.0	1.64	0.04	2.35 ± 0.5	33.05	0.83
10	0.0	6.7 ± 0.5	5.5 ± 0.2	22.0 ± 7.0	1.67	0.03	2.35 ± 0.5	33.12	0.82
5	0.0	7.3 ± 0.4	5.4 ± 0.2	65.0 ± 30.0	1.74	0.03	2.35 ± 0.5	33.26	0.80
ISO	0.5	7.3 ± 0.5	5.5 ± 0.2	22.0 ± 5.0	1.71	0.03	2.30 ± 0.5	32.93	0.85
10	0.5	7.2 ± 0.6	5.6 ± 0.2	24.0 ± 8.0	1.73	0.03	2.30 ± 0.5	33.01	0.84
5	0.5	7.7 ± 0.3	5.5 ± 0.2	71.3 ± 40.0	1.72	0.03	2.30 ± 0.5	33.19	0.81
ISO	1.0	8.2 ± 0.6	5.7 ± 0.3	25.0 ± 6.0	1.82	0.02	2.30 ± 0.5	32.81	0.86
10	1.0	9.1 ± 0.6	5.3 ± 0.3	50.0 ± 24.0	1.79	0.02	2.25 ± 0.5	32.87	0.86
5	1.0	8.4 ± 0.2	5.7 ± 0.2	94.5 ± 35.0	1.74	0.03	2.30 ± 0.5	33.10	0.83
ISO	1.5	10.5 ± 0.4	5.5 ± 0.2	43.0 ± 6.0	1.87	0.02	2.20 ± 0.5	32.72	0.87
10	1.5	10.4 ± 0.4	5.4 ± 0.2	73.0 ± 35.0	1.73	0.03	2.20 ± 0.5	32.82	0.84
5	1.5	9.1 ± 0.1	6.0 ± 0.2	89.3 ± 35.0	1.93	0.02	2.30 ± 0.5	33.03	0.83
ISO	2.0	12.9 ± 0.3	5.3 ± 0.2	64.0 ± 8.0	1.80	0.02	2.20 ± 0.5	32.70	0.87
10	2.0	11.7 ± 0.2	5.8 ± 0.2	93.0 ± 25.0	1.78	0.02	2.25 ± 0.5	32.79	0.86
5	2.0	9.9 ± 0.1	6.5 ± 0.2	99.0 ± 17.0	2.33	0.00	2.35 ± 0.5	32.98	0.84

differing degrees of anisotropy. 5) For the multi-mass models the global population M/L's are not well constrained, varying by a factor of five. However, the central population M/L's occupy a much narrower range, only varying between 0.08 - 0.14 $M_\odot/L_{B\odot}$ and 0.10 - 0.17 $M_\odot/L_{V\odot}$. Because the integrated cluster luminosity is overwhelmingly attributable to the giants, the total number of giant stars is fairly insensitive to the slope of the mass function (i.e. one needs the same number of giants to produce the cluster luminosity). As a result of the equipartition of energy, the low mass stars tend to be located at large radii and, due to their relatively low luminosities, have little effect on the measured surface brightness profile; the total

Table 3.6

King-Michie - B Band Derived Parameters

r_a (r_s)	x	L_{B0} ($L_{B\odot}$ pc^{-3})	L_B ($10^5 L_{B\odot}$)	ρ_0 ($M_\odot$ pc^{-3})	M ($10^5 M_\odot$)	Population		Dynamical	
						$(M/L_B)_0$ $(M/L_B)_\odot$	(M/L_B) $(M/L_B)_\odot$	$(M/L_B)_0$ $(M/L_B)_\odot$	(M/L_B) $(M/L_B)_\odot$
ISO	0.0	200.0±10.0	3.10±0.08	52.0±20.0	0.70±0.30			0.21±0.08	0.21±0.08
10	0.0	197.0±10.0	3.14±0.08	52.0±20.0	0.70±0.30			0.20±0.08	0.20±0.08
5	0.0	192.0±10.0	3.21±0.11	50.0±20.0	0.70±0.30			0.20±0.08	0.20±0.08
ISO	0.0	182.0±8.0	3.30±0.12	28.0±10.0	1.20±0.45	0.15	0.33	0.14±0.06	0.34±0.15
10	0.0	178.0±8.0	3.32±0.13	28.0±10.0	1.20±0.45	0.15	0.33	0.14±0.06	0.34±0.15
5	0.0	174.0±11.0	3.64±0.07	28.0±10.0	1.45±0.50	0.13	0.34	0.14±0.06	0.38±0.15
ISO	0.5	178.0±8.0	3.33±0.13	27.0±11.0	1.40±0.50	0.12	0.34	0.14±0.06	0.40±0.15
10	0.5	177.0±8.0	3.37±0.14	27.0±11.0	1.45±0.50	0.12	0.33	0.13±0.06	0.40±0.15
5	0.5	171.0±11.0	3.58±0.07	27.0±11.0	1.75±0.50	0.11	0.34	0.14±0.06	0.44±0.20
ISO	1.0	178.0±8.0	3.50±0.14	26.0±10.0	2.10±0.85	0.10	0.42	0.13±0.06	0.55±0.25
10	1.0	185.0±7.0	3.61±0.09	28.0±11.0	2.35±0.95	0.10	0.42	0.13±0.06	0.61±0.25
5	1.0	162.0±11.0	3.48±0.08	25.0±10.0	2.10±0.85	0.10	0.42	0.14±0.06	0.57±0.25
ISO	1.5	183.0±7.0	3.64±0.09	26.0±10.0	3.55±1.40	0.09	0.61	0.13±0.06	0.91±0.40
10	1.5	173.0±10.0	3.60±0.07	26.0±10.0	3.55±1.40	0.09	0.60	0.13±0.06	0.91±0.40
5	1.5	150.0±10.0	3.33±0.06	22.0±9.0	2.80±1.10	0.10	0.60	0.13±0.06	0.78±0.30
ISO	2.0	183.0±7.0	3.70±0.08	27.0±11.0	6.15±2.45	0.09	1.00	0.13±0.06	1.54±0.65
10	2.0	157.0±10.0	3.40±0.10	23.0±9.0	4.95±1.95	0.10	0.99	0.13±0.06	1.35±0.55
5	2.0	139.0±8.0	3.17±0.06	20.0±8.0	3.70±1.45	0.14	0.98	0.11±0.05	1.07±0.45

Table 3.7

King-Michie - V Band Derived Parameters

r_a (r_s)	x	L_{V0} ($L_{V\odot}\,pc^{-3}$)	L_V ($10^5\,L_{V\odot}$)	ρ_0 ($M_\odot\,pc^{-3}$)	M ($10^5\,M_\odot$)	Population $(M/L_V)_0$ $(M/L_V)_\odot$	Population (M/L_V) $(M/L_V)_\odot$	Dynamical $(M/L_V)_0$ $(M/L_V)_\odot$	Dynamical (M/L_V) $(M/L_V)_\odot$
ISO	0.0	222.0±14.0	3.07±0.09	48.0±20.0	0.65±0.25		0.20	0.20±0.08	0.20±0.08
10	0.0	222.0±14.0	3.08±0.09	48.0±20.0	0.65±0.25		0.20	0.20±0.08	0.20±0.08
5	0.0	213.0±14.0	3.10±0.14	46.0±20.0	0.65±0.25		0.20	0.20±0.08	0.20±0.08
ISO	0.5	200.0±11.0	3.13±0.14	30.0±12.0	1.10±0.45	0.18	0.40	0.12±0.06	0.32±0.14
10	0.5	198.0±11.0	3.14±0.14	30.0±12.0	1.10±0.45	0.18	0.40	0.12±0.06	0.30±0.14
5	0.5	202.0±12.0	3.41±0.14	30.0±12.0	1.30±0.50	0.16	0.40	0.12±0.06	0.35±0.14
ISO	1.0	198.0±11.0	3.16±0.14	30.0±12.0	1.30±0.50	0.15	0.40	0.13±0.06	0.37±0.14
10	1.0	195.0±11.0	3.16±0.16	30.0±12.0	1.30±0.50	0.14	0.41	0.13±0.06	0.37±0.14
5	1.0	197.0±13.0	3.38±0.12	30.0±12.0	1.60±0.50	0.16	0.41	0.13±0.06	0.42±0.19
ISO	1.0	192.0±11.0	3.19±0.14	26.0±10.0	1.70±0.70	0.13	0.50	0.12±0.05	0.48±0.19
10	1.0	203.0±11.0	3.39±0.17	30.0±12.0	2.15±0.85	0.14	0.51	0.13±0.06	0.56±0.24
5	1.0	183.0±14.0	3.34±0.11	27.0±11.0	2.05±0.85	0.13	0.41	0.13±0.06	0.55±0.24
ISO	1.5	198.0±10.0	3.37±0.14	27.0±11.0	3.05±1.20	0.11	0.75	0.12±0.05	0.80±0.31
10	1.5	198.0±11.0	3.39±0.14	27.0±11.0	3.20±1.25	0.11	0.74	0.12±0.05	0.83±0.31
5	1.5	170.0±13.0	3.22±0.09	25.0±10.0	2.70±1.10	0.12	0.74	0.13±0.06	0.75±0.28
ISO	2.0	202.0± 9.0	3.48±0.14	28.0±11.0	5.40±2.15	0.11	1.19	0.12±0.05	1.38±0.57
10	2.0	181.0±11.0	3.29±0.10	25.0±10.0	4.55±1.80	0.12	1.20	0.12±0.05	1.24±0.47
5	2.0	160.0±10.0	3.08±0.09	22.0± 9.0	3.50±1.40	0.14	1.22	0.12±0.05	1.02±0.43

cluster luminosity varies by only 10% for the various models. Hence the composition (and therefore the M/L) of the cluster core is largely independent of the mass function slope. As we shall see when we discuss the KM kinematic modeling in §3.5.1 the dynamical M/L's exhibit similar behavior.

3.3   RADIAL VELOCITIES

Spectra of 36 red giants were obtained during 1991 January 18-20 using the 4m at Cerro Tololo Inter-American Observatory (CTIO) and during January 30 -February 1 and February 14-20 at the 2.5m at LCO. Echelle spectrographs with 2D-Frutti detectors were employed at both telescopes.

The observation and reduction procedures for a previous run at LCO have been discussed extensively in Welch *et al.* 1991 and remain largely unchanged for this data. The CTIO data were obtained and reduced in a similar manner. Unfortunately, due to technical problems involving the dither on the CTIO 2D-Frutti, only half the available observing time was productive. Furthermore, the spectral resolution was about 50% lower than the LCO spectrograph, resulting in velocities with uncertainties about 50% larger. The observing procedure consisted of exposures with integration times of 500 - 1500s and Th-Ar arcs approximately every 45 minutes. A representative LCO spectrum is shown in Fig. 2 of Côté *et al.* (1991). The reduction utilizes the IRAF ECHELLE and RV packages (Tody 1986) to obtain both velocities and velocity uncertainties. The velocity zero-point is tied to the IAU velocity standard 33 Sex as described in Fischer *et al.* 1992a and is believed to be accurate to better than 1 km s^{-1}.

The radial velocity data are presented in Table 3.8. Column 1 contains the stellar identifications, column 2 indicates the observatory, column 3 has the projected radius, column 4 the equinox J2000.0 position angle, column 5 contains the

radial velocities and column 6 contains the mean velocity for stars with repeated measurements. Column 7 is the Heliocentric Julian Date – 2448000 for the velocity measurements. Columns 8 and 9 are V and B–V for the stars. The velocity uncertainties returned by the RV package seem to agree fairly well with the observed scatter in stars with repeated measurements. Ten stars have been measured at least twice (a total of 24 spectra), yielding $\chi^2 = 13.2$ for 14 degrees of freedom. Closer examination of Table 3.8 reveals that Star 13 has two measurements which are significantly discrepant. Further, the higher precision velocity is more than 5 km s^{-1} larger than any other cluster star. The radial velocity implies that this star is in the LMC and, therefore, definitely a giant. The large velocity change over about 24 hours argues against the star being a binary and further observations are required to determine its true nature. Alternatively, it might simply be a case of measurement error. Regardless, we choose not to include it in the following analysis. Removing Star 13 reduces χ^2 to 6.5 for 13 degrees of freedom. This rather low value of χ^2 is a strong indication that we have not underestimated the velocity uncertainties and that there are no significant zero-point differences between spectra taken on different nights or on different telescopes. Fig. 3.4 is a finder chart for stars 1 through 36, while Fig. 3.5 shows the positions of the stars relative to the cluster center along with a line indicating the photometric minor axis.

Fig. 3.6 shows mean radial velocity vs. projected radius (upper panel) and versus position angle (lower panel). The solid line is the mean velocity (§3.5.1), $\bar{v} = 293.3 \pm 1.0$ km s^{-1}, which is consistent with the two lower precision velocities obtained by Olzsewski *et al.* (1991) of 292.0 km s^{-1}, indicating no serious zero-point problems. There are no obvious trends present in the data such as one might expect. Typically, cluster velocity data will exhibit a decreasing velocity dispersion

Table 3.8
Radial Velocities

ID	Telescope	R (pc)	Θ (°)	v_r (km s^{-1})	$\langle v_r \rangle$ (km s^{-1})	HJD (−2448000)	V (mag)	B-V (mag)
1	CTIO	1.4	346.7	295.0 ± 2.1	294.9 ± 1.8	276.7601	16.88	0.82
	CTIO			294.6 ± 3.3		275.7578		
2	CTIO	1.5	273.3	296.4 ± 2.1	294.8 ± 1.0	276.7251	15.94	1.36
	LCO			294.6 ± 1.2		287.5633		
	CTIO			293.3 ± 2.2		275.7289		
3	CTIO	2.2	119.1	292.4 ± 2.0	292.8 ± 1.5	277.5507	15.89	1.38
	CTIO			293.4 ± 2.5		275.8156		
4	LCO	2.2	316.6	294.8 ± 1.5	294.2 ± 1.2	288.5598	16.31	1.26
	CTIO			293.0 ± 2.5		276.7102		
	CTIO			293.5 ± 2.9		275.7175		
5	CTIO	2.4	353.7	291.0 ± 2.9	292.8 ± 1.6	275.7691	16.09	1.01
	CTIO			293.6 ± 1.9		276.7798		
6	LCO	2.5	89.0	291.4 ± 1.3	291.4 ± 1.3	287.6484	16.35	1.08
7	CTIO	3.0	139.4	291.4 ± 1.7	291.2 ± 1.4	277.5654	16.48	1.44
	CTIO			290.8 ± 2.4		275.8273		
8	CTIO	3.4	44.4	293.4 ± 3.3	296.3 ± 2.2	275.7979	16.92	1.03
	CTIO			298.6 ± 2.9		277.7268		
9	CTIO	3.5	284.0	291.4 ± 2.2	291.4 ± 2.2	277.6689	16.35	1.54
10	CTIO	3.6	358.1	293.6 ± 1.9	293.6 ± 1.9	277.7086	16.57	1.01
11	LCO	3.9	327.2	296.7 ± 1.0	296.7 ± 1.0	287.5977	17.09	1.39
12	LCO	4.0	4.2	292.9 ± 1.4	292.9 ± 1.4	287.6338	16.57	1.01
13	CTIO	4.1	36.7	304.3 ± 2.6	Not Used	276.7952	16.11	1.52
	CTIO			292.7 ± 3.6		275.7854		
14	CTIO	4.3	16.1	290.7 ± 2.1	290.7 ± 2.1	277.6874	16.59	1.46
15	LCO	4.3	234.7	295.2 ± 1.5	295.2 ± 1.5	287.5769	16.75	1.25
16	CTIO	4.3	340.1	296.2 ± 2.8	291.9 ± 0.9	275.7405	16.02	1.38
	LCO			291.3 ± 1.1		302.5609		
	CTIO			291.4 ± 2.0		276.7448		
17	LCO	4.6	120.1	295.5 ± 2.1	295.5 ± 2.1	289.6231	16.98	1.10
18	CTIO	5.0	308.3	294.2 ± 3.4	294.2 ± 3.4	277.6038	16.70	1.42
19	LCO	5.0	104.0	292.6 ± 1.5	292.6 ± 1.5	289.6057	16.90	1.04
20	LCO	5.2	172.1	292.8 ± 0.9	292.8 ± 0.9	289.5814	16.96	1.27
21	CTIO	5.3	346.8	297.5 ± 2.6	297.5 ± 2.6	277.7824	16.76	1.25
22	CTIO	5.4	163.2	294.4 ± 1.8	294.4 ± 1.8	277.8052	16.70	1.34
23	LCO	5.6	21.7	291.8 ± 1.6	291.8 ± 1.6	287.6130	16.64	1.31
24	CTIO	5.6	70.3	291.8 ± 1.7	291.8 ± 1.7	277.5862	16.31	1.11
25	LCO	8.1	67.5	291.1 ± 1.6	291.1 ± 1.6	288.6356	16.87	1.51
26	CTIO	8.4	325.4	291.3 ± 2.9	291.3 ± 2.9	277.6291	17.02	1.52

Table 3.8 (cont.)
Radial Velocities

ID	Telescope	R (pc)	Θ (°)	v_r (km s^{-1})	$\langle v_r \rangle$ (km s^{-1})	HJD (-2448000)	V (mag)	B-V (mag)
27	LCO	8.9	142.4	290.6 ± 0.9	290.6 ± 0.9	288.6536	16.35	1.60
28	LCO	9.1	2.8	290.1 ± 1.3	290.1 ± 1.3	288.5932	16.91	1.41
29	LCO	9.5	40.8	296.6 ± 1.3	296.6 ± 1.3	288.6113	16.90	1.64
30	LCO	11.1	11.3	297.3 ± 0.9	297.4 ± 0.7	288.5716	15.79	1.89
	LCO			297.6 ± 1.0		287.6762		
	CTIO			296.7 ± 3.2		275.8437		
31	LCO	12.1	133.7	295.3 ± 1.0	295.3 ± 1.0	289.5633	16.56	1.77
32	LCO	12.5	86.6	295.7 ± 1.2	295.7 ± 1.2	289.6661	16.82	1.56
33	LCO	12.7	285.1	291.9 ± 1.4	291.9 ± 1.4	289.6897	16.68	1.74
34	LCO	12.7	116.2	290.3 ± 1.3	290.3 ± 1.3	289.6481	16.89	1.22
35	LCO	14.0	325.4	287.5 ± 1.9	287.5 ± 1.9	289.7078	16.84	2.10
36	LCO	19.9	155.8	294.0 ± 1.4	294.0 ± 1.4	302.6129	16.66	1.80

with increasing projected radius and, if rotation is present and the cluster inclination favorable, a sinusoidal functional dependence on position angle (Fischer *et al.* 1992a). The reason we do not observe either of these phenomena may simply be due to the sparseness of the data and the large values of the velocity uncertainties relative to both the velocity dispersion and the rotation amplitude.

3.4   EVOLUTIONARY TIMESCALES

Implicit in the adoption of "mass segregation" models is the assumption that there has been sufficient time for energy exchange between different mass classes to occur. Two important relaxation timescales based on energy exchange through distant two-body encounters are the central relaxation time

$$t_{r0} = (1.55 \times 10^7 \text{yr}) \left(\frac{r_s}{\text{pc}}\right)^2 \left(\frac{v_s}{\text{km s}^{-1}}\right) \left(\frac{M_\odot}{\langle m \rangle}\right) [\log(0.5M/\langle m \rangle)]^{-1} \qquad (3.4)$$

$$= 2.9 - 7.9 \times 10^8 \text{yr},$$

(Lightman and Shapiro 1978) and the half mass relaxation time

$$t_{rh} = (8.92 \times 10^8 \text{yr}) \left(\frac{M}{10^6 M_\odot}\right)^{1/2} \left(\frac{r_h}{\text{pc}}\right)^{3/2} \left(\frac{M_\odot}{\langle m \rangle}\right) [\log(0.4M/\langle m \rangle)]^{-1} \qquad (3.5)$$
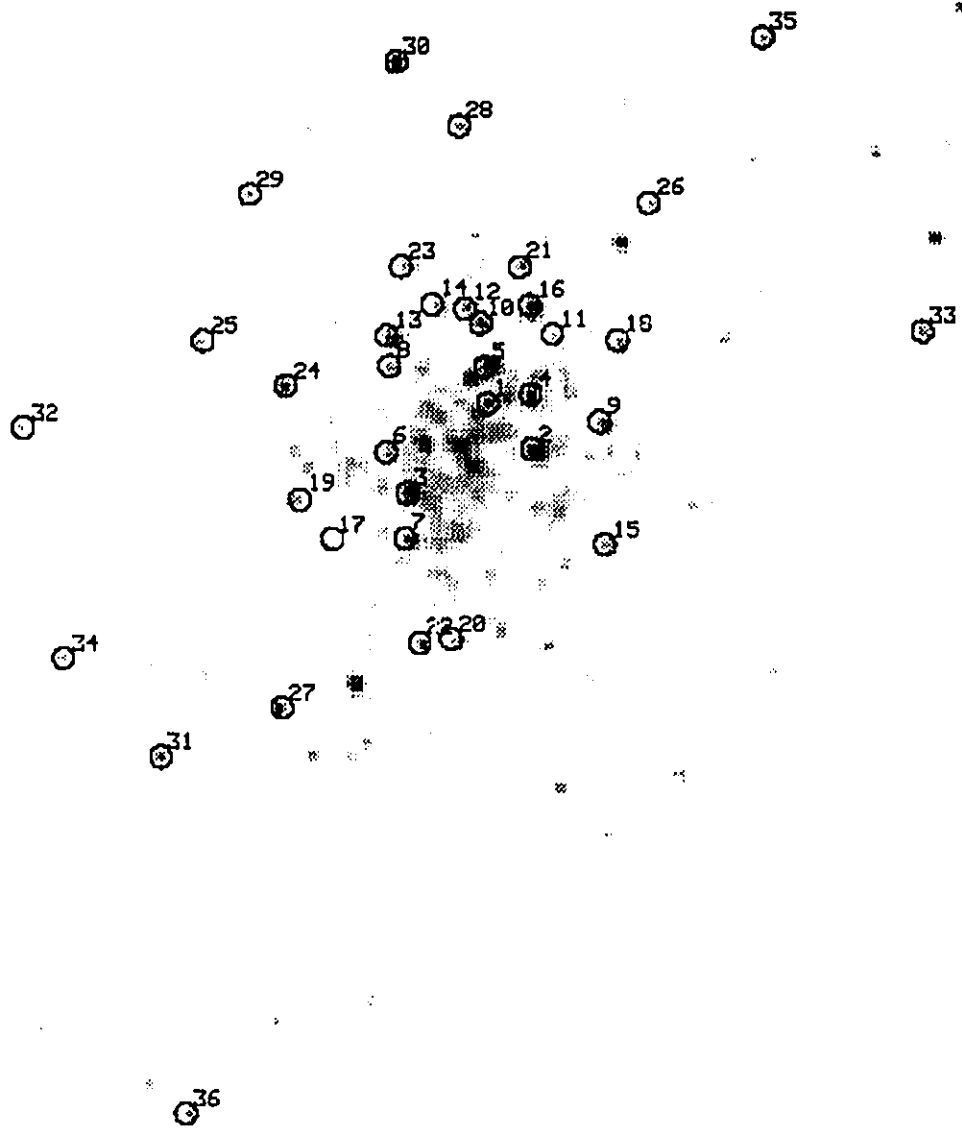
Fig. 3.4 A finder chart for stars with measured radial velocities. North is at the top, and east is to the left.
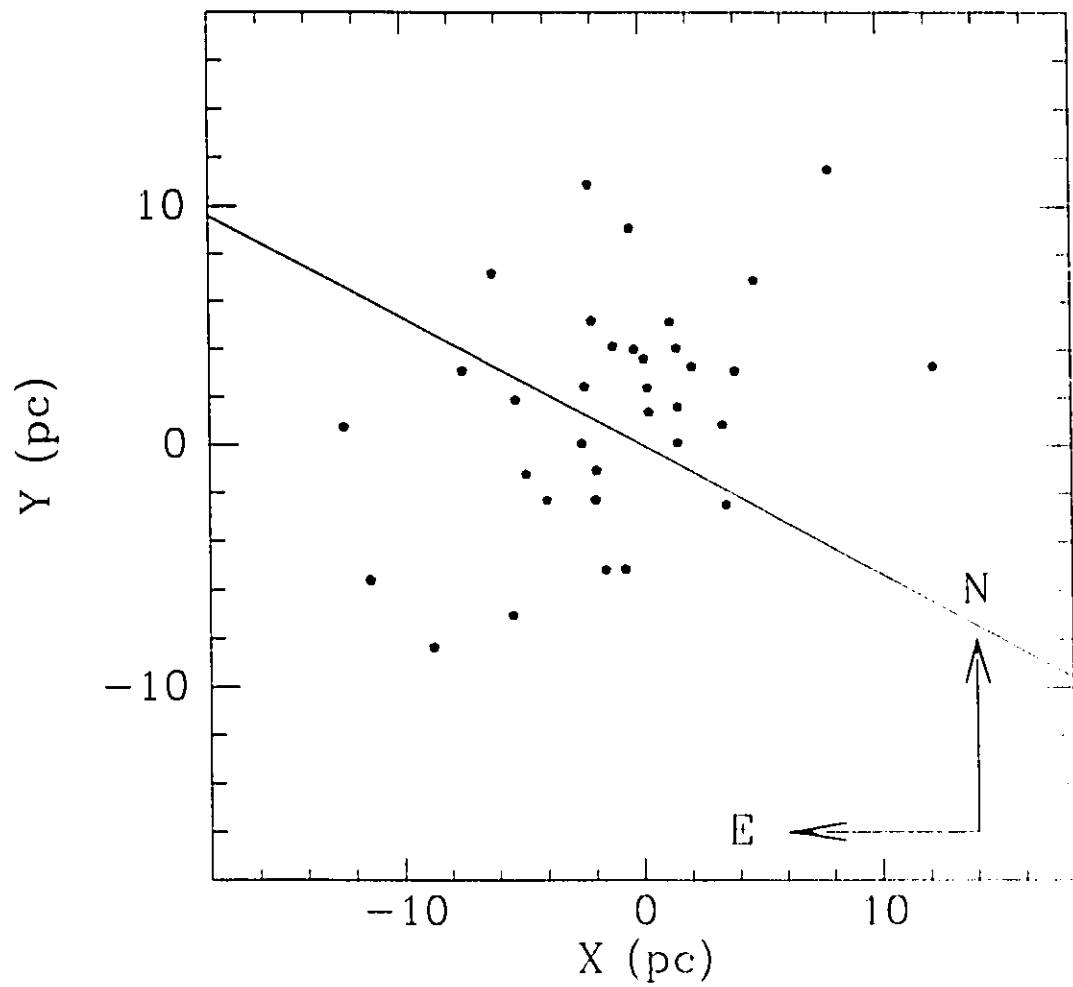
Fig. 3.5 - Positions with respect to the cluster center for stars with measured radial velocities. The straight line is the photometric minor axis.
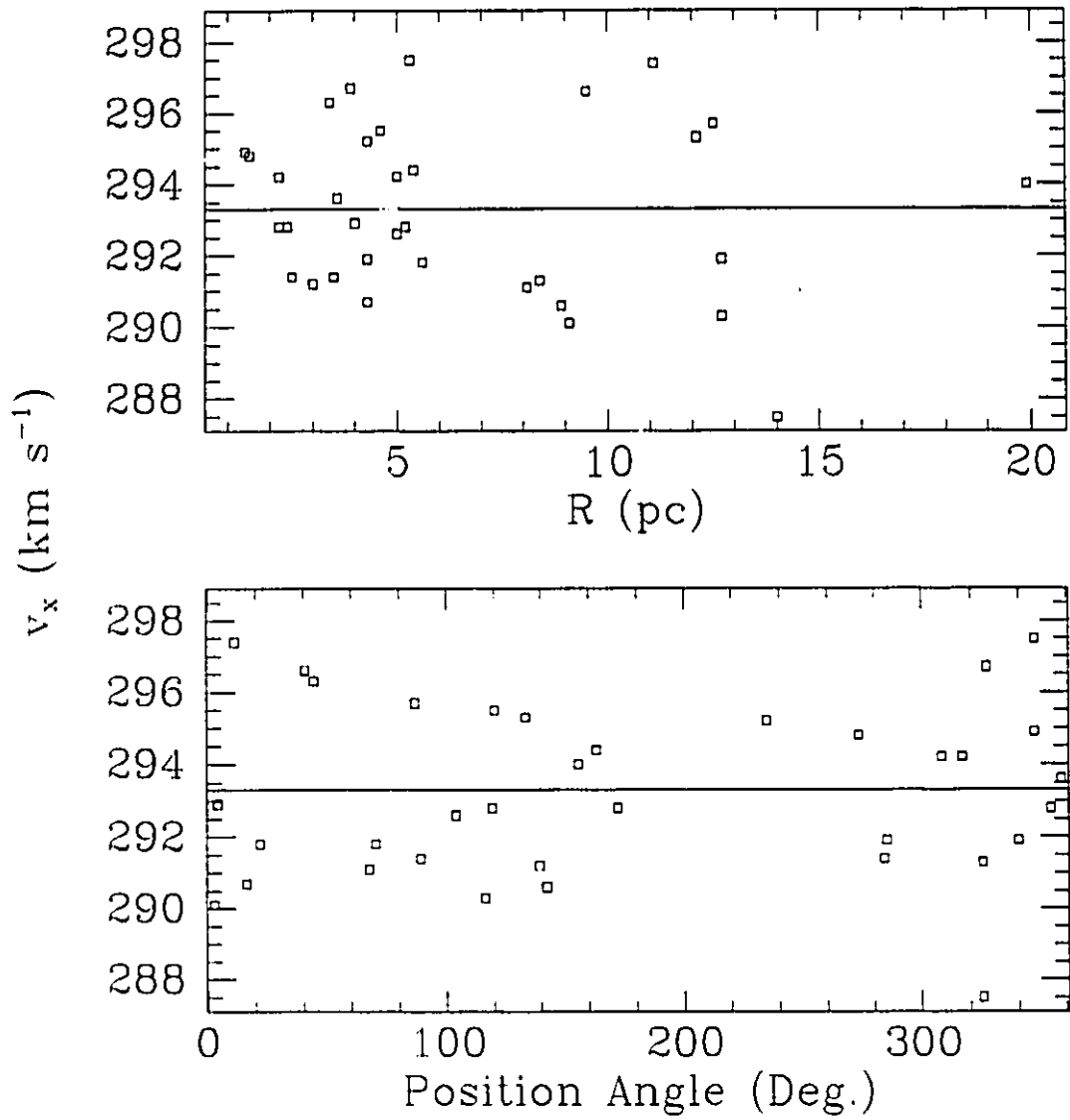
Fig. 3.6 - Plot of observed radial velocity versus position angle (lower panel) and projected radius (upper panel). The solid lines indicate the cluster mean velocity.

$$= 6.0 - 16.0 \times 10^9 \text{yr},$$

(Spitzer and Hart 1971), where the numerical values are for mass functions slopes ranging from $0.0 \leq x \leq 2.0$. As was mentioned earlier, the best age estimate for NGC 1978 is 2×10^9 yrs which is several times greater than the central relaxation time, but significantly younger than the half-mass relaxation time. We conclude, therefore, that there are significant portions of the cluster which have not had sufficient time to relax and it is important to keep this in mind when interpreting the results of the KM model analysis.

3.5   MASS DETERMINATIONS

3.5.1   King-Michie Models

The mass of a multi-mass KM model is given by

$$M = \frac{9 r_s v_s^2}{4\pi G} \int \frac{\rho}{\rho_0} r^2 dr \tag{3.6}$$

Illingworth (1976), where r_s is given in Tables 4 and 5, and v_s is the scale velocity. The run of $\sigma_{r,i}^2(r)$ and $\sigma_{t,i}^2(r)$ are determined from

$$\sigma_{(r,t),i}^2(r) = \frac{\int_{|\sigma_i| \leq W(r)} f_i(\sigma_i, W) \sigma_{\sim}^2 d^3 \vec{\sigma}_i}{\int_{|\sigma_i| \leq W(r)} f_i(\sigma_i, W) d^3 \vec{\sigma}_i}, \tag{3.7}$$

where W is the reduced potential ($W = 0$ at the tidal radius), $\sigma_k = \sigma_i \cos\theta$ or $\sigma_i \sin\theta$ for $\sigma_{r,i}$ or $\sigma_{t,i}$, respectively, and the i subscript refers to the ith mass class. Comparisons were made between the observed velocities and scaled model velocity dispersions projected along the line of sight,

$$\sigma_{p,i}^2(R) = \frac{2}{\mu_i(R)} \int_R^\infty \frac{\rho_i(r)[(r^2 - R^2)\sigma_{r,i}^2(r) + R^2 \sigma_{t,i}^2(r)] dr}{r(r^2 - R^2)^{1/2}}, \tag{3.8}$$

(Binney and Tremaine 1987, p. 208), where μ_i is the surface density of the ith mass class. The optimal scaling was derived using the maximum likelihood technique

outlined in Gunn and Griffin (1979). Simply put, the probability density function for $v_{x,k}$, an observed stellar velocity, is a Gaussian with standard deviation equal to the model dispersion added in quadrature to the velocity uncertainty:

$$P_k \sim \frac{1}{\sqrt{\sigma^2_{err,k} + v^2_s \sigma_{p,k,i}}} e^{-(v_{x,k}-\overline{V})^2/2(v^2_s\sigma^2_{p,k,i}+\sigma^2_{err,k})}. \tag{3.9}$$

This function is minimized with respect to v_s and $\overline{V}$ resulting in two equations which can be solved simultaneously for the most probable values of the two parameters.

The values of v_s thus obtained are displayed in column 8 of Tables 4 and 5. The corresponding dynamical masses and M/L's are in columns 9 and 10, respectively of Tables 6 and 7. Monte-Carlo orbit simulations were used to determine the uncertainties in the fitted and derived parameters and to search for possible systematic effects. We started with the known projected radii (R_k) of the program stars. The true radii are in the range $R_k \leq r \leq r_t$. If x is the displacement from the mean cluster position along the line-of-sight such that $r = \sqrt{R_k^2 + x^2}$, then the probability that a star is at x is $p(x)$, where

$$p(x) \sim \rho_i(\sqrt{R_k^2 + x^2}). \tag{3.10}$$

Three-dimensional positions, along with corresponding model-dependent radial and tangential velocities were drawn at random from their respective probability distributions. The velocity component along the line-of-sight was then determined, and an error term, drawn from a Gaussian distribution with standard deviation equal to the velocity uncertainty, as tabulated in Table 3.8, was added. This process was repeated, producing 10000 sets of data each with a given mass, r_a, x and the same projected positions and velocity measurement errors as the original data set. Finally the maximum likelihood technique was applied to each of the artificial data sets and the results compared to the input values for the models. From this we

noticed that the maximum likelihood method resulted in scale velocities that were biased systematically too low by approximately 4% (the values for v_s in Tables 4 and 5 have already been corrected for this effect).

A goodness-of-fit statistic

$$\zeta^2 = \sum \frac{(v_{x,k} - \overline{v})^2}{(v_s^2 \sigma_{p,k}^2 + v_{err,k}^2)} \tag{3.11}$$

was generated for each model and is shown in column 9 of Tables 4 and 5 (33 degrees of freedom). The distribution of this statistic can be extracted from the Monte Carlo simulations and column 10 shows the probability of exceeding the observed ζ^2 assuming that the cluster velocities are specified by the model parameters indicated and have the uncertainties tabulated in Table 3.8. The greater this probability the higher the likelihood that the cluster velocities are drawn from the specified distribution.

The results of the KM kinematic modeling can be summarized as follows: 1) The results for the two different bandpasses are consistent. 2) As can be seen from the $P(> \zeta^2)$, the radial velocity data are too sparse to provide a means of discriminating between the different sets of dynamical parameters with any confidence. However, the multi-mass models are in marginally better agreement with the kinematic data than the single-mass models. 3) A similar trend is seen in the dynamical M/L's as was seen for the population M/L's: the global M/L is very poorly determined while the central M/L is much more tightly constrained. As x is increased, the number of low-mass stars at large radii is increased. The resultant change in the gravitational potential at points where we have measured stellar velocities is minor, and therefore there is very little change in v_s. As was mentioned in §3.2.1, there is also very little change in the central luminosity density and, therefore, a relatively model-independent central M/L. 4) The best agreement

between population and dynamical M/L's is seen for the cases $x = 0.0$ for the B band $[(M/L)_0 = 0.14 \pm 0.06 \, M_\odot/L_{B\odot}$ and $M/L = 0.34 \pm 0.15 \, M_\odot/L_{B\odot}]$ and $x = 0.5$ for the V $[(M/L)_0 = 0.13 \pm 0.06 \, M_\odot/L_{V\odot}$ and $M/L = 0.40 \pm 0.15 \, M_\odot/L_{V\odot}]$, independent of r_a. However, there is agreement at fairly high confidence levels for all values of x. 5) Because the velocity uncertainties are about 70% of the derived velocity dispersion, the cluster mass estimates are somewhat dependent upon the accuracy of these uncertainties. As discussed earlier, the χ^2 for the 10 stars with multiple measurements came out lower than average indicating that the uncertainties are probably not underestimated. If, however, they are overestimated then one would get an underestimate for both the velocity dispersion and the mass. The worst possible (not to mention unreasonable) case is that the uncertainties are actually zero. In this case, we get a slightly less than 30% increase in the velocity dispersion and about a 60% increase in the cluster mass and M/L.

3.5.2   Oblate Spheroids

In order to determine the cause of flattening we have decided to model NGC 1978 as both a rotating and non-rotating (i.e. anisotropically supported) oblate spheroid. Because of the sparseness of the kinematic data, the goal will be to construct models with *extreme* sets of parameters and see which provide the greatest consistency with the data. This will also yield a mass range for the cluster.

For an axisymmetric system, the relevant Jeans' equations (velocity moments of the collisionless Boltzmann equation) in cylindrical coordinates are:

$$\frac{\partial(\rho\sigma_R^2)}{\partial R} + \frac{\partial(\rho\sigma_{Rz})}{\partial z} + \rho\left(\frac{\sigma_R^2 - \sigma_\phi^2 - v_\phi^2}{R}\right) + \rho\frac{\partial\Phi}{\partial R} = 0, \qquad (3.12)$$

and

$$\frac{\partial(\rho\sigma_{Rz})}{\partial R} + \frac{\partial(\rho\sigma_z^2)}{\partial z} + \frac{\rho\sigma_{Rz}}{R} + \rho\frac{\partial\Phi}{\partial z} = 0. \qquad (3.13)$$

where (R,ϕ,z) are the cylindrical coordinate axes, the $(\sigma_R,\sigma_\phi,\sigma_z)$ are the corresponding velocity dispersions, and v_ϕ is the rotation velocity. Φ is the gravitational potential.

Both the rotating and non-rotating models which were used have velocity ellipsoids aligned with the cylindrical coordinate axes (i.e. $\sigma_{Rz} = 0$) and, as well, both have

$$\sigma_\phi = \frac{\sigma_R}{\sqrt{1 + (R/R_a)^2}}, \tag{3.14}$$

where R_a is varied from 5 pc to ∞. The rotating models also have the condition

$$\sigma_R = \sigma_z, \tag{3.15}$$

im⁻ ʰ⁻ing

$$v_\phi^2 = R\frac{\partial\Phi}{\partial R} + \frac{R}{\rho}\frac{\partial}{\partial R}\int_z^\infty \rho\frac{\partial\Phi}{\partial z}dz + \frac{1}{\rho}\left[1 - \frac{1}{\sqrt{1+(R/R_a)^2}}\right]\int_z^\infty \rho\frac{\partial\Phi}{\partial z}dz. \tag{3.16}$$

The models are constructed by assuming that the mass distribution is equivalent to the deprojected light distribution (constant M/L). Equations 3.13 and 3.16 can then be solved directly to obtain σ_z, and v_ϕ. Once v_ϕ is known it can be substituted into equation 3.12 which, in turn, can be solved for σ_R and σ_ϕ. This is outlined in Binney and Tremaine (1987) for the $\sigma_R = \sigma_\phi = \sigma_z$ case.

Fig. 3.7 shows isovelocity maps for the models with $R_a = \infty$. The top panel is σ_R for the rotating model and the middle panel is the corresponding v_ϕ. The bottom panel is σ_R for the non-rotating model. Unfortunately, it is impossible to determine the inclination of NGC 1978 so we assume that it is $90°$. We believe this to be reasonable as it is already among the most elliptical clusters known and, of course, if it is inclined then it is intrinsically even more elliptical.

Once the models have been generated, it is simply a matter of scaling them using a similar maximum likelihood method to that employed for the KM models.
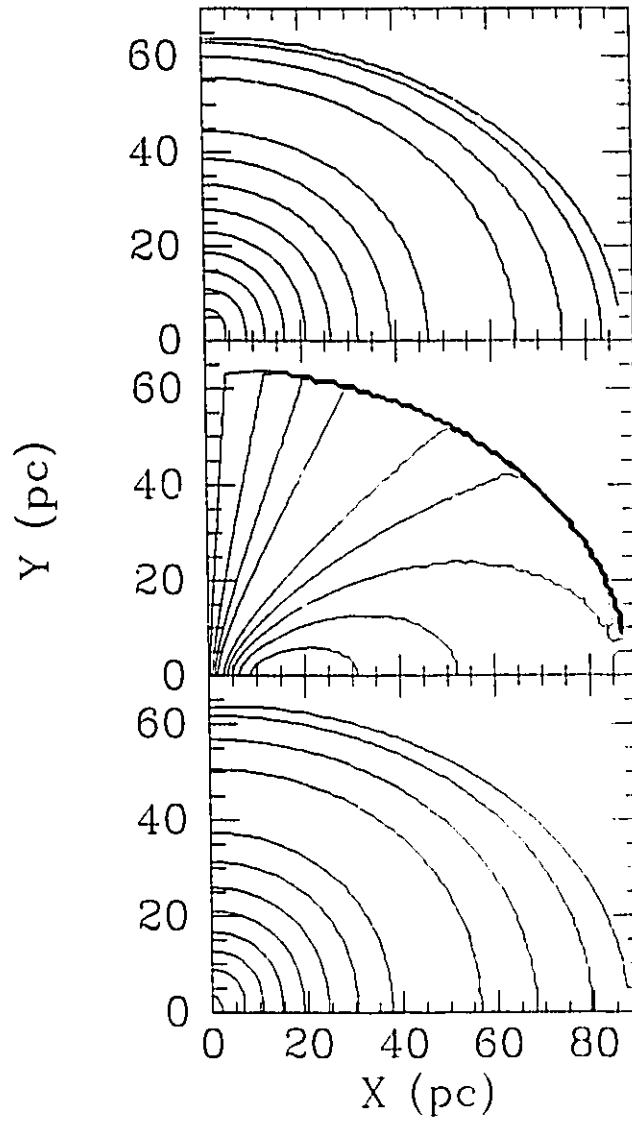
Fig. 3.7 - Isovelocity maps for oblate spheroid models. The top panel is σ_R for the rotating model and the middle panel is the corresponding v_ϕ. The bottom panel is σ_R for the non-rotating model.

Table 3.9 shows the results of this exercise; column 1 is R_a, while columns 2, 3, 4 and

5 are, respectively, the total mass, the goodness-of-fit parameter ζ^2, the probability

of exceeding it (as described in §3.5.1) and the cluster M/L_V for the non-rotating

case. Similarly, columns 6, 7, 8, and 9 represent the rotating case.

Table 3.9
Oblate Spheroid Models

R_a (pc)	Non-Rotating				Rotating			
	M_∞ $(10^4 M_\odot)$	ζ^2	$P(\zeta^2)$	M/L_V $(M_\odot/L_\odot)$	M_∞ $(10^4 M_\odot)$	ζ^2	$P(\zeta^2)$	M/L_V $(M_\odot/L_\odot)$
∞	6.5 ± 2.5	33.75	0.72	0.20 ± 0.08	7.6 ± 2.5	39.14	0.23	0.23 ± 0.09
100	6.5 ± 2.5	33.76	0.71	0.20 ± 0.08	7.6 ± 2.5	39.28	0.23	0.23 ± 0.09
50	6.5 ± 2.5	33.82	0.71	0.20 ± 0.08	7.8 ± 2.5	39.69	0.22	0.24 ± 0.09
25	6.5 ± 2.5	34.07	0.66	0.20 ± 0.08	7.9 ± 3.0	41.14	0.18	0.24 ± 0.09
10	6.6 ± 2.5	35.41	0.44	0.20 ± 0.08	9.0 ± 3.0	48.04	0.09	0.27 ± 0.10
5	7.1 ± 2.5	36.98	0.30	0.22 ± 0.09	9.8 ± 3.5	59.18	0.03	0.29 ± 0.10

There are four points worth noting: 1) The distribution of ζ^2 is much broader

for the rotating models. Fig. 3.8 shows histograms of ζ^2 based on sets of 10000

Monte Carlo simulations for two $R_a = \infty$ models. The solid line is the non-rotating

model while the dashed line is the rotating model. It is because of this broader

distribution that we cannot completely reject the rotating models. 2) The rotating

models produce higher masses than the non-rotating models, opposite to what is

seen in NGC 1866 (Fischer et al. 1992a), a cluster which has rotation detected at

the 97% confidence level. In fact, higher masses should result from the application

of a rotating model to a non-rotating system since the removal of a non-existent

rotation field causes an increase in the apparent velocity dispersion. 3) The oblate

spheroid masses are consistent with the spherical single-mass KM model masses

derived in §3.5.1. Even with $\epsilon \approx 0.3$ a spherical approximation is excellent. 4) The

non-rotating (anisotropic velocity dispersion) models appear to represent a better

fit to the data, although it is impossible to exclude the rotating models, especially

those with higher values of R_a. This trend to higher $P(> \zeta^2)$ with increasing R_a is seen in the non-rotating case as well. The precision and size of our radial velocity data set is insufficient to strongly constrain the flattening mechanism.

There is very little evidence to support the hypothesis of a recent cluster-cluster merger. The cluster light distribution is very smooth, the isophotes agree well with ellipses with no evidence for subclustering, and there is no sign of tidal interaction. Furthermore, except in very restricted cases, a recent merger would tend to give the cluster a net rotation for which there is no strong indication.

Because these are single mass models (i.e. the mass scales as the luminosity) they do not explicitly yield information about the mass function. However, it is possible to test which mass function is consistent with the dynamical M/L_V. We maintain the same assumptions about the form of the mass function (i.e. a power-law with a flattening at 0.3 $M_\odot$), the mass-luminosity relationship and the mass of the stellar remnants that were used for the KM modeling.

The population M/L_V is given by equation 3.3. We conclude that it is very difficult to reconcile the low M/L_V's with the adopted form of the mass function without invoking a high low-mass cut-off. With the KM low-mass cut-off (0.15 $M_\odot$), the lowest population M/L_V that can be achieved is $M/L_V = 0.40\ M_\odot/L_{V\odot}$ at $x \approx 0.2$. It is necessary to raise the low-mass cut-off to 0.8 $M_\odot$ (with $x = 1.6$) in order to get a population M/L_V of about 0.2 $M_\odot/L_{V\odot}$. This seems unreasonably high for a low-mass cut-off and leads us to believe that either our adopted mass function is an oversimplification or the assumption that mass follows light is unreasonable. Certainly, we see from the multi-mass KM models that it is possible to get excellent agreement between population and dynamical M/L_V's supporting the latter supposition.
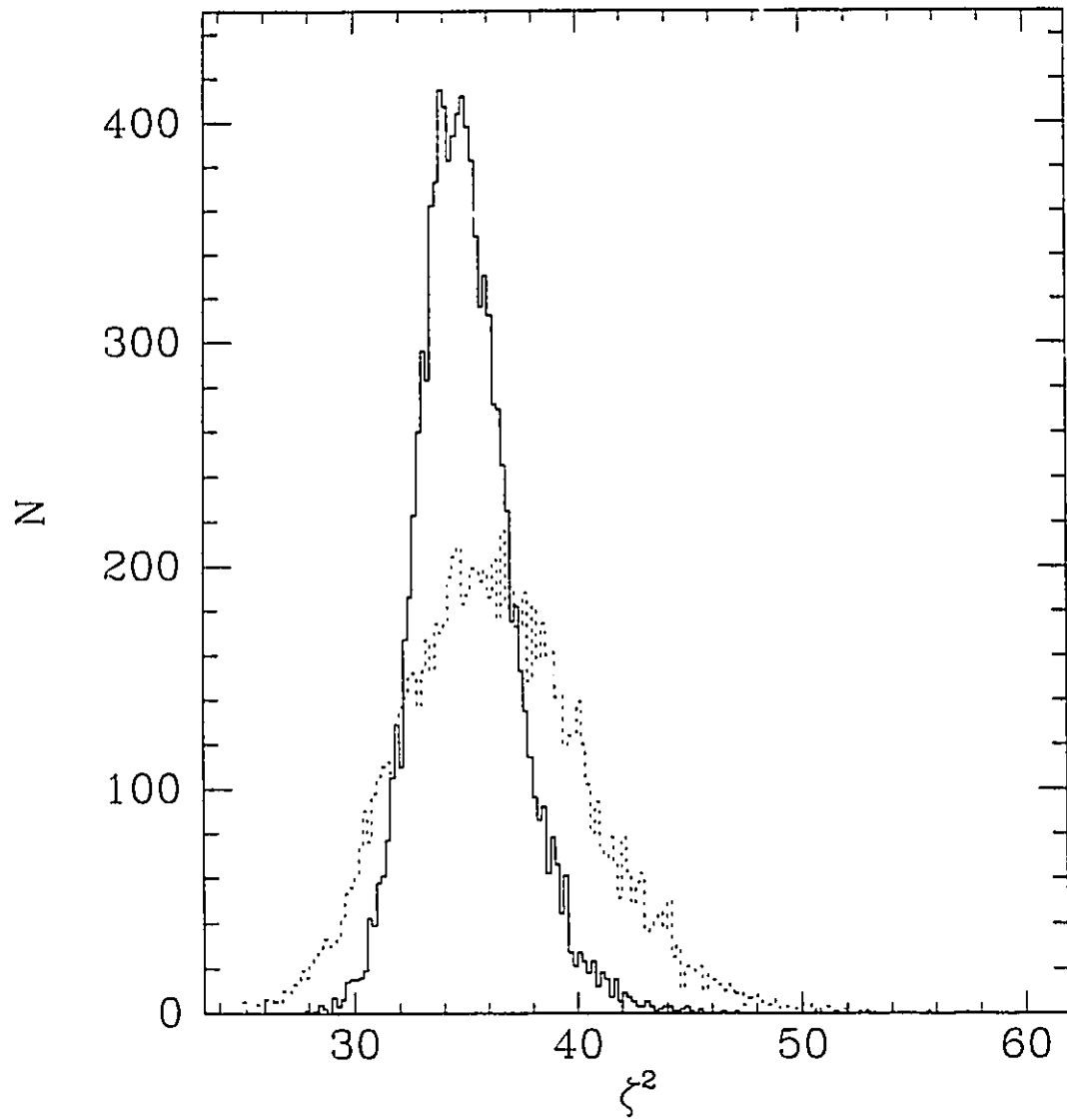
Fig. 3.8 - Histograms of ζ^2 based on sets of 10000 Monte Carlo simulations for two $R_a = \infty$ oblate spheroid models. The solid line is the non-rotating model while the dashed line is the rotating model.

3.7

3.6   COMPARISON WITH PREVIOUS RESULTS

There have been two previous kinematic studies of NGC 1978, and we consider these in turn. Meylan *et al.* (1991) find a central velocity dispersion of 5.8 ±1.2 km s^{-1} based upon an integrated spectrum of the cluster center (they use a region that does not overlap with our radial velocity data set). Seitzer (1991) finds a dispersion of 3.7 ± 0.8 km s^{-1} based upon 8 stellar velocities within two core radii of the cluster center. Seitzer further claims that the central velocity dispersion is a model-dependent 10 - 40% higher than this number. Our central velocity dispersion is also model-dependent and is about $\sigma_0 = 2.2\pm 0.5$ km s^{-1}.

Our result disagrees with Meylan *et al.* at the 2.8σ level and, even if we assume that our radial velocity uncertainties are zero, we get an upper limit of $\sigma_0 = 2.8\pm0.6$ km s^{-1}, still more than 2.2σ lower. Perhaps their result is affected by a large rotation velocity at the cluster center, but it is not possible to rule out a central mass density cusp. If so, the surface photometry does not reveal an accompanying luminosity density cusp. The disagreement with Seitzer is at approximately the 2σ level and it is not possible to definitively resolve this discrepancy without knowledge of which stars he measured.

We conclude by stating that when measuring a velocity dispersion the sources of error one encounters, such as binaries, field stars, slit errors, zero-point drift, etc. will tend to bias the result too high. One possible source of error than can cause the opposite effect occurs when two (or more) stars fall in the slit. This will tend to give the mean velocity for the two objects, which will, on average, be lower than the residual velocities of the individual stars. We feel that this has not been a problem with our sample of giants which are relatively isolated and significantly brighter than the underlying cluster light.

3.7 CONCLUSIONS

In this paper we have examined the internal dynamics of the elliptical LMC cluster NGC 1978 using BV CCD images and echelle spectra of 35 giants. Projected radii for the giants range from $1.4 \leq R$ (pc) ≤ 20.0 and the mean estimated stellar velocity uncertainty is $\sigma_{err} \approx 1.6$ km s^{-1}. The mean cluster velocity is $\overline{V} = 293.3 \pm 1.0$ km s^{-1}.

1) BV luminosity profiles were constructed out to projected radii of $R > 100$ pc. Despite the large ellipticity, single and multi-mass King-Michie models with $5.0 \leq r_a$ (r_s) $\leq \infty$ and $0.0 \leq x \leq 2.0$ were applied to the data. The single-mass models provided better agreement with the surface photometry which is perhaps not surprising since NGC 1978 is considerably younger than its half-mass two-body relaxation time. Among multi-mass models, there is (slightly) better agreement seen for the models with shallow mass functions. The total cluster luminosity is model dependent; $L_B = 3.1 - 3.7 \pm 0.2 \times 10^5$ $L_{B\odot}$ and $L_V = 3.0 - 3.5 \pm 0.2 \times 10^5$ $L_{V\odot}$.

2) The single mass KM models yielded $M/L = 0.20 \pm 0.08$ $M_\odot/L_\odot$. For the multi-mass KM models, we found that while the central M/L's were relatively tightly constrained to be around $(M/L)_0 = 0.13 \pm 0.06$ $M_\odot/L_\odot$ the global M/L's ranged over more than a factor of five (i.e., $M/L = 0.3 - 1.5$ $M_\odot/L_\odot$). The best agreement between the population and dynamical M/L's is seen for the cases $x = 0.0$ for the B band [$(M/L_B)_0 = 0.14 \pm 0.06$ $M_\odot/L_{B\odot}$ and $M/L_B = 0.34 \pm 0.15$ $M_\odot/L_{B\odot}$] and $x = 0.5$ for the V [$(M/L)_0 = 0.13 \pm 0.06$ $M_\odot/L_{V\odot}$ and $M/L = 0.40 \pm 0.15$ $M_\odot/L_{V\odot}$], independent of r_a. The kinematic data were too sparse to place strong constraints on dynamical parameters such as the anisotropy radius or the mass function.

3) Non-rotating single-mass oblate spheroid models produced M/L's consistent
   with the single-mass KM models while the rotating models had marginally
   higher M/L's. We found that the non-rotating model was in better agreement
   with the kinematic data but that it was impossible to completely rule out
   the rotating models. As well, there is very little morphological evidence for a
   merger; the light distribution is quite smooth, the isophotes are very elliptical
   (i.e. no subclustering) and there is no sign of tidal interaction.

4) In order to get consistency between the single-mass dynamical M/L and a
   simple power-law mass function requires an unusually high low-mass cut-off.
   A more probable solution invokes the multi-mass models or perhaps a more
   complex form for the mass function.

ACKNOWLEDGEMENTS

DYNAMICS OF THE YOUNG BINARY LMC CLUSTER NGC 1850

CHAPTER 4

4.1 INTRODUCTION

There is a large population of young, massive clusters in the LMC that have
no counterparts in the Milky Way. These objects represent a unique opportunity
to study the internal dynamics of resolved stellar systems in which the current ages
are substantially less than the two-body relaxation timescales. The clusters can
be studied kinematically to determine masses and mass-to-light ratios (hereafter,
M/L's) in order to constrain the initial mass function. Through the use of both

imaging and spectroscopic data one can determine the value of various dynamical parameters and better understand formation and early cluster evolution.

To date there have been a number of dynamical studies of LMC clusters including integrated spectra for several old and intermediate age clusters (Elson and Freeman 1985; Dubath *et al.* 1990; Mateo *et al.* 1991; and Meylan *et al.* 1991), individual stellar radial velocity measurements of intermediate age clusters (Seitzer 1991, Fischer *et al.* 1992b) and individual velocity measurements for young clusters (Lupton *et al.* 1989, Mateo *et al.* 1991, Fischer *et al.* 1992a). Assuming stars can be resolved right to the cluster core, the individual velocity measurements are favored over the integrated spectra. With stellar radial velocities one can include radial information in the dynamical models, rotation can be detected and quantified, escaping stars can be detected, and, if multi-epoch observations are available, favorably aligned binary stars can be found.

NGC 1850 is a very bright young cluster in the Bar region of the LMC. It is located in a region rich with star clusters and star formation and is, in fact, embedded in the emission nebula Henize 103. Furthermore, the cluster appears to be in a binary or perhaps even a triple system, and there is a clear indication of tidal interactions. The time is ripe for both photometric and kinematic studies of this object. Only recently have complete stellar isochrones appeared for high mass stars enabling one to determine ages more reliably than in the past. The use of photon-counting detectors enables high-precision radial velocity measurements for stars with apparent magnitudes as faint as $V = 18$ mag.

In §2.1 the CCD imaging is described and, in §2.2, a color-magnitude diagram is constructed and analyzed in order to derive an accurate age estimate. In §2.3 surface density profiles are derived and in §3 King-Michie models are applied to this data. §4 contains a description of the radial velocity observations and reductions.

§5 has the cluster mass estimates and §6 is a discussion of the cluster mass function. Finally §7 contains a calculation of the relaxation timescales for the cluster.

4.2   CCD IMAGING

4.2.1   The Data

BV CCD frames of NGC 1850 were obtained at the Las Campanas Observatory (LCO) 1.0 m telescope on 1991 February 23. The TEK2 1024^2 chip was used (readout noise $= 7$ e$^-$, gain $= 2$ e$^-$/ADU, and angular scale $= 0.61''$ px^{-1}). The exposure times were 60 seconds for each filter.

There are many interesting objects in the immediate vicinity (i.e. within about 6 arcminutes) of NGC 1850 as can be seen from Figs. 4.1 and 4.2. Fig 4.1 displays intensities around the median for the frame while Fig. 4.2 shows only the brighter stars. In Fig. 4.1 the cluster appears highly asymmetric with a large collection of stars slightly north of due east. This has been interpreted as both an interaction tail due to the presence of a binary companion (Bhatia and MacGillivray 1987) and as a cluster with a population distinct from the central cluster II88-159 (Bica et al. 1992, based on integrated photometry). Following the line joining the main cluster to this subcluster about 200 arcsec one finds a very low luminosity cluster. Approximately 100 arcsec south there is a diffuse object. Another, slightly higher luminosity cluster is located about 275 arcsec north of NGC 1850 and NGC 1855/54, a bright young cluster, lies to the south, with just its edge visible in this frame. Another interesting feature is revealed in Fig. 4.2 directly to the West of NGC 1850 with a center-to-center separation of 30 arcsec. This object has been previously designated by Bhatia and Hatzidimitriou (1988) as a distinct binary companion to NGC 1850 and according to Bica et al. is the probable source of ionizing radiation for the emission nebula Henize 103 in which these objects are embedded.
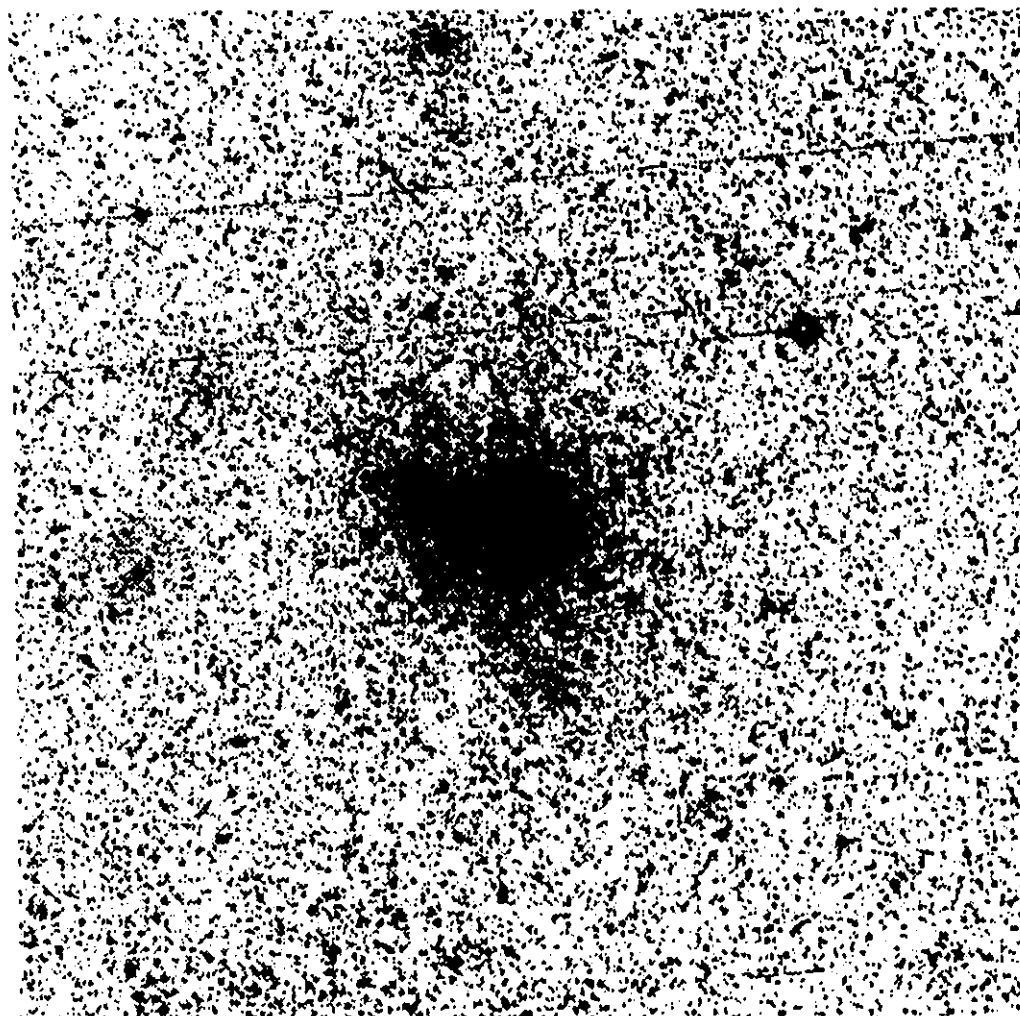
Fig. 4.1 - A B band CCD image of NGC 1850 displayed to highlight fainter features. The image is approximately 10' square with north at the top and east to the left.
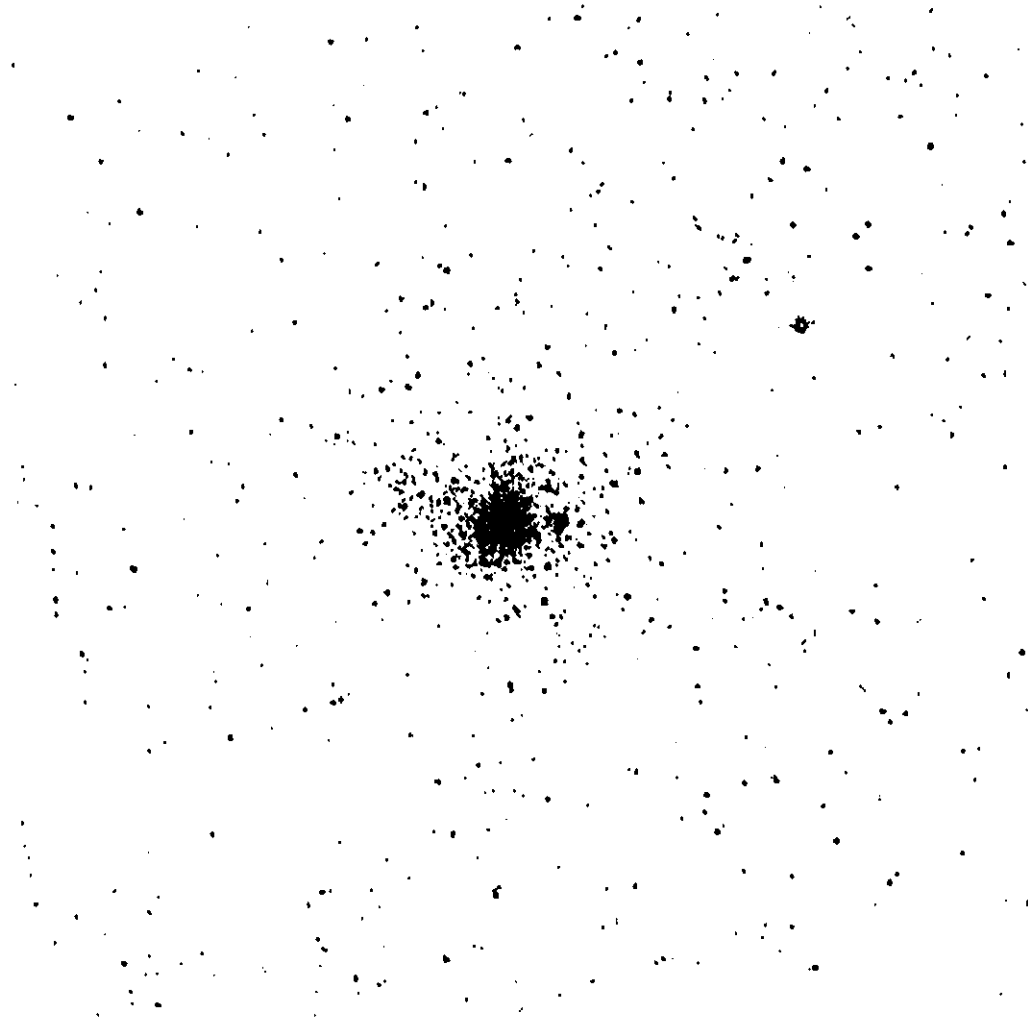
Fig. 4.2 - The same as Fig. 4.1 but displayed to show only the bright stars.

4.2.2   The Color-Magnitude Diagram

Stellar photometry was performed using DoPHOT (Mateo & Schechter 1989). As no standard stars were observed on this night the calibration was accomplished through the use of another set of NGC 1850 frames taken on 1990 November 5 using the same telescope, CCD and filters as above. On that night 12 BV observations of 9 E-region standards (Menzies *et al.* 1989) were observed covering an airmass range of 1.02 - 1.52 and a color range of -0.043 mag $\leq$ B-V $\leq$ 1.890 mag. The rms of the adopted solutions was approximately 0.02 mag. Aperture corrections yielded a zero-point with a similar accuracy and we conservatively estimate our absolute calibration to be accurate at better than 0.04 mag. Stars were then matched up between the two sets of frames to calibrate the present data. The reason for not using the older data for the current work is that the more recent frames had superior seeing which yielded improved stellar photometry particularly in the cluster's inner regions.

There have been at least three previous published photometric studies of NGC 1850. Robertson (1974) presented $(BV)_{pg}$ photographic photometry using an iris photometer and based his calibration on the $(BV)_{pe}$ photoelectric photometry of Tifft and Snell (1971). Alcaino & Liller (1987) presented photographic BVRI photometry also using an iris photometer and based their calibration on a 15 star photoelectric sequence (Alcaino & Liller 1982). Elson (1991) performed BV CCD photometry and based her calibration on four stars from Graham (1982), claiming a zero-point uncertainty of less than 0.01 mag. We have plotted the differences between our photometry and 44 stars from Robertson, 99 stars from Alcaino & Liller, and 190 stars from Elson in Figs. 4.3 through 4.5, respectively. The mean zero-point differences, in the sense of us–them, are $\Delta V_{Robertson} = 0.29$, $\Delta B_{Robertson} = 0.36$, $\Delta V_{A\&L} = 0.06$, $\Delta B_{A\&L} = 0.03$, and $\Delta V_{Elson} = -0.14$, $\Delta B_{Elson} = -0.10$, We are

fainter than Robertson and Alcaino & Liller, brighter than Elson, redder than both Robertson and Elson and bluer than Alcaino & Liller. There is a strong trend in both the B and V magnitude differences between ourselves and Robertson in the sense that the agreement becomes systematically worse for the fainter objects. Since this trend is not significantly present for the other two comparisons we conclude that the Robertson data is incorrect.

Fig. 4.6 shows an apparent BV color-magnitude diagram (CMD) for the entire 10′ square field. There is evidence for at least three distinct populations. Region 1 contains only very young stars still on the main sequence. Region 2 contains a mixture of the very young stars as well as a slightly older population of main sequence and evolved stars. Region three appears to consist of a significantly older population of evolved stars.

Fig. 4.7 contains a small subset of the stars found in Fig. 4.6. These are all the stars which were detected within 12 arcsec of the center of the binary companion located 30 arcsec to the west of the main cluster. In fact, there are many more stars in this region but unfortunately the inner region of the companion cluster was saturated on the 60s frames. Even with a shorter exposure we suspect that the extremely high degree of crowding in this region would render stellar photometry both difficult and unreliable. In any case, one can see that nearly all the detected stars are blue and they extend beyond the clearly delineated turnoff region obvious in Fig. 4.6 indicating a very young system.

We attempted to fit isochrones from Mermilliod et al. 1992 to the photometry data. These isochrones incorporate the new radiative opacities from Iglesias & Rogers (1991), convective overshooting and mass-loss (see Schaller et al. 1992 for a complete description of the stellar models). Isochrones were available for z=0.0188 (solar abundance). $z = 0.008$, and z=0.001. There are two published photometric
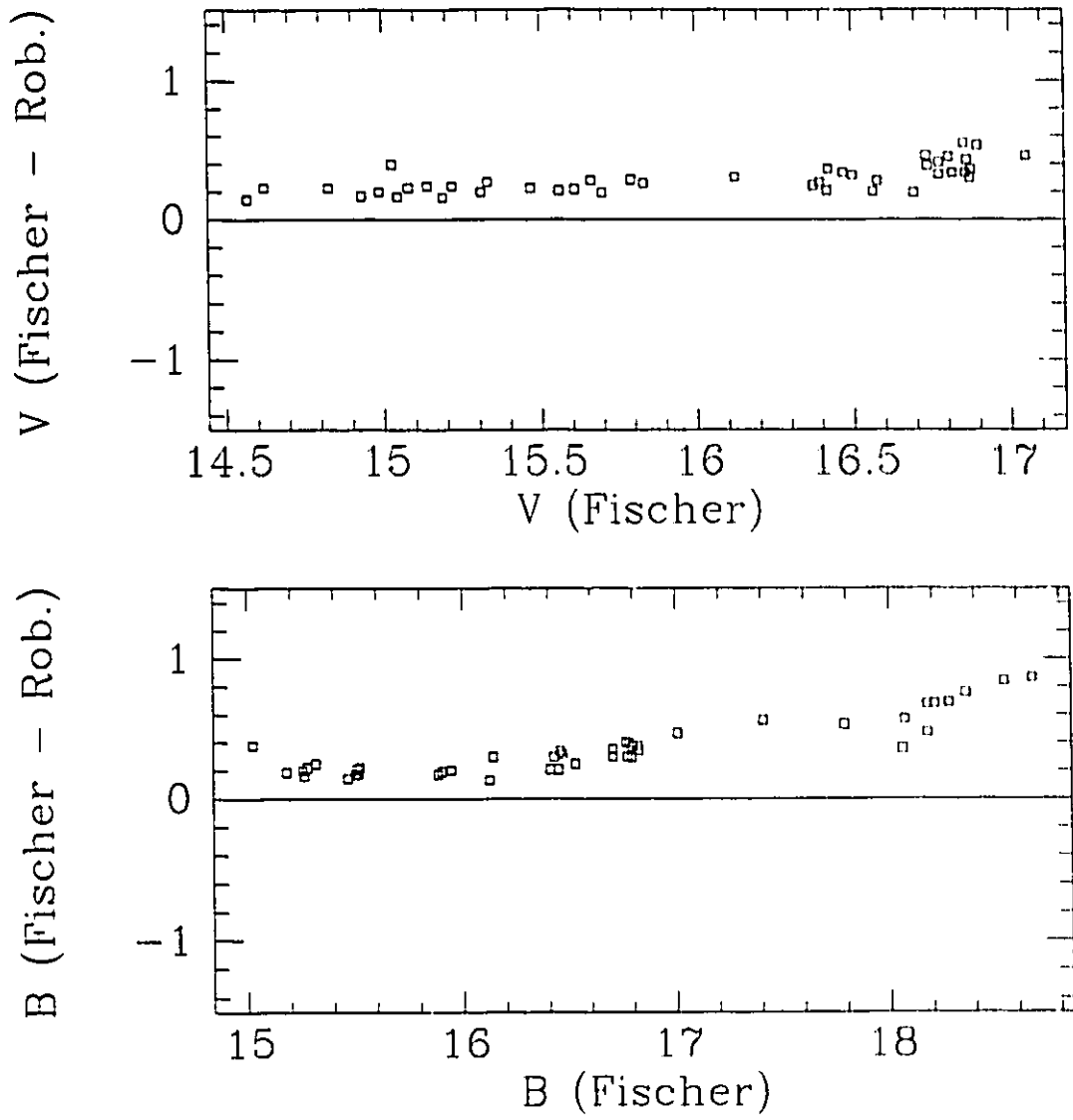
Fig. 4.3 - Comparison between photometry from this work and Robertson (1974). The zero-point differences can be found in the text.
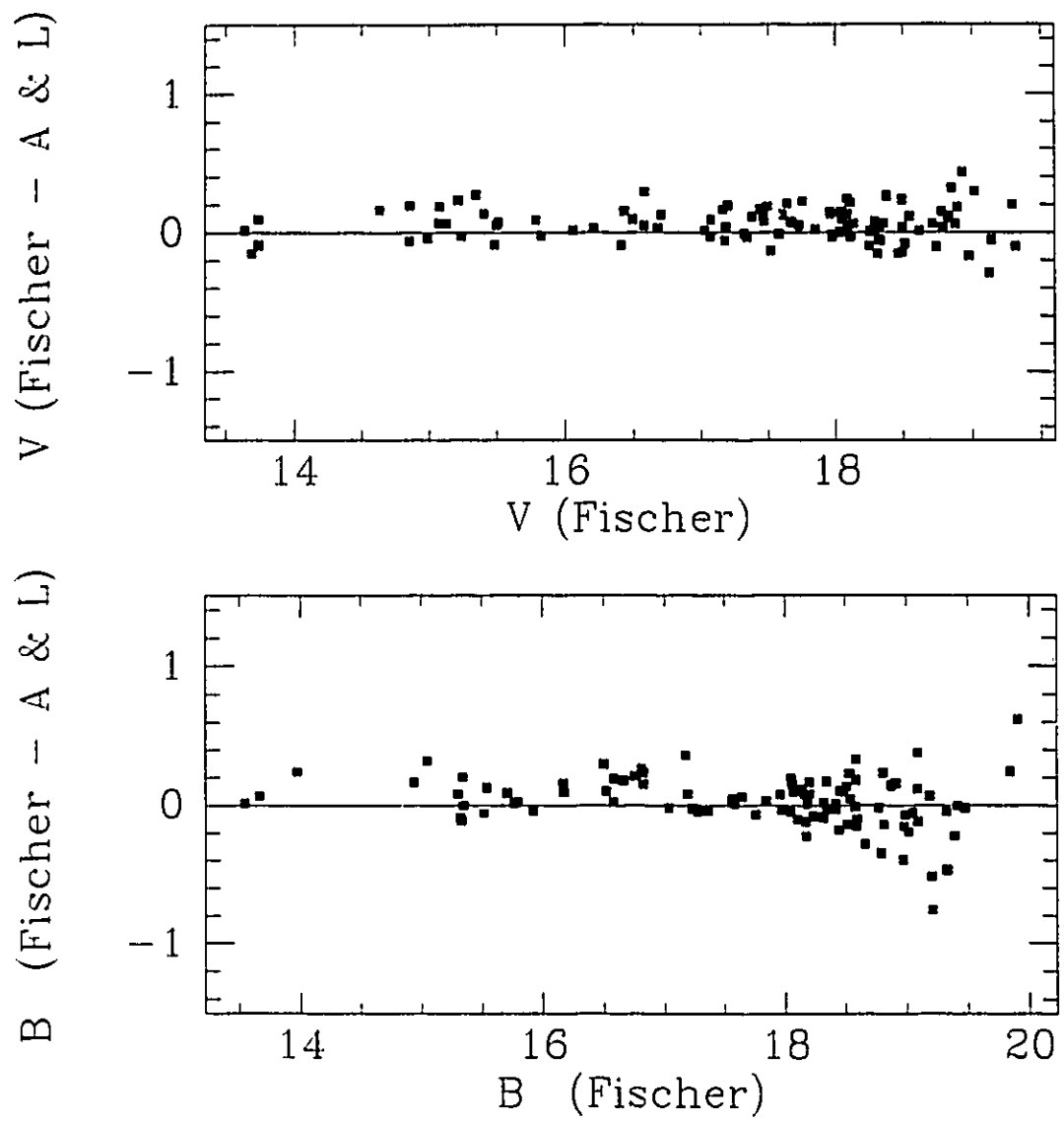
Fig. 4.4 - The same as figure 4.3 but for the photometry from Alcaino & Liller (1987).
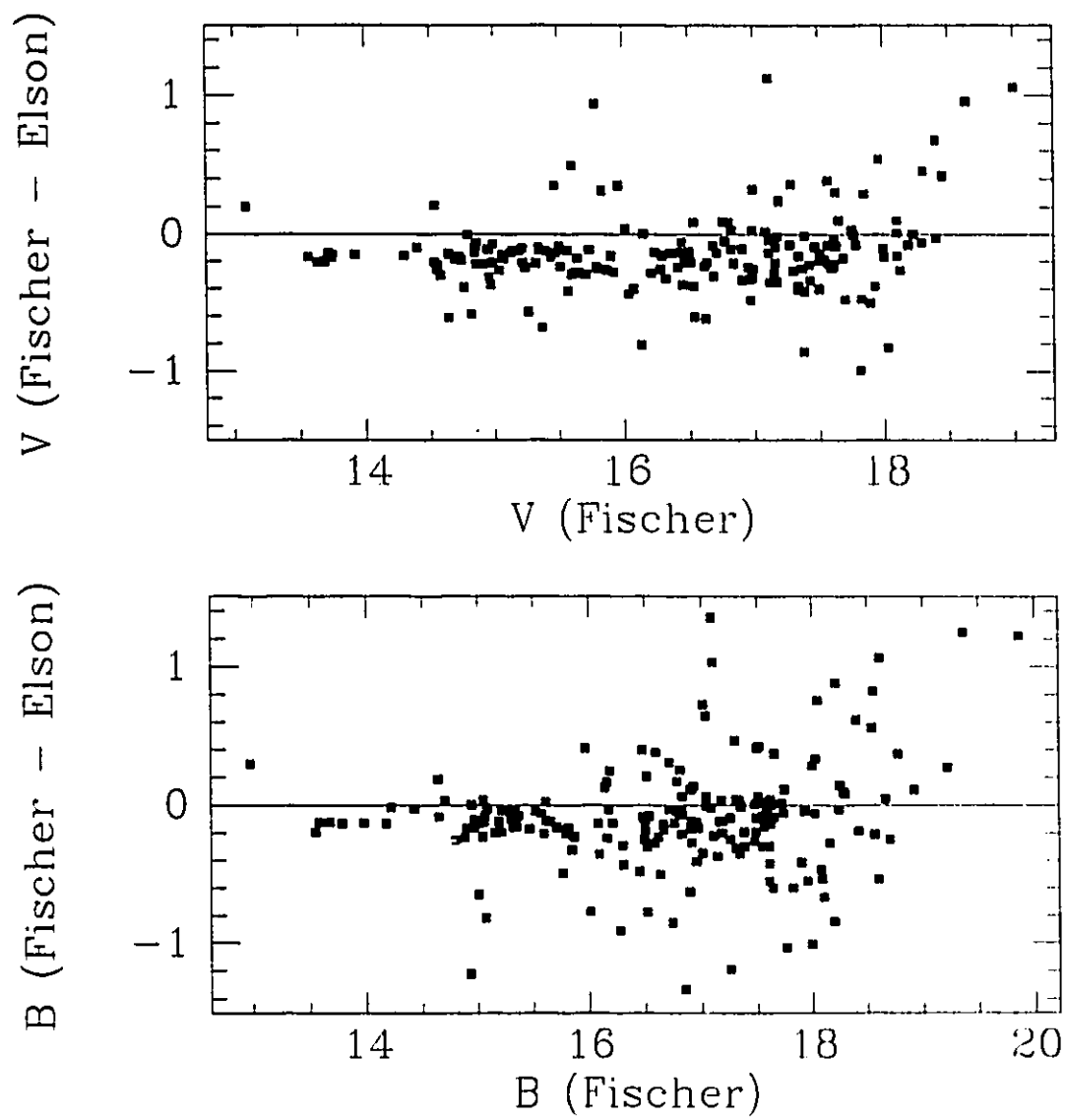
Fig. 4.5 - The same as figure 4.3 but for the photometry from (Elson 1991)
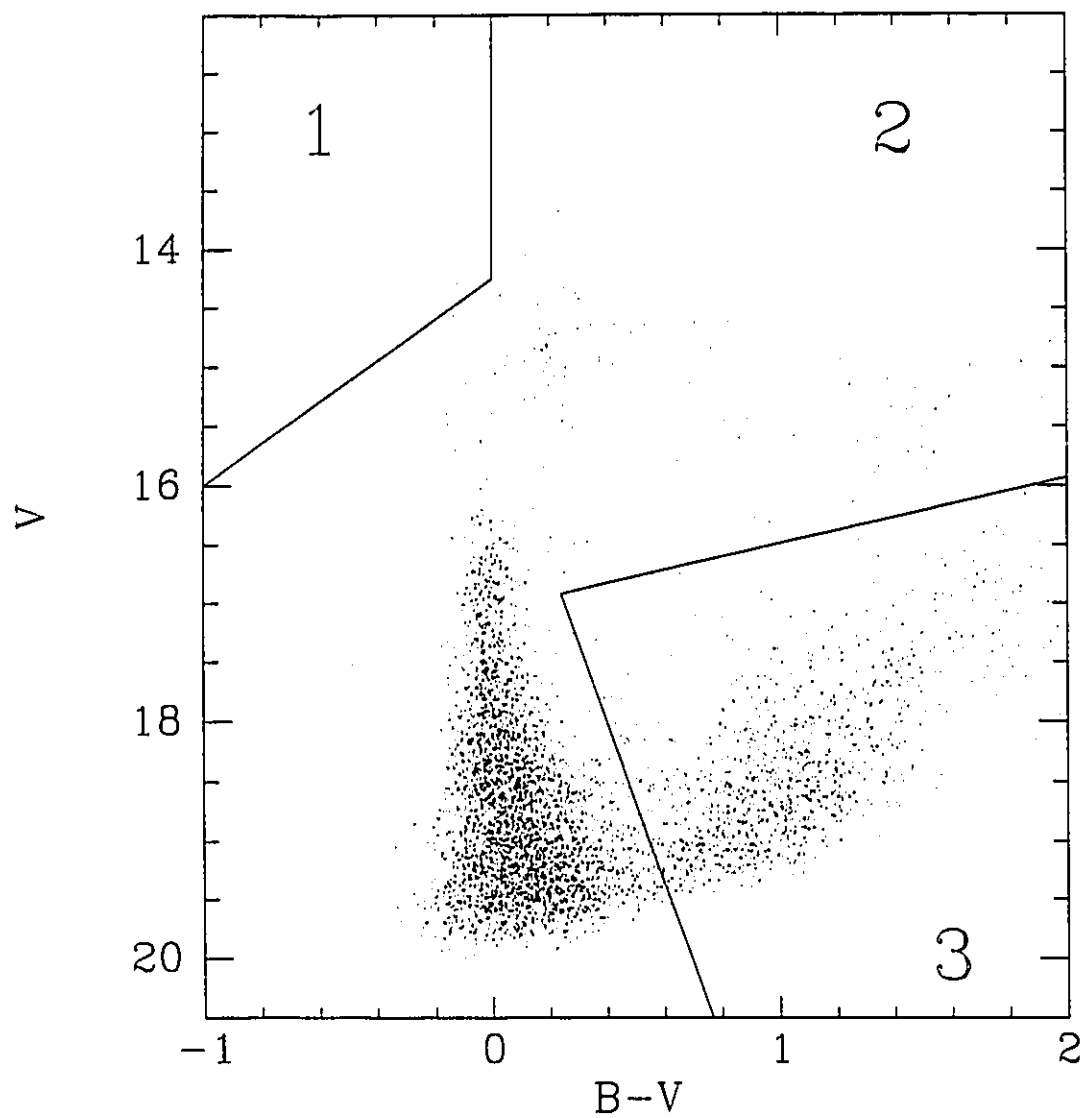
Fig. 4.6 - BV color-magnitude diagram for the entire 10′ field surrounding NGC 1850. The numbers correspond to three distinct populations (see text).
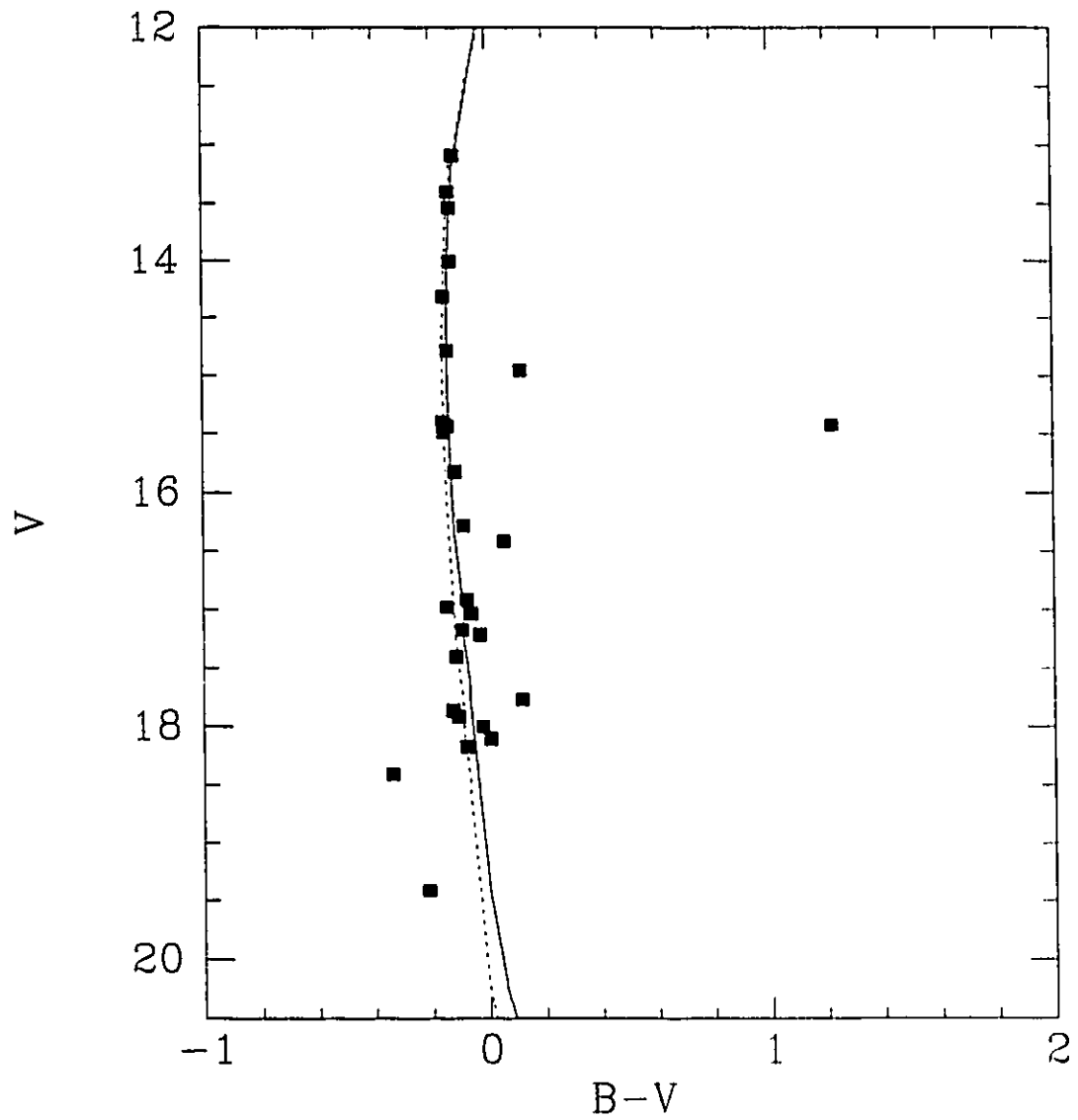
Fig. 4.7 - BV color-magnitude diagram for the region within 12″ of center of the companion cluster (see Fig. 4.2). The solid line corresponds to the isochrone with $z = 0.008$ while the broken line has $z = 0.001$. Both sets of isochrones have ages of $\tau = 6$ Myr, as well as $(m-M)_0 = 18.5$ and $E(B-V) = 0.17$ mag.

metallicity determinations for NGC 1850: the first based on Washington photometry of two stars yielding z = 0.009 (Schommer & Geisler 1986), and the second based on Strömgren photometry of five stars yielding z = 0.004 (Grebel *et al.* 1992).

In Fig. 4.7 one can see the result of the isochrone fitting to the stars of the companion cluster. The inferred reddening was E(B–V) = 0.17 ±0.03 mag [A_V = 3.1E(B–V) was assumed]. The presence of the young, barely-evolved, companion provides an excellent opportunity to accurately determine the reddening and our value agrees well with three previous reddening determinations. Persson *et al.* (1983) find E(B–V) = 0.15 mag using the technique outlined in Cohen *et al.* (1981) involving both optical and IR broadband color indices. Alcaino and Liller (1987) obtained E(B–V) = 0.18 mag from a BVRI CMD study and Lee (1991) found E(B–V) = 0.15 ± 0.05 for UBV photometry. The best age is τ = 6±5 Myr. This changes by less than 1 Myr as one varies the distance modulus by ±0.3 mag.

Fig. 4.8 is a CMD for the region within 1′ of the center of the main cluster (it includes all the stars in Fig. 4.7). The apparent BV magnitudes for this inner region are presented in Table 4.1. Column 1, 6 and 11 are the stellar identifications, column 2, 7 and 12 are the X positions on the CCD (increases towards the south), column 3, 8 and 13 are the Y positions (increasing towards the east), columns 4, 9, and 14 are the apparent V magnitudes, and columns 5, 10, and 15 are the apparent B-V magnitudes.

The two younger isochrones in Fig. 4.8 are identical to those discussed above while the older set are for τ = 90 Myr. We have adopted the reddening obtained above using the young stars. Our age estimate is therefore τ = 90 ± 30 Myr, where the error estimate takes into account the uncertainty in the zero-point and reddening and the difficulty in fitting the isochrones to this crowded data set. Varying the distance modulus by ±0.3 affects the age estimate by approximately 10 Myr. Fig

Table 4.1

BV Photometry

ID	X	Y	V	B-V	ID	X	Y	V	B-V	ID	X	Y	V	B-V
1	511.8	417.2	18.04	1.04	51	505.7	444.8	18.04	-0.04	101	528.5	463.9	13.40	-0.14
2	528.8	418.0	18.75	-0.15	52	545.1	445.0	18.54	-0.14	102	498.6	464.4	14.64	0.29
3	541.4	418.1	16.37	-0.00	53	485.8	445.1	18.08	0.03	103	466.2	464.5	16.84	1.58
4	502.5	419.7	18.44	1.23	54	530.6	445.2	14.79	-0.14	104	548.6	464.5	16.06	0.11
5	521.2	419.9	16.28	-0.19	55	550.8	445.7	16.01	0.18	105	555.2	465.2	18.49	-0.03
6	545.2	420.4	18.85	-0.07	56	498.4	446.3	18.30	-0.10	106	481.9	465.3	17.01	-0.05
7	498.8	422.3	17.07	-0.02	57	492.8	446.5	18.48	0.02	107	534.1	465.3	14.01	-0.13
8	506.3	423.8	16.95	-0.02	58	516.4	446.6	16.42	0.05	108	518.2	465.9	16.98	-0.15
9	552.8	426.0	15.90	-0.05	59	463.3	447.1	19.48	-0.01	109	526.0	466.2	15.40	-0.16
10	544.8	426.5	16.82	-0.08	60	579.3	447.2	17.81	-0.03	110	607.7	466.4	17.95	-0.11
11	558.7	426.6	18.51	-0.02	61	549.8	447.9	16.87	-0.11	111	485.1	466.5	18.02	-0.00
12	533.7	426.8	18.14	0.09	62	594.6	448.0	18.78	0.00	112	542.2	466.8	15.48	-0.16
13	480.4	427.3	18.40	-0.00	63	565.7	448.0	18.81	-0.19	113	610.3	467.1	17.35	0.11
14	522.6	429.1	17.82	-0.03	64	570.4	448.9	18.53	0.38	114	480.2	467.4	17.00	0.07
15	499.4	429.4	17.30	-0.05	65	534.8	450.1	18.18	-0.08	115	477.9	467.6	17.99	-0.16
16	572.9	429.4	18.86	0.19	66	486.8	451.3	17.99	-0.07	116	562.6	468.7	16.83	-0.00
17	531.8	429.4	18.64	-0.10	67	552.1	451.5	19.08	-0.14	117	459.1	468.8	16.97	-0.00
18	565.5	430.2	18.98	-0.06	68	589.2	452.1	17.85	-0.06	118	511.2	469.1	17.17	-0.10
19	502.7	430.2	18.86	-0.20	69	463.8	452.2	17.17	-0.01	119	534.6	469.5	17.22	-0.03
20	537.0	430.3	18.84	-0.09	70	554.9	452.5	18.34	-0.11	120	584.5	469.6	17.81	-0.05
21	523.9	432.8	17.08	-0.04	71	515.3	452.6	17.91	-0.11	121	555.6	469.6	18.05	-0.14
22	579.2	434.0	18.39	-0.09	72	452.9	452.8	18.17	-0.17	122	567.2	470.3	17.54	0.02
23	569.2	435.5	16.51	-0.01	73	572.1	452.9	16.81	-0.01	123	528.1	470.5	18.41	-0.34
24	476.1	435.8	17.03	-0.01	74	494.1	453.8	16.53	1.45	124	549.2	470.6	18.45	-0.16
25	511.8	435.8	17.62	0.08	75	541.1	454.9	17.86	-0.13	125	575.1	470.8	17.11	-0.01
26	466.5	437.0	18.06	-0.05	76	491.9	455.3	15.76	1.46	126	523.4	470.9	17.77	0.12
27	504.5	437.4	18.75	0.31	77	556.4	455.6	18.94	-0.25	127	494.3	471.2	13.69	-0.14
28	490.7	437.7	18.15	0.07	78	515.5	456.9	16.28	-0.09	128	544.7	471.7	17.58	-0.10
29	471.6	437.9	15.92	-0.06	79	590.4	457.0	17.16	-0.08	129	608.3	471.7	18.34	0.07
30	539.8	437.9	16.81	0.02	80	492.2	457.1	17.09	1.47	130	439.6	471.9	17.60	0.07
31	480.3	439.0	17.24	0.95	81	542.5	457.6	15.83	-0.12	131	552.8	472.2	17.14	-0.09
32	502.0	439.2	17.62	-0.06	82	522.5	457.8	16.92	-0.08	132	445.7	472.6	18.81	-0.21
33	572.7	439.2	18.65	0.22	83	556.2	457.9	17.64	-0.05	133	530.5	473.3	18.01	-0.02
34	531.5	439.2	17.79	-0.08	84	532.6	458.0	18.18	0.18	134	473.9	473.6	16.66	-0.10
35	486.7	440.0	15.81	0.01	85	527.6	458.2	14.32	-0.16	135	513.8	473.7	15.43	1.22
36	512.0	440.3	17.78	-0.16	86	443.2	459.1	18.44	0.00	136	524.2	474.4	14.96	0.12
37	581.7	441.1	17.11	-0.04	87	521.1	459.4	15.43	-0.14	137	450.7	474.7	19.29	0.12
38	589.4	441.5	18.64	0.04	88	460.3	459.7	15.06	1.02	138	613.5	474.8	18.38	0.01
39	572.5	441.5	18.04	-0.06	89	569.7	460.4	18.61	0.03	139	459.8	475.1	17.82	0.07
40	464.3	441.7	16.90	1.46	90	487.1	460.8	17.82	0.09	140	568.6	475.6	17.63	-0.15
41	549.6	441.8	18.11	-0.04	91	539.8	461.2	19.41	-0.22	141	472.3	476.2	17.20	-0.11
42	569.3	441.8	19.04	-0.07	92	524.3	461.5	13.54	-0.13	142	550.6	476.4	16.81	0.00
43	527.8	443.0	15.39	1.28	93	492.7	461.7	17.33	-0.07	143	492.8	476.7	17.07	-0.07
44	558.1	443.1	17.75	-0.12	94	534.0	461.9	17.04	-0.06	144	457.3	477.0	17.50	1.11
45	587.1	443.6	16.20	-0.04	95	557.8	462.6	17.06	-0.06	145	466.2	477.1	17.60	-0.09
46	540.8	443.6	18.43	0.20	96	469.1	462.8	17.22	-0.03	146	494.6	477.7	17.64	-0.16
47	492.4	443.9	17.94	-0.06	97	523.6	463.2	13.09	-0.12	147	579.6	477.9	17.76	-0.02
48	523.3	444.4	18.11	0.00	98	495.5	463.2	16.72	0.72	148	532.3	478.1	18.17	-0.08
49	471.0	444.4	19.15	0.06	99	451.6	463.4	18.75	0.13	149	566.4	478.3	13.74	0.24
50	573.9	444.5	17.68	-0.05	100	579.6	463.9	17.67	0.10	150	588.6	478.5	18.13	0.63

Table 4.1 (cont.)

BV Photometry

ID	X	Y	V	B-V	ID	X	Y	V	B-V	ID	X	Y	V	B-V
151	559.0	478.8	17.77	-0.03	201	535.1	492.3	15.31	0.98	251	542.2	502.8	14.76	0.12
152	613.8	478.9	14.85	0.50	202	586.1	492.4	18.30	-0.06	252	469.2	503.1	17.36	-0.04
153	481.1	479.1	18.48	-0.17	203	540.5	492.7	17.08	0.10	253	488.7	503.5	18.32	0.04
154	472.8	479.4	16.73	-0.00	204	469.1	493.1	17.47	0.07	254	511.9	503.6	14.72	0.13
155	529.5	479.5	17.41	-0.12	205	572.0	493.3	18.20	0.03	255	595.2	503.8	18.15	0.14
156	562.3	480.1	18.37	-0.06	206	495.2	493.5	16.25	-0.05	256	479.4	504.0	18.11	-0.04
157	569.4	480.1	17.32	0.04	207	567.3	493.7	15.42	-0.09	257	534.4	504.3	16.86	-0.08
158	556.0	480.4	17.33	0.00	208	463.9	493.8	15.79	-0.02	258	454.3	504.4	15.65	1.24
159	485.3	480.6	18.58	-0.24	209	554.9	493.8	15.40	1.26	259	499.9	504.4	13.56	0.65
160	468.2	481.1	16.56	-0.05	210	432.3	494.2	18.53	-0.03	260	467.2	504.7	17.38	-0.05
161	591.7	481.2	18.54	-0.04	211	560.5	494.2	18.63	0.32	261	494.5	505.0	15.36	0.86
162	574.4	481.4	18.37	-0.06	212	607.0	494.2	18.31	0.01	262	484.4	505.4	15.37	1.44
163	581.5	481.8	19.10	0.03	213	437.0	494.2	14.85	0.19	263	580.5	505.6	18.60	0.31
164	587.7	482.1	16.90	0.05	214	484.6	494.3	17.68	-0.02	264	477.8	506.2	18.05	0.10
165	502.4	482.7	17.61	-0.03	215	593.2	494.8	18.78	0.05	265	447.1	506.6	16.69	-0.08
166	536.7	482.9	16.74	-0.07	216	475.9	494.8	17.99	0.03	266	552.3	507.5	18.12	-0.06
167	508.6	483.1	15.56	0.88	217	574.4	495.6	18.96	0.33	267	584.0	507.7	18.13	0.18
168	462.0	483.2	18.35	-0.12	218	523.7	495.9	16.01	0.09	268	574.3	507.9	18.12	0.04
169	442.6	483.7	18.90	-0.10	219	540.8	495.9	17.22	0.06	269	568.8	507.9	19.12	-0.13
170	598.9	484.2	13.74	-0.07	220	480.5	496.3	16.53	-0.02	270	558.2	508.4	15.81	0.10
171	435.0	484.5	19.30	-0.32	221	547.4	496.4	16.73	-0.01	271	510.1	508.6	15.86	-0.24
172	484.5	484.7	18.18	-0.03	222	508.1	496.4	15.06	0.90	272	479.1	509.0	17.12	0.03
173	539.8	484.7	14.26	0.78	223	598.0	496.7	17.95	-0.04	273	449.1	509.1	18.48	-0.03
174	545.7	485.1	17.19	0.11	224	453.2	496.7	17.95	-0.05	274	527.3	509.1	16.19	-0.17
175	532.4	485.3	15.21	1.40	225	491.2	497.0	16.62	-0.04	275	578.8	509.2	18.41	-0.02
176	478.2	485.5	17.64	0.18	226	467.5	497.2	18.17	-0.05	276	499.1	509.6	16.85	0.09
177	474.4	485.5	14.94	0.27	227	483.9	497.4	18.40	0.20	277	608.8	509.6	17.20	0.07
178	469.7	485.5	18.30	0.14	228	504.5	497.6	16.32	-0.04	278	475.2	509.7	17.50	0.00
179	613.8	485.8	18.76	0.09	229	487.2	497.7	17.42	0.93	279	554.4	509.8	17.41	-0.07
180	565.4	486.0	18.93	0.28	230	559.2	498.3	18.20	0.19	280	540.8	510.1	17.94	-0.22
181	526.8	486.0	17.16	-0.15	231	561.7	498.8	18.42	-0.03	281	491.3	510.2	15.94	-0.02
182	535.9	486.0	14.74	0.20	232	578.8	498.8	17.23	0.00	282	432.2	510.6	16.78	-0.00
183	440.6	486.3	19.15	-0.12	233	440.8	498.9	18.68	-0.02	283	604.6	511.1	14.96	0.38
184	595.7	486.4	18.07	-0.18	234	541.7	499.0	17.90	0.01	284	528.5	511.2	14.69	0.86
185	448.4	487.3	16.80	0.01	235	609.4	499.0	17.93	0.00	285	425.5	511.3	17.45	-0.02
186	463.1	487.6	17.08	0.02	236	515.0	499.0	15.86	1.01	286	587.2	511.5	18.55	0.10
187	458.5	487.8	17.94	0.03	237	572.1	499.2	18.42	0.07	287	440.1	511.6	18.18	0.03
188	561.9	487.9	18.57	0.06	238	463.8	499.6	16.29	-0.13	288	485.5	511.6	16.27	-0.07
189	468.8	488.0	18.95	-0.11	239	426.1	500.5	16.96	0.03	289	567.5	511.7	18.56	-0.16
190	504.4	488.3	16.57	-0.01	240	467.0	500.5	17.52	0.06	290	512.7	511.9	14.57	0.10
191	534.4	488.5	16.33	-0.04	241	445.7	501.3	17.96	-0.02	291	492.1	512.2	14.87	0.17
192	552.3	488.6	18.20	-0.07	242	437.6	501.4	17.78	0.10	292	599.7	512.4	16.83	0.12
193	485.0	489.7	18.23	-0.13	243	464.9	501.5	16.99	0.03	293	532.5	512.7	14.62	0.15
194	573.6	490.9	16.53	0.06	244	481.2	501.5	17.08	0.03	294	550.9	513.1	17.03	-0.28
195	482.5	491.1	17.91	-0.24	245	497.1	501.8	16.02	-0.04	295	582.4	513.1	18.50	-0.02
196	563.9	491.3	18.11	-0.01	246	430.1	502.4	15.24	0.09	296	530.1	513.3	14.85	0.18
197	613.2	491.4	18.48	0.17	247	475.6	502.5	16.25	-0.03	297	447.7	513.5	17.99	0.06
198	505.7	491.5	15.30	0.13	248	601.9	502.5	17.26	-0.03	298	591.5	513.5	18.53	0.09
199	448.4	491.6	18.77	0.25	249	535.8	502.6	16.70	-0.12	299	573.2	513.5	18.63	-0.15
200	530.6	492.0	17.28	0.01	250	574.4	502.7	15.47	1.71	300	615.0	513.6	17.80	-0.03

Table 4.1 (cont.)

BV Photometry

ID	X	Y	V	B-V	ID	X	Y	V	B-V	ID	X	Y	V	B-V
301	542.6	513.9	16.48	0.01	351	560.8	526.2	15.39	1.09	401	499.4	538.7	16.38	0.03
302	488.2	513.9	14.76	1.21	352	538.0	526.3	15.40	-0.00	402	535.9	538.7	15.33	0.01
303	426.7	514.4	18.95	-0.20	353	575.7	526.4	18.32	0.07	403	547.4	539.0	17.33	-0.16
304	480.5	514.5	15.46	1.53	354	471.4	526.5	19.00	0.07	404	557.1	539.2	17.01	-0.10
305	423.9	514.8	17.40	0.04	355	540.7	526.7	16.60	-0.07	405	528.4	539.4	17.88	0.22
306	434.4	515.2	18.19	0.23	356	520.2	526.9	14.43	0.31	406	552.5	539.5	16.86	0.01
307	602.5	515.3	17.80	0.16	357	509.0	527.4	17.81	0.45	407	571.8	539.7	18.47	0.08
308	451.4	515.4	17.97	0.16	358	552.0	528.2	18.13	0.29	408	602.8	540.0	18.01	0.20
309	559.7	515.5	16.57	0.16	359	466.5	528.2	19.05	-0.08	409	443.4	540.0	18.02	0.06
310	583.6	515.6	17.95	0.00	360	580.5	528.2	18.81	0.10	410	437.4	540.7	18.71	-0.04
311	576.4	515.6	18.07	0.09	361	555.0	528.3	17.76	0.17	411	524.8	540.7	16.93	0.01
312	462.4	515.9	18.75	-0.17	362	613.1	528.6	15.44	2.08	412	612.0	540.9	19.13	0.62
313	550.7	516.2	15.70	-0.11	363	480.7	528.7	17.84	-0.09	413	483.6	541.0	18.59	-0.17
314	540.9	516.6	17.23	0.35	364	517.3	528.8	16.63	0.03	414	435.2	541.2	17.97	0.05
315	497.6	517.0	17.58	-0.04	365	558.2	529.1	16.83	0.12	415	443.5	542.2	18.91	0.01
316	558.6	517.0	17.19	0.07	366	473.2	529.1	16.95	0.04	416	495.7	542.2	17.07	0.04
317	580.7	517.0	16.35	1.29	367	535.2	529.3	14.53	0.17	417	588.5	542.5	17.24	-0.31
318	530.2	517.7	15.44	0.63	368	566.6	530.0	17.73	-0.09	418	530.9	543.0	16.70	0.06
319	542.5	518.4	16.77	0.06	369	501.5	530.5	15.68	1.64	419	511.7	543.3	17.15	-0.12
320	477.0	518.5	14.97	0.19	370	569.7	531.2	15.64	1.46	420	556.2	543.5	17.24	0.17
321	494.9	518.5	17.78	0.09	371	467.4	531.2	18.48	0.29	421	609.8	544.0	19.23	0.12
322	488.0	519.2	15.34	1.24	372	589.8	531.5	18.32	0.02	422	589.9	544.1	14.84	1.75
323	566.0	519.2	17.21	0.13	373	498.7	532.1	17.43	-0.25	423	571.7	544.4	18.28	0.14
324	501.5	519.3	15.58	0.30	374	561.8	532.2	16.87	0.02	424	558.7	544.9	15.36	1.55
325	555.5	519.4	17.29	-0.24	375	508.3	532.3	17.35	0.06	425	564.4	545.3	18.16	0.20
326	481.0	519.4	18.11	-0.03	376	539.9	532.5	16.48	0.34	426	515.5	546.6	15.60	1.34
327	551.5	519.7	17.53	-0.49	377	514.5	533.0	15.56	1.31	427	569.2	547.0	16.03	0.10
328	575.3	519.8	17.61	0.09	378	528.9	533.2	15.39	1.42	428	441.4	547.3	17.96	0.02
329	457.3	520.2	17.62	0.10	379	517.2	533.3	15.78	0.03	429	520.1	547.7	17.21	0.00
330	610.8	520.4	14.99	0.31	380	556.8	533.5	18.08	0.03	430	510.9	548.0	17.16	0.02
331	543.1	520.6	17.60	-0.05	381	560.0	533.6	16.84	-0.05	431	559.6	548.0	16.94	-0.01
332	484.4	520.7	15.86	1.33	382	548.6	534.0	14.81	0.19	432	471.2	548.1	17.92	0.04
333	498.2	520.7	15.86	1.24	383	526.3	534.0	16.70	-0.16	433	488.0	548.2	14.94	1.22
334	433.3	520.9	18.10	-0.15	384	539.2	534.6	15.27	0.15	434	434.0	548.5	18.32	-0.11
335	505.2	521.6	16.74	0.24	385	572.9	535.0	15.79	0.06	435	475.9	548.5	18.32	-0.26
336	467.7	521.8	15.56	1.22	386	466.8	535.0	18.52	-0.03	436	499.9	548.8	17.72	-0.10
337	443.7	522.2	15.13	1.70	387	595.0	535.5	16.90	0.01	437	528.8	549.9	17.36	0.07
338	478.7	522.5	15.70	1.58	388	483.2	535.6	15.64	1.27	438	586.5	550.2	18.33	0.21
339	564.5	522.9	17.22	-0.02	389	504.1	535.7	18.06	0.03	439	547.5	550.2	16.45	0.03
340	585.2	522.9	17.55	0.08	390	617.9	536.1	19.36	0.21	440	451.8	550.7	18.12	0.01
341	556.8	522.9	14.89	0.24	391	570.5	536.2	15.41	1.43	441	559.5	550.7	15.71	1.28
342	447.6	523.0	18.07	0.11	392	510.1	536.2	17.38	0.05	442	551.0	550.7	17.89	0.15
343	536.9	523.1	17.87	-0.12	393	543.0	536.4	14.55	0.25	443	515.0	550.9	17.16	-0.09
344	509.2	523.2	16.30	0.04	394	560.2	536.5	14.91	0.25	444	491.5	551.1	18.06	0.08
345	611.0	524.2	17.34	0.42	395	491.0	536.7	18.66	0.24	445	540.2	551.2	17.22	-0.72
346	559.6	524.3	14.53	0.11	396	556.7	536.9	14.83	0.19	446	533.4	551.2	17.36	0.18
347	486.8	524.5	17.24	0.00	397	435.0	537.1	18.29	0.08	447	432.1	551.3	18.52	0.15
348	516.6	524.6	15.97	0.13	398	427.1	538.0	17.85	-0.01	448	553.5	551.6	17.01	0.02
349	505.5	525.5	15.59	1.05	399	600.6	538.3	18.00	0.24	449	455.8	551.6	17.14	0.00
350	442.8	526.2	18.51	0.04	400	524.0	538.3	14.99	0.05	450	565.8	552.5	17.79	0.02

Table 4.1 (cont.)

BV Photometry

ID	X	Y	V	B-V	ID	X	Y	V	B-V	ID	X	Y	V	B-V
451	571.9	552.6	18.65	0.00	501	497.5	564.2	13.68	0.23	551	483.9	578.0	18.48	-0.05
452	470.0	552.7	18.05	0.26	502	484.0	565.6	17.61	-0.02	552	505.1	578.9	17.34	-0.03
453	534.5	553.1	17.35	-0.13	503	471.4	566.3	18.08	0.02	553	494.5	579.1	16.59	-0.00
454	544.1	553.2	17.38	-0.14	504	527.4	566.6	17.36	0.02	554	564.9	579.4	19.23	0.03
455	578.6	553.6	17.81	0.16	505	607.7	566.6	16.79	1.65	555	554.7	579.4	16.89	-0.01
456	463.0	553.7	18.96	-0.21	506	562.8	566.6	18.17	-0.01	556	577.4	579.7	18.72	0.29
457	481.0	554.2	16.42	-0.12	507	595.6	567.3	18.46	0.22	557	487.6	580.2	18.59	0.11
458	527.8	554.2	15.96	1.34	508	574.6	567.4	16.94	0.09	558	509.2	580.2	18.63	0.07
459	457.2	554.3	16.76	-0.05	509	585.8	567.6	16.06	1.48	559	519.5	580.8	16.89	0.08
460	531.7	554.5	17.02	-0.10	510	441.2	567.8	14.87	0.11	560	469.2	581.8	15.32	0.14
461	545.5	554.8	17.61	-0.17	511	556.0	567.9	18.87	0.41	561	556.2	582.1	18.82	-0.05
462	559.3	555.2	17.63	0.15	512	486.7	568.2	18.29	0.01	562	575.5	582.2	17.63	0.03
463	460.4	555.6	17.18	0.08	513	483.2	569.0	18.13	0.06	563	462.8	582.2	18.28	-0.02
464	485.8	555.6	17.69	0.04	514	520.5	569.1	14.68	0.30	564	581.4	582.3	18.50	0.12
465	448.6	555.7	18.83	0.05	515	462.7	569.3	19.03	-0.25	565	505.0	583.3	18.81	0.12
466	435.8	555.8	19.18	0.13	516	470.6	569.9	18.41	0.07	566	511.0	584.0	15.60	1.02
467	529.0	555.9	15.90	1.33	517	465.2	570.0	17.34	0.18	567	473.9	584.6	17.88	0.07
468	611.1	556.1	19.25	0.09	518	541.8	570.0	17.73	0.10	568	561.5	585.4	17.70	0.84
469	509.6	556.4	17.78	-0.00	519	561.4	570.3	18.12	-0.06	569	460.4	585.7	17.28	0.16
470	478.5	556.5	15.40	0.00	520	546.8	570.3	17.76	-0.04	570	523.5	585.8	19.06	-0.20
471	506.1	556.7	15.46	1.63	521	479.0	570.3	17.82	-0.26	571	514.3	585.9	18.76	0.30
472	493.9	556.7	17.72	-0.08	522	598.3	570.3	18.06	0.05	572	493.4	586.0	19.07	-0.34
473	482.3	557.2	18.22	0.07	523	514.1	570.5	18.15	0.13	573	549.5	586.3	18.42	0.14
474	569.7	557.5	17.92	0.11	524	584.9	571.2	17.95	0.13	574	496.6	586.8	17.85	0.12
475	600.8	557.7	19.09	0.13	525	553.0	571.4	18.88	0.10	575	481.8	587.1	18.55	0.08
476	540.2	557.7	17.84	-0.08	526	481.9	571.5	18.59	0.01	576	457.7	587.2	16.07	1.41
477	498.1	557.8	17.77	-0.08	527	451.8	572.0	19.15	0.05	577	486.0	587.4	17.25	0.23
478	543.0	558.5	17.82	0.09	528	496.8	572.2	16.53	0.01	578	500.5	587.5	18.73	0.14
479	551.6	558.8	17.92	0.05	529	475.6	572.2	16.88	-0.34	579	544.1	587.8	18.06	-0.08
480	486.8	559.2	16.39	1.43	530	557.1	572.2	18.15	-0.07	580	588.2	588.1	19.18	0.04
481	526.7	559.8	18.47	0.06	531	504.1	572.5	18.76	-0.22	581	490.8	588.1	16.25	0.42
482	582.0	560.1	17.55	0.06	532	471.6	572.6	16.54	0.08	582	502.7	588.9	16.98	0.51
483	474.2	560.2	19.02	0.08	533	499.3	572.9	16.15	-0.08	583	549.2	589.2	18.07	0.01
484	523.2	560.6	18.32	-0.03	534	600.2	573.0	18.59	0.30	584	505.7	589.8	17.76	-0.01
485	485.2	560.6	16.07	0.64	535	468.0	573.6	18.01	0.24	585	529.0	589.9	18.84	0.12
486	500.5	560.9	17.94	0.03	536	528.7	573.9	18.52	-0.13	586	478.2	590.0	18.23	0.02
487	536.0	561.0	16.70	-0.04	537	458.4	574.0	18.87	0.18	587	583.6	590.0	15.73	1.54
488	446.7	562.2	18.14	0.09	538	548.6	574.1	19.24	-0.10	588	522.7	590.6	18.99	0.01
489	559.7	562.3	14.58	1.70	539	486.9	574.4	19.00	0.15	589	514.0	590.9	19.05	0.06
490	512.3	562.6	18.16	0.11	540	521.7	574.5	18.58	-0.53	590	539.9	591.2	17.50	-0.07
491	588.0	562.7	17.81	0.02	541	535.9	574.6	18.29	-0.13	591	576.7	591.3	19.01	-0.09
492	533.0	562.8	17.98	0.08	542	493.2	574.9	19.36	0.10	592	489.2	591.3	15.50	1.11
493	480.6	563.1	18.37	-0.03	543	454.5	575.4	18.41	0.02	593	509.4	591.5	18.40	0.08
494	502.5	563.2	18.03	0.08	544	477.4	575.5	19.53	-0.15	594	553.8	592.3	17.77	-0.04
495	443.8	563.6	17.23	-0.07	545	573.3	575.5	17.72	0.02	595	517.3	592.7	18.32	-0.01
496	542.5	563.8	16.15	1.48	546	553.6	575.6	16.27	0.92	596	504.4	592.7	18.14	-0.01
497	551.4	564.0	15.18	0.39	547	543.0	576.6	18.14	-0.03	597	570.4	593.1	14.85	0.17
498	530.6	564.0	16.07	0.02	548	497.2	577.2	18.31	0.21	598	477.3	593.5	16.78	0.07
499	606.1	564.0	17.81	0.31	549	546.6	577.6	17.27	0.03	599	486.6	593.8	16.75	1.70
500	508.9	564.2	17.17	-0.02	550	463.3	577.9	18.75	0.56	600	583.1	594.1	15.29	1.14

Table 4.1 (cont.)

BV Photometry

ID	X	Y	V	B-V	ID	X	Y	V	B-V	ID	X	Y	V	B-V
601	473.9	594.3	17.55	0.09	616	566.0	598.7	19.08	-0.36	631	518.5	604.1	19.30	0.49
602	471.3	594.5	17.59	0.01	617	479.5	599.1	18.99	0.24	632	509.2	604.3	16.61	0.05
603	509.7	594.7	17.49	0.12	618	539.2	599.1	18.05	0.12	633	525.5	604.9	18.08	0.03
604	498.9	594.8	17.65	0.28	619	529.0	599.4	18.00	0.17	634	484.8	605.1	16.65	-0.04
605	555.9	595.1	17.52	-0.03	620	542.3	599.6	18.43	0.11	635	499.6	605.4	14.69	0.39
606	546.7	595.4	18.71	0.04	621	559.2	599.6	15.51	0.28	636	492.9	606.0	17.60	0.05
607	519.1	595.5	18.01	-0.05	622	473.7	599.7	17.63	0.01	637	540.7	606.0	18.26	-0.04
608	552.3	595.7	17.67	0.12	623	514.1	600.1	18.34	0.09	638	553.8	606.3	17.18	0.01
609	532.4	596.1	18.60	0.03	624	485.8	601.7	17.69	1.15	639	485.3	607.3	17.06	0.12
610	508.5	596.3	17.93	0.09	625	496.6	602.0	16.64	0.14	640	512.4	607.7	18.30	-0.06
611	564.2	597.0	18.48	-0.04	626	477.4	602.3	16.82	0.66	641	504.8	610.1	17.95	0.10
612	492.4	597.1	15.86	1.27	627	475.6	602.5	17.15	0.10	642	528.8	612.0	18.30	1.04
613	483.0	597.1	18.22	0.05	628	491.8	602.7	18.27	-0.14	643	534.9	614.7	18.06	-0.10
614	486.4	597.9	18.39	0.54	629	482.0	603.0	18.59	0.16					
615	500.9	598.5	19.30	-0.01	630	494.3	603.9	17.67	0.02					

4.9 shows population-synthesis Monte Carlo simulations based on the two different isochrones with an assumed photometric scatter of 0.05 mag and a mass function slope of 1.0 (see equation 4.15). One feature is immediately apparent in both cases, the lack of stars in the Hertzsprung gap compared to the observed data. Accepting the correctness of the models, there are at least three possible explanations for this effect: 1) The presence of young LMC field stars (and possibly a few stars from the young subcluster), 2) Binaries and close superpositions that were measured as single stars and 3) A possible time span for the initial star formation (this would need to be at least half the cluster age). We feel the first two effects are the likeliest and a close superposition of stars has been invoked by Welch & Stetson (1993) to explain the anomalously small luminosity amplitude and high brightness of three cepheids in the crowded regions of the young LMC cluster NGC 1866. Another feature is that the evolution slows down around the red giant branch (RGB) and at the blue end of the horizontal branch (HB) causing stars to build up in these regions. This is observed and we conclude that the stars are more metal-poor than $z = 0.008$ based
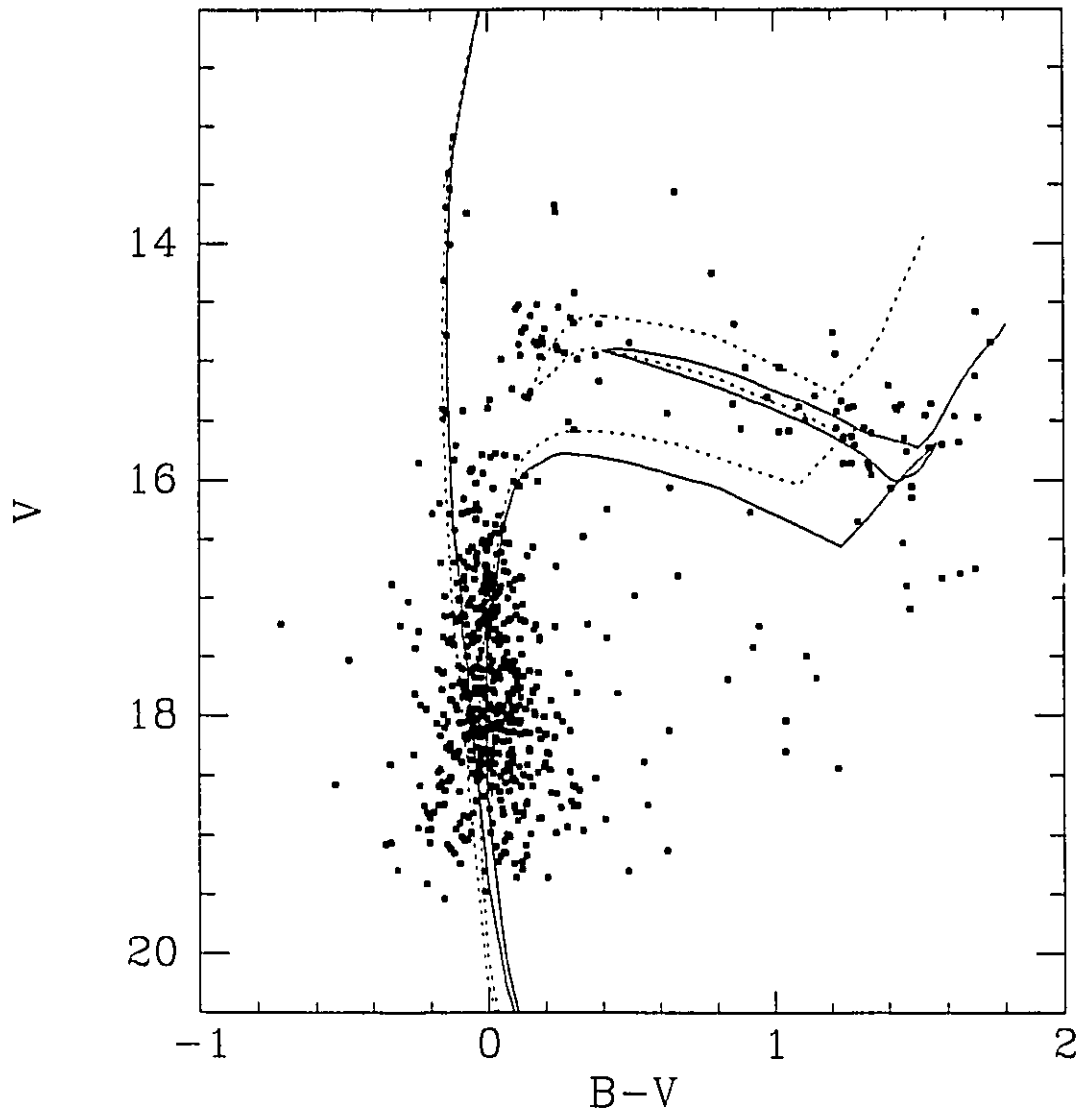
Fig. 4.8 - BV color-magnitude diagram for the region within 1' of the center of the main cluster. The solid lines correspond to the isochrones with z = 0.008 while the broken lines have z = 0.001. Both sets of isochrones have ages of τ = 6 Myr and τ = 90 Myr, as well as $(m-M)_0$ = 18.5 and E(B-V) = 0.17 mag.

on a synthetic HB which does not extend far enough to the blue and a synthetic
RGB which appears to be too red. The z = 0.001 isochrone appears to have too blue
a RGB although it does provide a reasonable fit at the blue end of HB. Therefore,
the metallicity lies between z=0.008 and z=0.001 but this conclusion is dependent
on the adopted reddening and distance modulus.

Previous age estimates are $\tau = 40 \pm 10$ Myr (Hodge 1983, based on data from
Tifft & Connoly 1973, and Robertson 1974), $\tau = 21 \pm 5$ Myr (Alcaino & Liller
1987) and $\tau = 40 \; ^{+50}_{-10}$ (Lee 1991). We have shown that the the Alcaino & Liller
photometry and reddening estimate are both close to our own and therefore the
different age estimates can be attributed to the different isochrones (they used
the isochrones of Maeder & Mermilliod 1981) and the different age-determination
techniques. Unfortunately, the photometry of Lee was not available for comparison.

Finally, we examined stars in the region of H88-159. Unfortunately, there are
no stars in this region as bright as the turn-off for the main cluster. Therefore, it is
impossible to derive an accurate age for this subcluster in order to determine if it is,
in fact, a distinct population from the main cluster as indicated from the integrated
photometry of Bica et al. (1992). An argument against it being distinct as opposed
to being a tidal tail is that it appears to continue outward from the main cluster in
a fairly straight line for about 2 arcmin (see Fig. 4.1).

4.2.3   Surface Photometry

Clearly, the presence of the above described sub-clustering coupled with the
large number of LMC field stars located near NGC 1850 is going to complicate
attempts to obtain reliable surface photometry. Thus, it is advantageous to remove
the luminosity contribution of any definite cluster non-members. DoPHOT was
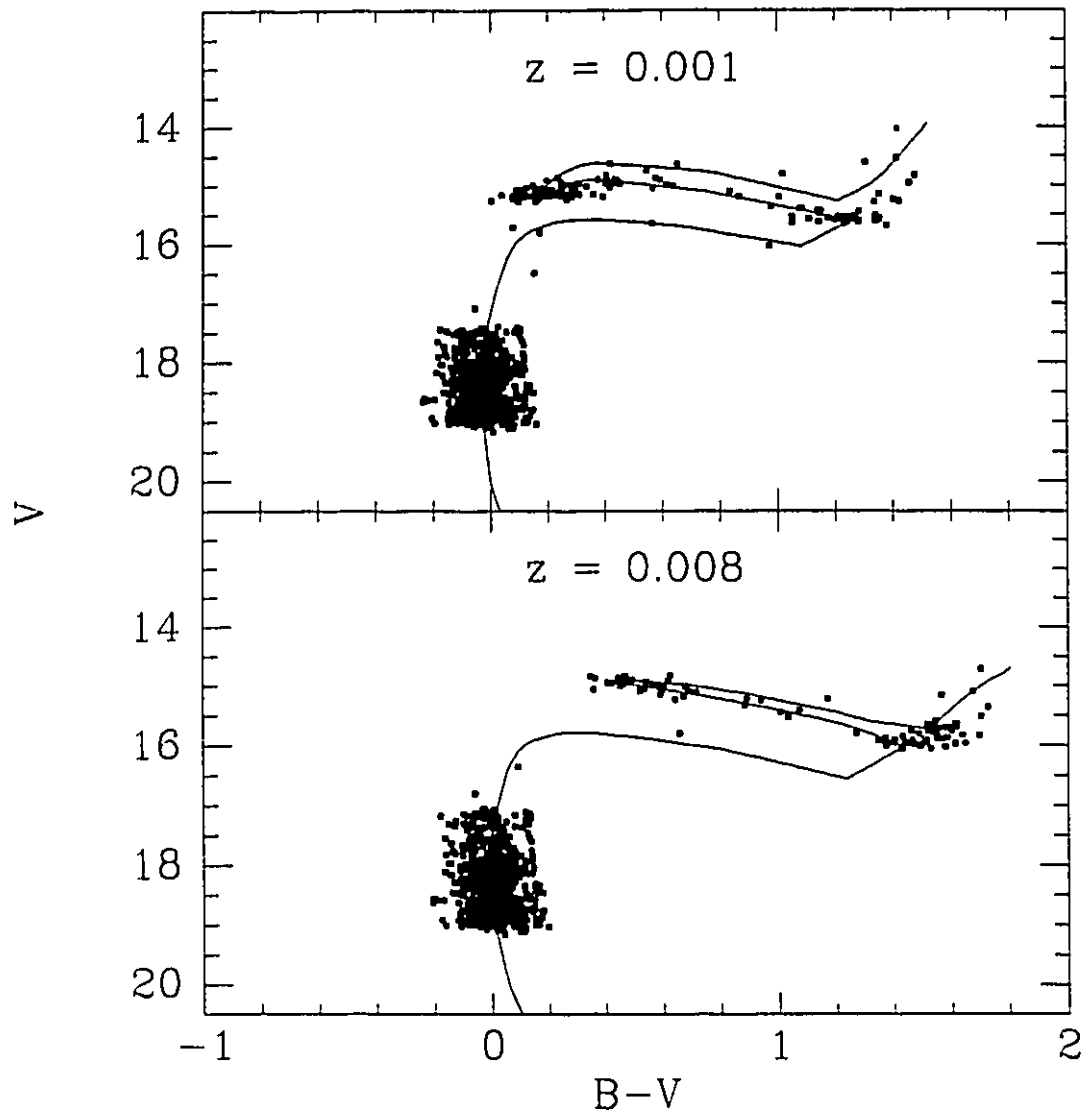
Fig. 4.9 - Population synthesis Monte Carlo experiments for the z = 0.008 and z = 0.001 isochrones described in the previous figure. A photometric uncertainty of 0.05 mag has been added.

used to remove the stars in regions 1 and 3 (see Fig. 4.6) from both the B and V frames.

It is also favorable to determine the cluster ellipticity so that correspondingly elliptical apertures can then be used to perform the surface photometry. This is a difficult task for most globular clusters and particularly so for NGC 1850. In common with other clusters, NGC 1850 consists of resolved stars, but in this case the stars dominating the light are young supergiants. As well, there is the presence of the young binary companion. Fig. 4.10 shows a contour plot of the B and V star-subtracted, median filtered (filter radius of 9″) images (solid lines). Superimposed on the contours are ellipses produced by the ELLIPSE task in the IRAF[1] STSDAS package which uses the ellipse fitting technique of Jedrzejewski (1987). Three things are immediately clear: 1) The ellipses do not provide a good model for the smoothed NGC 1850 light distribution, 2) the elliptical parameters change rapidly as a function of radius, and 3) there is rather poor agreement between the two different bandpasses. This leads us to believe that the ellipticities which we are measuring probably result from the presence of a number of bright stars which could not be adequately subtracted due to the extreme crowding. They are, therefore, not a good representation of the shape of the underlying mass distribution and hence, lacking anything better, we use circular contours to perform the surface photometry. We cannot, however, rule out the possibility that NGC 1850 is significantly elliptical. The use of circular apertures in such a case does not tend to result in systematic errors in the surface photometry, but does increase the photometric scatter (i.e., see Fischer *et al.* 1992b).

---

[1] IRAF is distributed by the National Optical Astronomy Observatories, which is operated by the Association of Universities for Research in Astronomy, Inc., under contract to the National Science Foundation.
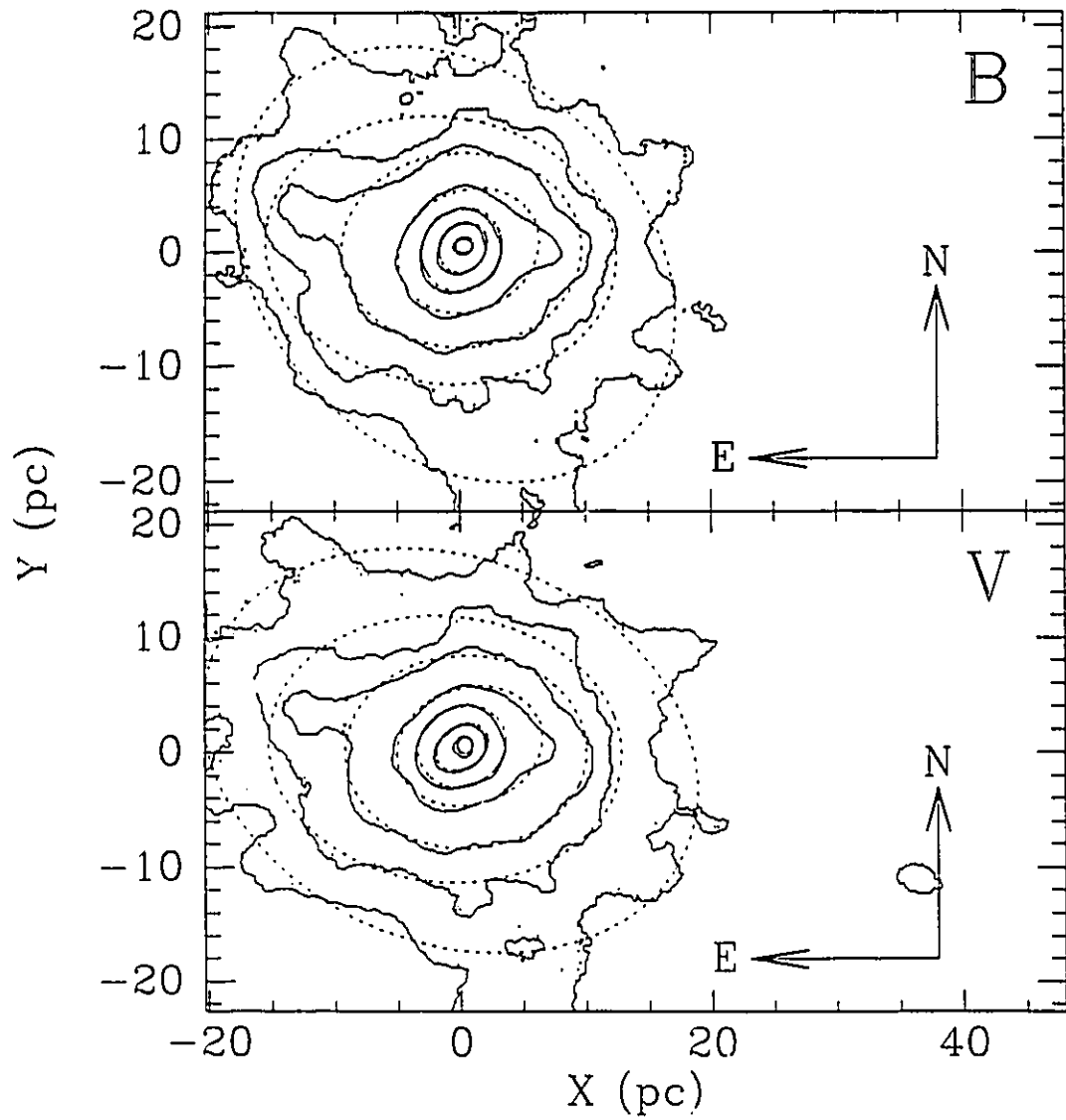
Fig. 4.10 - Contour plot of star-subtracted, median-filtered BV images of NGC 1850. The solid lines are isophotes while the dashed lines are the best-fit ellipses.

The cluster center was found using a multi-step procedure. The first step was to estimate the position of the center using the isophotes produced above. Surface photometry was then obtained utilizing this cluster center. A King model (see §4.2.4) was fit to the surface photometry and a new image was made with the fitted King parameters but with a smooth light distribution. We then cross correlated the artificial image with the original image to obtain small residual X and Y shifts. The final centers were within 2 arcsec of the original guesses.

Surface photometry was performed in a manner similar to Djorgovski (1988). The frames were broken up into a series of concentric circular annuli centered on the cluster. The annuli were further divided into eight azimuthal sectors. The average pixel brightness was determined for each sector in a given annulus and the *median* of the eight separate measurements was taken as the representative brightness at the area-weighted average projected radius of the annulus (i.e., the mean radius of all the pixels within the annulus which is approximately equal to the geometric mean). The standard error of the median of the eight sectors was adopted as the photometric uncertainty. Using the median as opposed to the more commonly adopted mean is essential in the case of NGC 1850 as it reduces the contamination due to the bright supergiants and the binary companion.

A background level (a combination of sky light and Galactic foreground and remaining LMC field stars) was estimated from regions at large projected distances from the cluster. We found that the surface brightness profiles tended to level out beyond 45 pc (we have adopted a distance to the cluster of 50 kpc) for both the B and V frames. By "levelling out" we don't necessarily mean that the cluster light does not extend beyond this point but simply that fluctuations in the background dominate to such an extent that it is no longer possible to observe the profile declining in intensity. Therefore, it was this region with a projected radius of 45

$\leq$ R (pc) $\leq$ 100 that was used for the background determinations. The reddening-corrected background values for the B and V frames were, respectively, 1370 $\pm$ 27 $L_{B\odot}$ pc^{-2} and 682 $\pm$ 14 $L_{V\odot}$ pc^{-2}.

The background-subtracted surface photometry data is presented in Table 4.2 [assuming a cluster distance of 50 kpc, $M_{V\odot}$ = 4.83 and (B-V)$_\odot$ = 0.65, Mihalas and Binney 1981, p. 60]. Columns 1 and 3 are the projected area-weighted radii, and columns 2 and 4 are the B and V luminosity densities, respectively.

Table 4.2
Surface Photometry

R (pc)	L_B ($L_{B\odot}$ pc^{-2})	R (pc)	L_V ($L_{V\odot}$ pc^{-2})
0.3	26246.0 $\pm$ 3517.0	0.3	14938.0 $\pm$ 1958.0
0.5	25094.0 $\pm$ 3993.0	0.5	9719.0 $\pm$ 1844.0
0.7	24901.0 $\pm$ 3821.0	0.7	10536.0 $\pm$ 2155.0
0.8	31223.0 $\pm$ 5737.0	0.8	12438.0 $\pm$ 3273.0
1.1	26021.0 $\pm$ 6693.0	1.0	11899.0 $\pm$ 3994.0
1.3	22898.0 $\pm$ 4908.0	1.3	11771.0 $\pm$ 2702.0
1.7	19512.0 $\pm$ 4085.0	1.7	10236.0 $\pm$ 2041.0
2.1	14890.0 $\pm$ 3159.0	2.1	6037.0 $\pm$ 1010.0
2.6	11276.0 $\pm$ 1308.0	2.7	5831.0 $\pm$ 988.0
3.3	10828.0 $\pm$ 1290.0	3.3	5357.0 $\pm$ 554.0
4.2	6910.0 $\pm$ 1417.0	4.2	3517.0 $\pm$ 733.0
5.3	3889.0 $\pm$ 938.0	5.3	2098.0 $\pm$ 443.0
6.6	3198.0 $\pm$ 435.0	6.6	1625.0 $\pm$ 261.0
8.4	2919.0 $\pm$ 429.0	8.4	1423.0 $\pm$ 199.0
10.5	1044.0 $\pm$ 210.0	10.5	510.0 $\pm$ 88.0
13.2	944.0 $\pm$ 201.0	13.2	423.0 $\pm$ 101.0
16.7	414.0 $\pm$ 144.0	16.7	233.0 $\pm$ 68.0
21.0	360.0 $\pm$ 63.0	21.0	170.0 $\pm$ 29.0
26.4	140.0 $\pm$ 44.0	26.4	64.0 $\pm$ 23.0
33.1	92.0 $\pm$ 39.0	33.1	46.0 $\pm$ 20.0
40.5	22.0 $\pm$ 28.0	40.5	8.0 $\pm$ 17.0

Fig. 4.11 is a plot of the B and V surface brightness profiles. Also shown are typical stellar profiles which have a FWHM less than 15% of the cluster core

radius (see §4.2.4); hence seeing will have a negligible effect on measurements of this quantity (Mihalas and Binney 1981, p. 315).

4.2.4   King-Michie Models

We fit projected single-component King-Michie (KM) models (King 1966 and Michie 1963) to the surface photometry data. These models have an energy (E) angular momentum (J) per unit mass distribution function given by

$$f(E = -0.5v^2 + W, J) \propto e^{-[J/(2v_s r_a)]^2}(e^{-0.5v^2 + W} - 1), \tag{4.1}$$

where v_s is the scale velocity, r_a is the anisotropy radius (both described below), and W is the reduced gravitational potential. The shape of the density distribution, $\rho_K(r)$, is determined by solving Poisson's equation and is dependent on two parameters; the central potential W_o, and r_a, beyond which stellar orbits become increasingly radial. Scaling is applied in both the radial (r_s) and luminosity (ρ_{Ko}) dimensions to give the best fit. For a complete description of the models (albeit for the more complex multi-component case) the reader is directed to Gunn and Griffin (1979). Model density profiles with r_a values ranging from 3 r_s to infinity (i.e., an isotropic distribution function) were generated, and projected on to the observational plane. These were binned identically to the observed data and fit using a maximum likelihood technique.

Tables 4.3 and 4.4 show, for each r_a, the best *fitted* KM parameters for both bandpasses. Column 1 contains r_a, column 2 is the reduced central potential, column 3 is r_s and column 4 is c $= r_s/r_t$ (r_t is the tidal radius). Column 5 is the reduced chi-square ($\chi_\nu^2 = \chi^2/\nu$, where $\nu = 18$ is the number of degrees of freedom) for the fit. Column 6 is the probability of obtaining a value greater than χ_ν^2 for a model with the given parameters and the uncertainties listed in Table 4.2. These were derived from 1000 simulations of the surface photometry data per
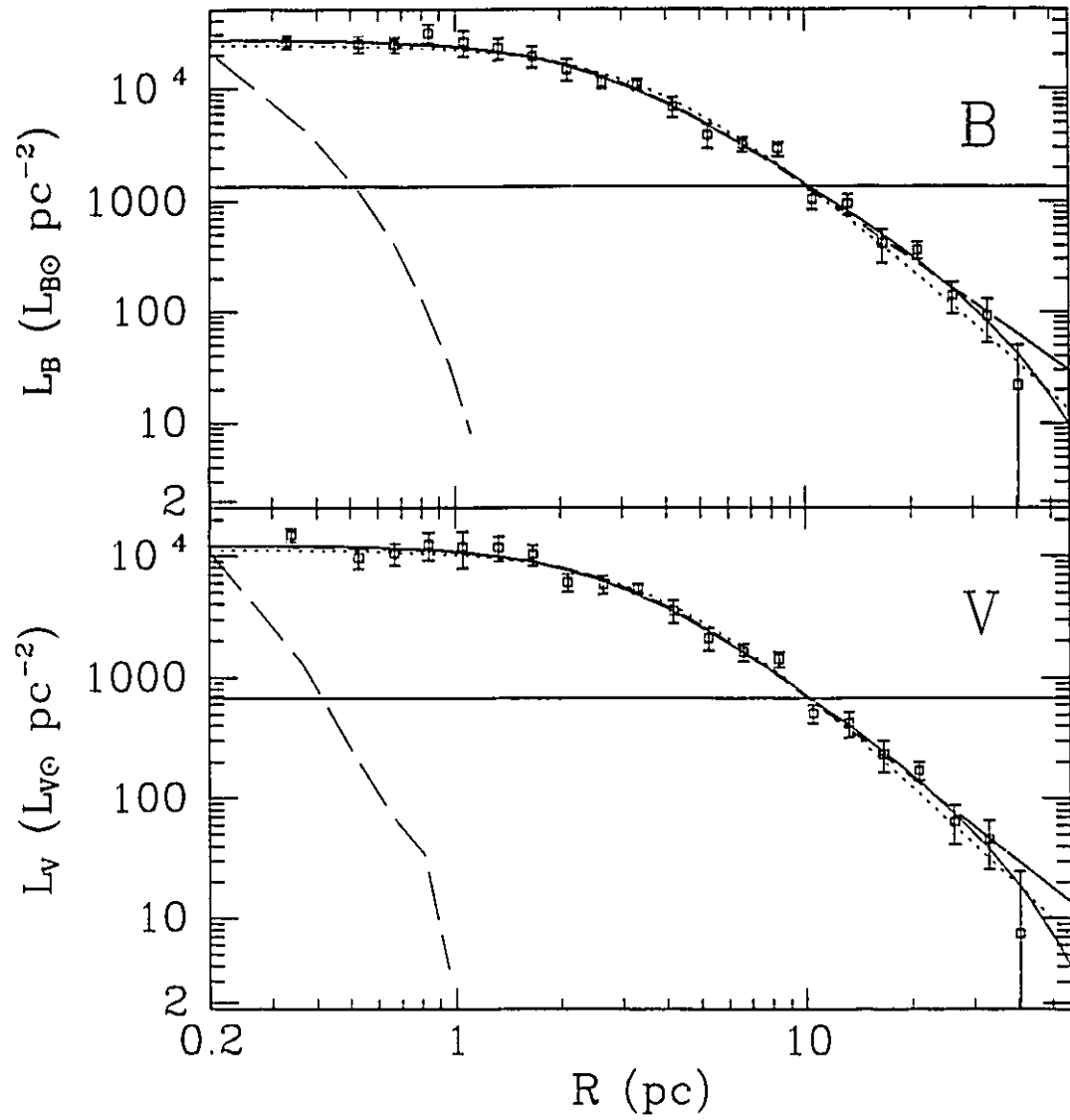
Fig. 4.11 - B and V surface brightness profiles. The long-dashed lines are typical stellar profiles. The solid and short-dashed lines are isotropic and $r_a = 3r_s$ single-mass King-Michie surface density models, respectively.

model. Each simulation used a surface profile generated from the best fit model with errors, drawn from the uncertainties shown in Table 4.2. The same fitting procedure originally applied to the real data was utilized and, in this way, we found the uncertainties in each fitted parameter as well as the distribution of χ_ν^2 . The remaining columns of Tables 4.3 and 4.4 will be discussed in §4.4.1. The fitted KM model parameters were consistent for the two bandpasses.

Tables 4.5 and 4.6 have a summary of the *derived* KM parameters for both bandpasses corresponding to the models specified in Tables 4.3 and 4.4. Column 1 is the anisotropy radius while column 2 is the central luminosity density, ρ_{K_0}. Column 3 is the cluster luminosity and columns 4 and 5 will be discussed in §4.4.1.

The solid lines in Fig. 4.11 show the best fit models which are those possessing isotropic orbits. The quality of the fits deteriorates as r_a decreases. Interestingly, this is quite different from what was seen in the case of the slightly older LMC cluster NGC 1866 which favored highly anisotropic (i.e. $r_a = 3\ r_s$) KM models and appeared to have a halo of unbound stars (Fischer *et al.* 1992a). Also shown as dotted lines in the same figure are the $r_a = 3\ r_s$ models. It is unclear whether or not the data exhibit a tidal cut-off. In fact, using a profile that extends out to about 20 pc, Elson (1991) finds no evidence for truncation. Our profile extends to about twice that radius and there is, at best, a small indication for truncation. To test the hypothesis that there is significant truncation we have fit models of the form:

$$\mu(R) = \mu_0[1 + (R/a)^2]^{-\gamma/2}, \qquad (4.2)$$

to the surface brightness profile using a non-linear, weighted, least squares technique. The best-fit parameters for these untruncated power-law models are: $\mu_{B_0} = 26800. \pm 2000.\ L_{B\odot}\ pc^{-2}$, $a_B = 2.8 \pm 0.3$ pc, $\gamma_B = 2.26 \pm 15$, $\mu_{V_0} = 12000. \pm 900.\ L_{V\odot}\ pc^{-2}$, $a_V = 3.1 \pm 0.4$ pc, $\gamma_V = 2.34 \pm 0.15$. The χ_ν^2 are 0.89 $[P(> \chi_\nu^2) = 0.59]$

Table 4.3
King-Michie - B Band Fitted Parameters

r_a (r_s)	Photometry					Velocities		
	W_o	r_s (pc)	c	χ^2_ν ($\nu=18$)	$P(>\chi^2_\nu)$	v_s (km s^{-1})	ζ^2	$P(|\zeta^2-N|)$
ISO	7.3 ± 0.30	2.6 ± 0.20	$42. \pm 8.$	0.68	0.81	2.2 ± 0.4	37.61	0.42
20	7.3 ± 0.30	2.6 ± 0.20	$46.\ ^{+12.}_{-9.}$	0.69	0.80	2.2 ± 0.4	37.66	0.42
10	7.3 ± 0.35	2.6 ± 0.15	$67.\ ^{+45.}_{-25.}$	0.72	0.76	2.2 ± 0.4	37.80	0.40
5	$6.8\ ^{+0.10}_{-0.20}$	3.1 ± 0.15	$125. \pm 50.$	0.86	0.60	2.2 ± 0.5	38.40	0.30
3	$5.9\ ^{+0.05}_{-0.10}$	3.5 ± 0.20	$122. \pm 45.$	1.17	0.25	2.3 ± 0.5	39.11	0.20

Table 4.4
King-Michie - V Band Fitted Parameters

r_a (r_s)	W_o	Photometry				Velocities		
		r_s (pc)	c	χ^2_L ($\nu = 18$)	$P(>\chi^2_L)$	v_s (km s^{-1})	ζ^2	$P(|\zeta^2 - N|)$
ISO	7.1 ± 0.30	2.7 ± 0.20	$37. \pm 8.$	0.91	0.51	2.2 ± 0.4	37.68	0.42
20	7.1 ± 0.30	2.8 ± 0.20	$39. \begin{smallmatrix}+11.\\-9.\end{smallmatrix}$	0.91	0.51	2.2 ± 0.4	37.72	0.40
10	7.1 ± 0.35	2.8 ± 0.20	$51. \begin{smallmatrix}+33.\\-16.\end{smallmatrix}$	0.92	0.50	2.2 ± 0.4	37.84	0.38
5	$6.8 \begin{smallmatrix}+0.10\\-0.20\end{smallmatrix}$	3.2 ± 0.20	$116. \pm 47.$	0.98	0.43	2.2 ± 0.5	38.31	0.30
3	$5.9 \begin{smallmatrix}+0.05\\-0.10\end{smallmatrix}$	3.7 ± 0.20	$122. \pm 44.$	1.16	0.25	2.3 ± 0.5	38.97	0.22

Table 4.5
King-Michie - B Band Derived Parameters

r_a (r_s)	ρ_{KBo} $(L_{B\odot}\ pc^{-3})$	L_B $(10^6 L_{B\odot})$	Mass $(10^4 M_\odot)$	M/L_B $(M_\odot/L_{B\odot})$
ISO	5500. ± 700.	2.60 ± 0.20	5.7 ±2.3	0.02 ±0.01
20	5500. ± 700.	2.64 ± 0.20	5.7 ±2.3	0.02 ±0.01
10	5400. ± 700.	2.75 ± 0.30	5.9 ±2.4	0.02 ±0.01
5	4200. ± 550.	2.75 ± 0.20	5.8 ±2.3	0.02 ±0.01
3	3700. ± 500.	2.62 ± 0.20	5.4 ±2.2	0.02 ±0.01

Table 4.6
King-Michie - V Band Derived Parameters

r_a (r_s)	ρ_{KVo} $(L_{V\odot}\ pc^{-3})$	L_V $(10^6 L_{V\odot})$	Mass $(10^4 M_\odot)$	M/L_V $(M_\odot/L_{V\odot})$
ISO	2300. ± 350.	1.26 ± 0.10	5.7 ±2.3	0.05 ±0.02
20	2300. ± 350.	1.27 ± 0.10	5.7 ±2.3	0.04 ±0.02
10	2300. ± 300.	1.31 ± 0.15	5.8 ±2.3	0.04 ±0.02
5	1900. ± 250.	1.37 ± 0.10	5.9 ±2.4	0.04 ±0.02
3	1600. ± 200.	1.32 ± 0.10	5.6 ±2.2	0.04 ±0.02

and 1.06 $[P(> \chi^2_\nu) = 0.39]$ for the B and V profiles, respectively, which are higher than all but the $r_a = 3\ r_s$ KM models. We conclude that the best truncated models provide marginally better agreement with the surface photometry data.

4.3   RADIAL VELOCITIES

4.3.1   Observations and Reductions

Spectra of 52 supergiants in the region surrounding NGC 1850 were obtained during two runs (1991 February 14-20 and 1991 December 14-17) using the photon-counting echelle spectrograph on the 2.5m Dupont reflector, designed and built by Steve Shectman. Eight of the stars have repeat measurements.

The observation and reduction procedures for a previous run at LCO have been discussed extensively in Welch *et al.* (1991) and remain largely unchanged for this data. Briefly, the observing procedure consisted of exposures with integration times

of 200 - 500s and Th-Ar arcs approximately every 45 minutes. A representative LCO spectrum is shown in Fig. 2 of Côté *et al.* (1991). The reduction utilizes the IRAF ECHELLE and RV packages (Tody 1986) to obtain both velocities and velocity uncertainties. The velocity zero-point is tied to the IAU velocity standard 33 Sex as described in Fischer *et al.* 1992a and is believed to be accurate to better than 2 km s^{-1}.

Along with the program stars, relatively high S/N spectra were obtained on each night for both a nearby bright star used as a local velocity standard (LVS) for differential measurements and the radial velocity standard HD 23214 to examine the possibility of velocity zero-point drifts and to test the accuracy of the velocity uncertainties returned by RVXCOR. These velocities are shown in Table 4.7 for the eight separate nights over the two observing runs in which NGC 1850 stars were observed. Column 1 is the Heliocentric Julian Date minus 2448000, column 2 is the radial velocity, column 3 is the mean velocity for the given observing run and column 4 is the reduced chi squared for the appropriate observing run. Within the RVXCOR produced uncertainties, there is no significant zero-point drift during the individual runs. There is, however, a discrepancy between the mean velocities for the LVS for the two separate observing runs at the 4.6σ level implying either that the radial velocity zero-point has shifted or that this star has a variable velocity. The shift is not seen in HD 23214 implying the latter hypothesis is probably correct. Olszewski *et al.* (1991) have obtained 9 lower resolution radial velocity measurements for HD 23214 during two observing runs, 1987 January 8-12 and 1987 December 27-31, deriving a mean velocity of -4.3 ± 1.8 km s^{-1}. They also present a single CORAVEL velocity determination of -4.7 ± 0.3 km s^{-1} for HJD = 2446862.51. This latter deviates by 5.6σ from our value of -2.8 ± 0.2 km s^{-1}, which, as mentioned above, is based upon the IAU radial velocity standard 33 Sex. Another radial velocity

standard, HD 196983, has been measured at two epochs, HJD − 2448000 = 606.5225
and 608.5179 yielding v_x = -9.6 ± 0.5 km s^{-1} and -8.7 ± 0.6 km s^{-1}, respectively,
for a mean of -9.2 ± 0.4 km s^{-1}. This agrees very well with the CORAVEL value,
based on 10 separate measurements spanning 715 days starting in September 1981,
of -9.3 ± 0.1 km s^{-1} (Maurice et al. 1984). To conclude, we feel that our velocity
zero-point is uncertain at about the 2.0 km s^{-1} but that there is no significant
zero-point drift during the two runs. (This latter possibility will be examined in
more detail presently.)

The radial velocity data for the cluster stars are presented in Table 4.8. Column
1 contains the stellar identifications (these do not correspond to the ID's in Table
4.1), column 2 has the projected radii, column 3 the equinox J2000.0 position angles,
column 4 contains the radial velocities and column 5 contains the mean velocities
for stars with repeated measurements. Column 6 is the Heliocentric Julian Date −
2448000 for the velocity measurements. Columns 7 and 8 are V and B−V for the
stars. The photometry in the innermost regions is relatively uncertain due to the
high degree of crowding. Fig. 4.12 is a finder chart for all but the star farthest from
the cluster center.

Of the eight stars with repeated velocity measurements, six had individual χ^2
of less than 2.85 for a total χ^2 = 6.44 for 5 degrees of freedom. Of the other two,
one had χ^2 = 7.9 (star RV 49) and the other had χ^2 = 217 (star RV 19). If the
velocity shift indicated by the LVS is applied these χ^2 values all decrease; we get a
total χ^2 = 4.33 for the six stars and 3.40 and 217.00 for the other two stars. This
is an argument in favor of adoption of the velocity shift.

From their colors, the two high-χ^2 stars are evolved and their velocities indicate
that they are in the LMC. Star RV49 appears to be an LMC field star, perhaps
a binary. Star RV19, as indicated by its radial velocities, is clearly a member of

Table 4.7
Velocity Standards

HJD (−2448000)	v_x (km s^{-1})	$\langle v_x \rangle$ (km s^{-1})	χ_ν^2
	Local		
304.5946	34.5 ± 0.3	34.2 ± 0.1	1.12
305.5481	34.3 ± 0.3		
306.5467	33.7 ± 0.3		
307.5481	34.4 ± 0.2		
308.5432	34.0 ± 0.3		
605.7090	36.0 ± 0.6	35.7 ± 0.3	0.72
606.6605	36.0 ± 0.6		
607.6073	35.0 ± 0.6		
608.6622	35.7 ± 0.6		
	HD 23214		
305.5204	-2.6 ± 0.4	-2.9 ± 0.2	0.26
306.5211	-2.9 ± 0.4		
307.5189	-3.0 ± 0.4		
308.5182	-3.1 ± 0.4		
605.5891	-3.1 ± 0.5	-2.8 ± 0.2	0.32
605.6899	-2.8 ± 0.6		
606.5868	-2.9 ± 0.6		
607.5920	-2.4 ± 0.5		
608.5895	-2.7 ± 0.5		

the LMC. Further, its luminosity (V = 13.54) indicates that it is a supergiant. Two possibilities are that the star is a binary or a Cepheid. The two velocity measurements differ by over 30 km s^{-1} which argues against the former hypothesis as it would require a very favorable inclination coupled with fortuitous observations. The star's color (B − V = 0.65) makes it an excellent Cepheid candidate, and it is likely to be a cluster member based on its proximity to the cluster center (R = 3.8 pc). Neither of these two stars will be used in the cluster mass determinations.

Table 4.8
Radial Velocities

ID	R (pc)	Θ (°)	v_x (km s^{-1})	$\langle v_x \rangle$ (km s^{-1})	HJD (−2448000)	V (mag)	B–V (mag)
RV1	0.0	18.5	252.7 ± 2.1	252.7 ± 2.1	608.6797	15.74	0.58
RV2	0.5	166.7	248.3 ± 1.3	248.3 ± 1.3	608.6768	14.89	0.20
RV3	0.9	224.6	248.4 ± 1.9	248.4 ± 1.9	304.5439	14.69	0.86
RV4	1.0	163.4	251.8 ± 2.6	251.8 ± 2.6	608.6729	15.44	0.67
RV5	1.1	325.4	248.4 ± 4.9	248.4 ± 4.9	303.5889	14.04	0.06
RV6	1.3	200.3	249.8 ± 3.3	249.8 ± 3.3	303.6309	14.68	0.14
RV7	1.5	71.1	252.2 ± 1.9	252.2 ± 1.9	303.5547	14.30	-0.19
RV8	1.7	349.2	260.2 ± 4.3	260.2 ± 4.3	304.5420	14.54	0.14
RV9	1.7	102.0	254.3 ± 1.7	252.3 ± 1.1	607.6504	14.23	0.68
			251.0 ± 1.4		608.6973		
RV10	2.4	321.1	257.4 ± 3.0	257.4 ± 3.0	306.5625	14.72	0.13
RV11	2.7	134.0	276.0 ± 2.8	276.0 ± 2.8	303.5850	14.53	0.18
RV12	2.8	110.9	250.3 ± 1.1	250.1 ± 0.8	607.6543	15.39	1.40
			249.9 ± 1.2		608.7061		
RV13	2.8	340.9	254.6 ± 1.3	254.6 ± 1.3	608.6816	15.14	0.60
RV14	3.0	67.9	253.1 ± 2.2	253.1 ± 2.2	608.6943	15.56	1.30
RV15	3.0	236.9	246.7 ± 1.6	246.7 ± 1.6	607.6572	15.37	0.04
RV16	3.1	76.5	248.5 ± 2.2	248.5 ± 2.2	304.5586	14.74	0.42
RV17	3.3	218.8	243.4 ± 3.1	243.4 ± 3.1	304.5479	14.73	0.13
RV18	3.6	315.3	234.4 ± 2.4	234.4 ± 2.4	306.5605	15.05	0.93
RV19	3.8	341.1	272.7 ± 1.3	260.7 ± 1.0	303.5586	13.54	0.65
RV19			240.9 ± 1.7		607.6416		
RV20	4.0	39.9	253.6 ± 1.3	253.2 ± 0.9	608.6885	15.70	1.56
			252.9 ± 1.2		605.7393		
RV21	4.1	84.4	256.7 ± 1.4	256.7 ± 1.4	605.7344	15.19	1.62
RV22	4.2	137.2	247.7 ± 1.7	247.7 ± 1.7	306.5576	14.55	0.23
RV23	4.6	147.9	258.7 ± 3.4	258.7 ± 3.4	303.5752	14.82	0.16
RV24	4.6	252.5	253.0 ± 2.0	250.1 ± 1.0	304.5547	14.71	0.21
			249.1 ± 1.2		608.6689		
RV25	4.7	0.1	242.4 ± 2.9	242.4 ± 2.9	307.5625	14.85	0.15
RV26	5.0	247.4	242.3 ± 2.9	242.3 ± 2.9	304.5518	14.25	0.77
RV27	5.1	57.9	248.3 ± 1.6	248.3 ± 1.6	608.6924	15.57	0.41
RV28	5.2	300.6	255.7 ± 2.1	255.7 ± 2.1	608.7168	15.55	0.86
RV29	5.2	3.4	250.5 ± 1.0	249.8 ± 0.7	608.6855	14.77	1.18
			249.2 ± 0.9		307.5654		
RV30	5.5	219.5	253.5 ± 1.5	253.5 ± 1.5	608.7139	15.40	1.23
RV31	6.0	351.4	252.2 ± 1.7	252.2 ± 1.7	606.6895	15.39	1.41
RV32	6.3	288.7	250.7 ± 2.0	250.7 ± 2.0	606.6836	15.42	1.19

Table 4.8 (cont.)
Radial Velocities

ID	R (pc)	Θ (°)	V_x (km s^{-1})	$\langle v_x \rangle$ (km s^{-1})	HJD (−2448000)	V (mag)	B–V (mag)
RV33	6.7	14.6	251.9 ± 1.3	251.9 ± 1.3	605.7305	15.70	1.53
RV34	6.9	9.4	251.9 ± 2.0	251.9 ± 2.0	605.7266	14.96	0.19
RV35	7.2	48.0	249.7 ± 1.5	249.7 ± 1.5	607.6465	14.94	1.19
RV36	7.7	198.9	250.9 ± 1.1	250.9 ± 1.1	605.7227	15.48	1.64
RV37	7.8	309.1	277.3 ± 3.9	277.3 ± 3.9	303.5625	13.67	-0.14
RV38	8.0	91.7	241.7 ± 1.6	241.7 ± 1.6	303.6201	14.67	0.29
RV39	8.2	67.0	233.5 ± 1.1 232.2 ± 2.0	233.2 ± 1.0	303.6152 607.6436	13.67	0.23
RV40	8.3	226.0	239.6 ± 3.8	239.6 ± 3.8	303.5508	13.73	0.22
RV41	8.3	12.0	252.5 ± 1.3	252.5 ± 1.3	608.7246	15.57	1.25
RV42	8.3	301.6	252.5 ± 2.0	252.5 ± 2.0	308.5596	14.64	0.29
RV43	8.7	132.5	249.1 ± 1.1	249.1 ± 1.1	607.6270	14.58	1.67
RV44	10.3	356.5	250.1 ± 1.7	250.1 ± 1.7	608.7207	15.65	1.21
RV45	10.6	161.5	250.7 ± 1.0	250.7 ± 1.0	605.7178	14.85	1.73
RV46	11.8	10.2	252.4 ± 1.5	252.4 ± 1.5	606.6943	15.13	1.66
RV47	13.7	80.2	249.6 ± 1.5	249.6 ± 1.5	305.5654	14.68	0.39
RV48	16.6	304.7	252.0 ± 1.2	252.0 ± 1.2	607.6318	15.19	1.55
RV49	18.3	120.6	288.6 ± 1.1 284.4 ± 1.0	286.3 ± 0.7	607.6240 308.5518	13.66	1.82
RV50	18.7	67.2	253.3 ± 1.9	253.3 ± 1.9	305.5586	14.54	0.49
RV51	19.4	332.6	246.4 ± 2.6	246.4 ± 2.6	607.6377	15.08	1.41
RV52	35.5	81.7	254.9 ± 1.0	254.9 ± 1.0	307.5576	14.59	1.71

In Fig. 4.13 we present plots of radial velocity and radial velocity uncertainty vs. stellar B–V. There are clearly trends towards both a larger apparent velocity dispersion and larger uncertainties for the bluer stars. The correlation between velocity uncertainty and apparent velocity dispersion is, of course, expected. The correlation between uncertainty and color has two causes: 1) the lack of lines in the bluer stars, and 2) spectral mismatch with the template star (a K giant). For the mass determinations of the next section we decided not to employ any stars with uncertainties greater than 2.7 km s^{-1} (the solid line in Fig. 4.13), eliminating 9 stars. We have also eliminated the three stars having $v_x > 270$ km s^{-1} as being
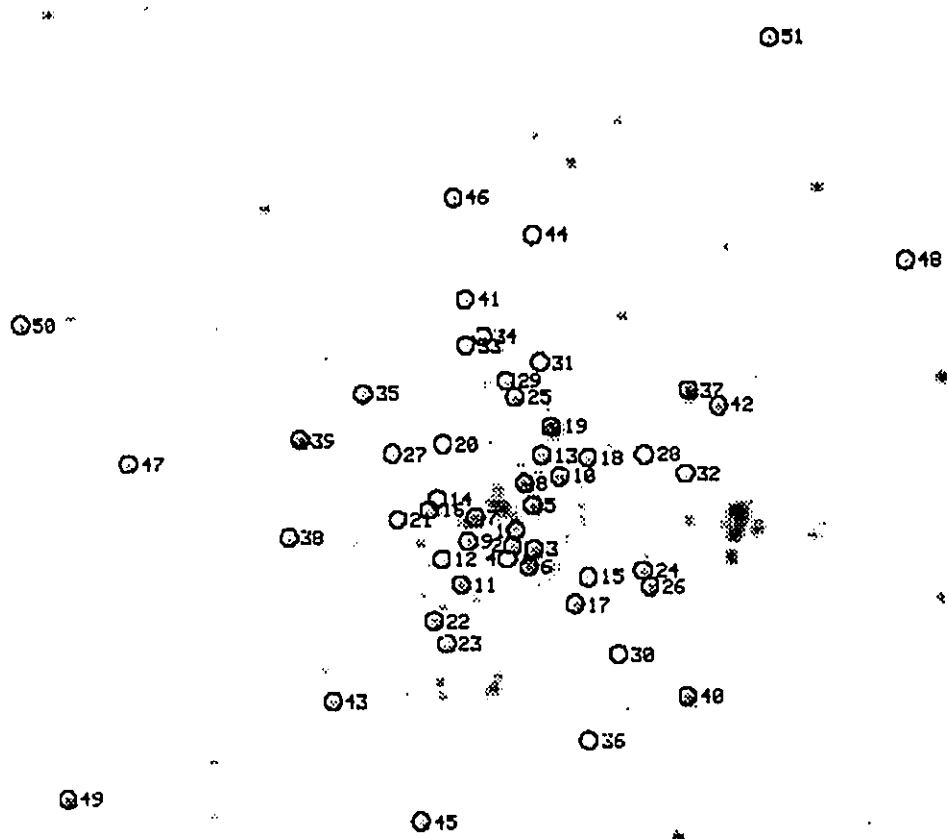
Fig. 4.12 - A finder chart for 51 of the 52 stars for which we have radial velocities.

probable non-members (or variables) and star RV 18, which was classified as a variable by Robertson (1974) and from its color is a probable cepheid, leaving a total of 38 stars.

4.4   MASS DETERMINATIONS

4.4.1   King-Michie Models

The mass of a multi-mass KM model is given by

$$M = \frac{9 r_s v_s^2}{4\pi G} \int \frac{\rho}{\rho_0} r^2 dr \qquad (4.3)$$

Illingworth (1976), where r_s is given in Tables 4.3 and 4.4, and v_s is the scale velocity. The run of $\sigma_r^2(r)$ and $\sigma_t^2(r)$ are determined from

$$\sigma_{r,t}^2(r) = \frac{\int_{|\sigma| \leq W(r)} f(\sigma, W) \sigma_k^2 d^3\vec{\sigma}}{\int_{|\sigma| \leq W(r)} f(\sigma, W) d^3\vec{\sigma}}, \qquad (4.4)$$

where W is the reduced potential (W = 0 at the tidal radius) and $\sigma_k = \sigma\cos\theta$ or $\sigma\sin\theta$ for σ_r or σ_t, respectively. Comparisons were made between the observed velocities and the model velocity dispersion projected along the line of sight,

$$\sigma_p^2(R) = \frac{2}{\mu(R)} \int_R^\infty \frac{\rho_K(r)[(r^2 - R^2)\sigma_r^2(r) + R^2\sigma_t^2(r)]dr}{r(r^2 - R^2)^{1/2}}, \qquad (4.5)$$

(Binney and Tremaine 1987, p. 208), yielding the optimal value for v_s. The comparison was accomplished using the maximum likelihood technique outlined in Gunn and Griffin (1979). Simply put, the probability density function for v_{zi}, an observed stellar velocity, is a Gaussian with standard deviation equal to the model dispersion plus the velocity uncertainty added in quadrature:

$$P_i \sim \frac{1}{\sqrt{v_{err\,i}^2 + v_s^2 v_{p\,i}}} e^{-(v_{z\,i} - v_{ave})^2 / 2(v_s^2 v_{p\,i}^2 + v_{err\,i}^2)}. \qquad (4.6)$$
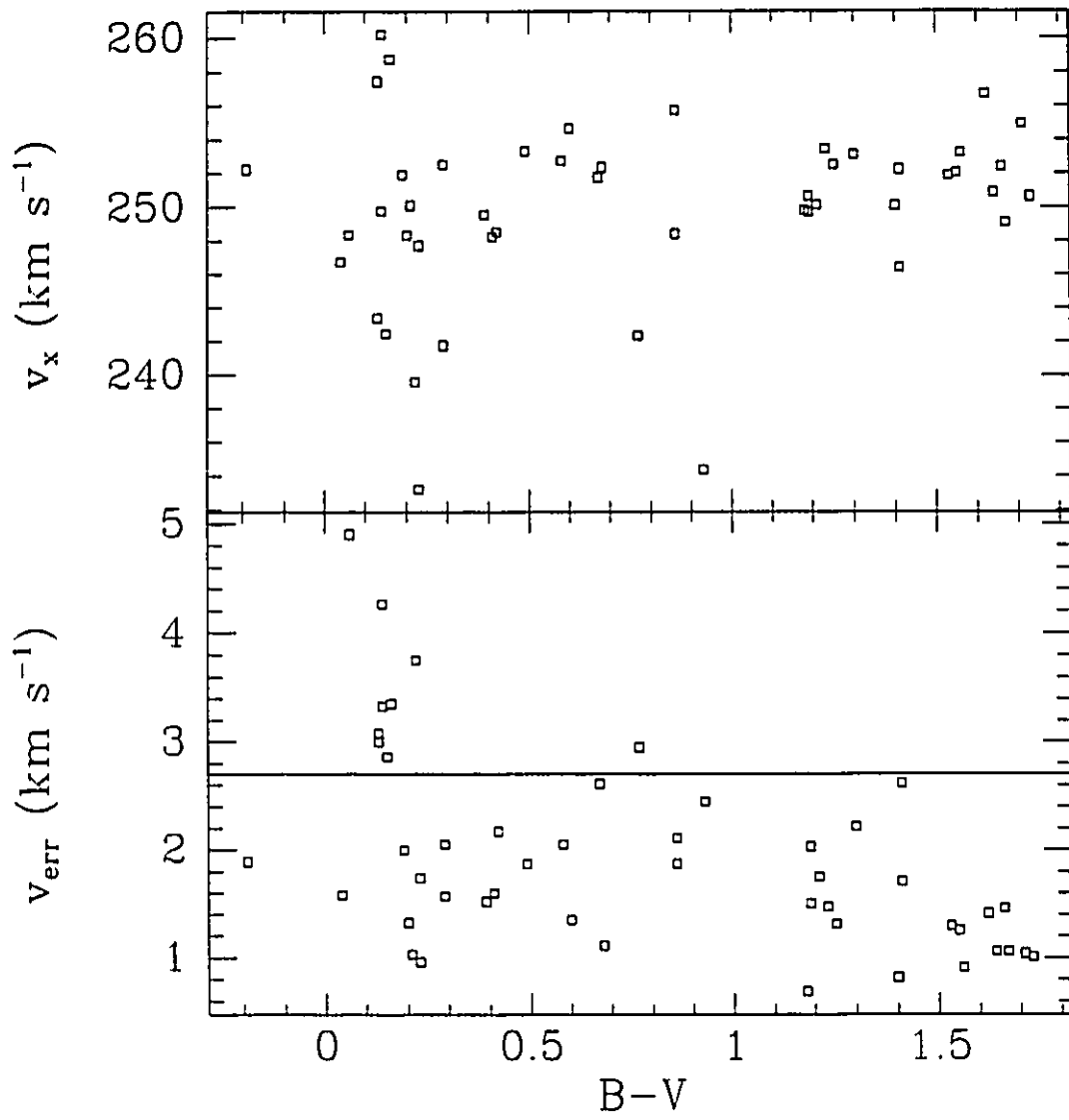
Fig. 4.13 - Radial velocity (upper panel) and velocity uncertainty (lower panel) vs. B-V.

One minimizes this function with respect to v_s and v_{ave} resulting in two equations which can be solved simultaneously for the most probable values of the two parameters.

A serious problem in mass determinations is contamination from binary and non-member stars, both of which tend to increase the mass estimate. This is particularly a problem when one has a relatively small sample of stars and a small velocity dispersion as is the case for NGC 1850. A single interloper in the data sample can easily result in a 50% or greater overestimate in the mass. We attempted to deal with this problem in the following manner. First, using the entire data set, the optimal v_s and v_{ave} are determined using equation 6. For every star the parameter

$$\delta_i = \sqrt{\frac{(v_{ri} - v_{ave})^2}{v_s^2 \sigma_p^2(R_i) + v_{err\ i}^2}} \qquad (4.7)$$

is tabulated. The star with the largest δ_i is removed and the procedure is repeated until all the stars have been removed. Then, using the KM models, we performed Monte Carlo simulations of the radial velocity data. We started with the known projected radii (R_i) of the program stars. The true radius is in the range $R \leq$ r $\leq r_{max}$, where r_{max} can extend to infinity for an unbound distribution. If x is the displacement from the mean cluster position along the line-of-sight such that r $= \sqrt{R^2 + x^2}$ then the probability that the star is at x is

$$p(x) \sim \rho_K(\sqrt{R^2 + x^2}). \qquad (4.8)$$

A three-dimensional position along with corresponding model-dependent radial and tangential velocities were drawn at random from their respective probability distributions. The velocity component along the line-of-sight was then determined, and an error term, drawn from a Gaussian distribution with standard deviation equal to the velocity error, as tabulated in Table 4.8, was added. This process was

repeated, producing 10000 sets of data, each with a given mass and r_a and the same projected positions and velocity measurement errors as the original data set. Finally the maximum likelihood technique was applied to each of the artificial data sets and the maximum δ_i were recorded. The v_s for the first three iterations (using the unshifted radial velocity data) are shown in column 2 of Table 4.9. Columns 3 and 4 are the maximum δ_i and the fraction of simulations with δ_{max} exceeding this value, respectively, and column 5 is the star possessing δ_{max}. A value of zero in the fourth column indicates less than 0.001. We feel that there is a fairly high probability that the first two stars are either variables or non-members and hence they will not be used for the mass determinations. It is worth remembering, however, that their removal results in a mass reduction of about 80% demonstrating the extreme sensitivity of the mass determinations to interlopers. We repeated the procedure with data that was corrected according to the LVS (see §4.3.1) and found similar results but obtained a v_s that was about 2% larger. The fact that it causes an increase in the velocity dispersion argues against its use, but in any case it does not have significant repercussions on the mass estimates and hence was not adopted.

Table 4.9
Velocity Residuals

| Iteration	v_s (km s^{-1})	δ_{max}	$P(> \delta_{max})$	Star
1	4.8	4.35	0.00	39
2	2.8	3.39	0.01	38
3	2.1	2.49	0.39	52

Fig. 4.14 shows mean radial velocity vs. projected radius (upper panel) and versus position angle (lower panel) for the 36 remaining stars. The solid lines are the mean velocity, $\overline{V} = 251.4 \pm 2.0$ km s^{-1}.
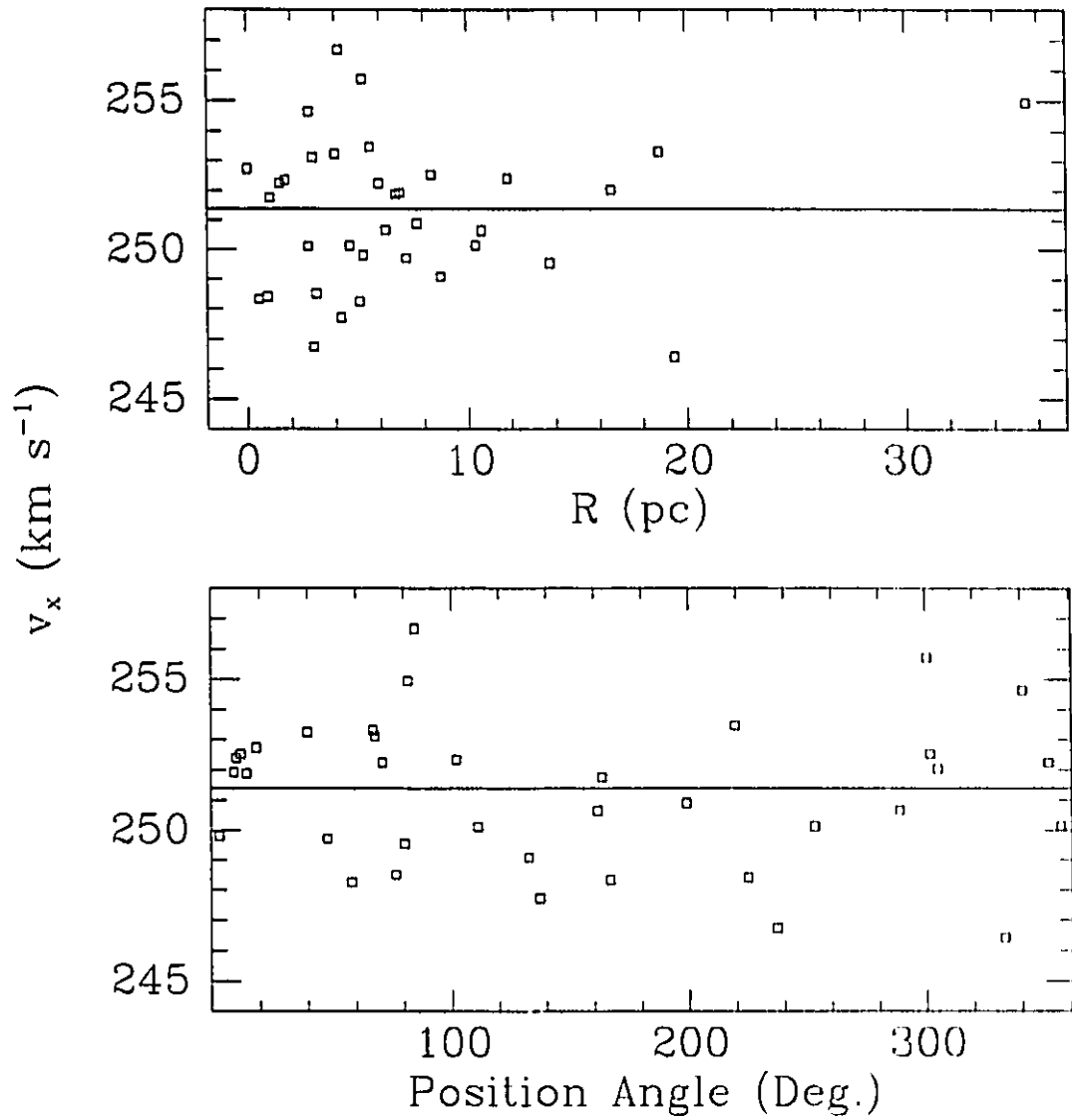
Fig. 4.14 - Mean radial velocity vs. projected radius (upper panel) and versus position angle (lower panel) for the 36 remaining stars. The solid lines are the mean velocity, $\overline{v} = 251.4 \pm 2.0$ km s^{-1}.

The values of v_s obtained from this reduced data set are displayed in column 7 of Tables 4.3 and 4.4. The corresponding masses and M/L ratios are in columns 4 and 5 of Tables 4.5 and 4.6. One can see that the total cluster mass and M/L are fairly insensitive to assumptions about r_a, and the best values are M = 5.7 ±2.3×10⁴ $M_\odot$ and M/L$_B$ = 0.02 ±0.01 $M_\odot$/L$_{B\odot}$ or M/L$_V$ = 0.05 ±0.02 $M_\odot$/L$_{V\odot}$.

The above-described Monte-Carlo orbit simulations were used to determine the uncertainties implicit in the maximum likelihood technique and to search for any possible systematic effects. We found that this method tended to underestimate v_s by about 3% and hence the mass by 6%. The values in the relevant tables have been corrected for this effect and the uncertainties shown were derived from the simulations.

A goodness-of-fit statistic

$$\zeta^2 = \sum \frac{(v_{x\ i} - v_{ave})^2}{(v_s^2 v_p^2{}_i + v_{err\ i}^2)} \tag{4.9}$$

was generated for each value of r_a and is shown in column 8 of Tables 4.3 and 4.4 (34 degrees of freedom). The distribution of this statistic can be extracted from the Monte Carlo simulations. We find that ζ^2 is distributed around N, the number of radial velocity measurements. Values of ζ^2 below the mean tend to indicate that the model is too flat as a function of projected radius for the radial velocity data while high values imply too steep a model. Column 9 shows the probability of being further from the mean than the measured ζ^2 assuming that the cluster velocities are specified by the model parameters indicated and have the uncertainties tabulated in Table 4.8. The isotropic models yielded the best agreement with the data (although, only marginally so) consistent with the findings from the surface photometry.

Because of the similarity between the velocity dispersion and the velocity uncertainty, the mass estimates are quite highly dependent on the the accuracy of

the uncertainty estimates. We have already discussed the analysis of the stars with repeated measurements and concluded that the uncertainties seem to be reasonable with reduced χ^2 near unity. However, it is worth quantifying the effects of the uncertainties. Assuming that the uncertainties are actually zero causes an increase in the estimates of the v_s's by approximately 25%, or a roughly 50% increase in cluster mass. Increasing the uncertainties by 50% lowers the v_s's by 50% and the mass by 75%.

4.4.2   Rotation

A careful examination of the radial velocities vs. position angle (Fig. 4.14) reveals evidence for a sinusoidal variation which may be indicative of cluster rotation. In order to test this hypothesis we measured the difference in median velocities on either side of an imaginary axis which is stepped around the cluster center at $1°$ intervals. If one is viewing an edge-on rotating system then a sinusoidal variation is expected with the velocity difference maximized when the axis corresponds to the rotation axis. This effect will degrade as the system deviates from edge-on. The bottom left panel of Fig 4.15 shows a plot of the velocity differences versus the position angle of the axis. The best-fit sine curve (using unweighted least-squares) has an amplitude of A = 2.1 km s^{-1} and the implied projected rotation axis is $100° \pm 40°$ ($\chi^2 = 25.12$ for 178 degrees of freedom). To test the significance, we constructed 1000 non-rotating models as described above and performed the same test. Only 7% of these models had amplitudes exceeding A = 2.1 and hence we feel fairly confident that NGC 1850 is rotating. Rotation has previously been detected at the 97% confidence level for a sample of 69 stars in the young LMC cluster NGC 1866 (Fischer et al. 1992a) which had A = 1.8 km s^{-1} and v_s = 3.1 km s^{-1}. In that case, incorporation of rotation resulted in only a very small downward changes

in the mass estimate. However, in the case of NGC 1850, the two parameters have very similar values meaning rotation may be dynamically more significant than it was in NGC 1866.

Unfortunately, as explained in §4.2.3 it is impossible to extract a meaningful ellipticity from the NGC 1850 light distribution. This information would have enabled us to construct rotating oblate cluster models to compare with the radial velocities. We therefore adopted an alternative approach of assuming different ellipticities values for the cluster, constructing models for the rotation, and comparing them to the data.

For an axisymmetric system, the relevant Jeans' equations (velocity moments of the collisionless Boltzmann equation) in cylindrical coordinates are:

$$\frac{\partial(\rho\sigma_{\rm R}^2)}{\partial{\rm R}} + \frac{\partial(\rho\sigma_{{\rm R}z})}{\partial z} + \rho\left(\frac{\sigma_{\rm R}^2 - \sigma_\phi^2 - v_\phi^2}{\rm R}\right) + \rho\frac{\partial\Phi}{\partial{\rm R}} = 0, \qquad (4.10)$$

and

$$\frac{\partial(\rho\sigma_{{\rm R}z})}{\partial{\rm R}} + \frac{\partial(\rho\sigma_z^2)}{\partial z} + \frac{\rho\sigma_{{\rm R}z}}{\rm R} + \rho\frac{\partial\Phi}{\partial z} = 0, \qquad (4.11)$$

where (R,ϕ,z) are the cylindrical coordinate axes, the ($\sigma_{\rm R},\sigma_\phi,\sigma_z$) are the corresponding velocity dispersions, and v_ϕ is the rotation velocity. Φ is the gravitational potential.

Both the rotating and non-rotating models which were used have velocity ellipsoids aligned with the cylindrical coordinate axes (i.e. $\sigma_{{\rm R}z} = 0$) and, as well, both have

$$\sigma_\phi = \frac{\sigma_{\rm R}}{\sqrt{1 + ({\rm R}/{\rm R}_a)^2}}, \qquad (4.12)$$

where $\rm R_a$ can be varied up to ∞. The rotating models also have the condition

$$\sigma_{\rm R} = \sigma_z, \qquad (4.13)$$
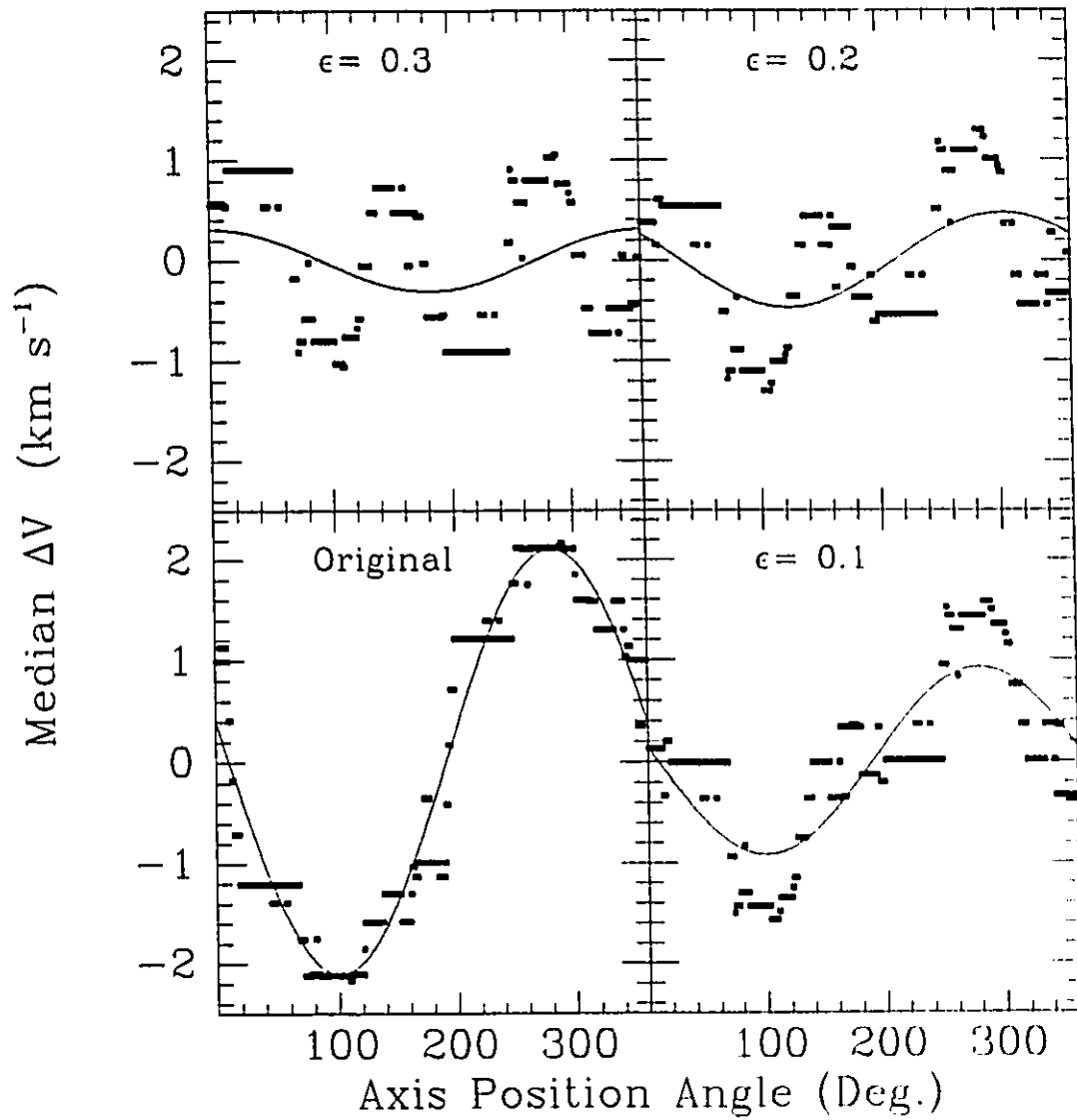
Fig. 4.15 - The lower left panel displays the difference in median velocity for stars on either side of an axis at the specified position angle. Also shown is the best fit sine function corresponding to a rotation axis with position angle 100°. The other panels show the same thing but for velocity data which has been rotation-subtracted assuming the specified ellipticities and the models described in §4.4.2

implying

$$v_\phi^2 = R\frac{\partial\Phi}{\partial R} + \frac{R}{\rho}\frac{\partial}{\partial R}\int_z^\infty \rho\frac{\partial\Phi}{\partial z}dz + \frac{1}{\rho}\left[1 - \frac{1}{\sqrt{1+(R/R_a)^2}}\right]\int_z^\infty \rho\frac{\partial\Phi}{\partial z}dz. \quad (4.14)$$

The models are constructed by assuming that the mass distribution is equivalent to the deprojected light distribution (constant M/L). Equations 4.11 and 4.14 can then be solved directly to obtain σ_z, and v_ϕ. Once v_ϕ is known it can be substituted into equation 10 which, in turn, can be solved for σ_R and σ_ϕ. This is outlined in Binney and Tremaine (1987, p. 209) for the $\sigma_R = \sigma_\phi = \sigma_z$ case and a $\epsilon = 0.3$ model is shown in Fig. 3.7.

Once the models have been generated, it is simply a matter of projecting and then scaling them using a similar maximum likelihood method to that employed for the KM models. For our purposes we have constructed models spanning $\epsilon = 0.1 - 0.3$ for $R_a = \infty$. All of the models assume a cluster inclination of 90°. Table 4.10 displays the results of the model fitting. Column 1 is the ellipticity, column 2 the cluster mass, columns 3 and 4 the B and V M/L's, and columns 5 and 6 are ζ^2 and $P(|\zeta^2 - N|)$ as above. These models all have $P(|\zeta^2 - N|)$ of similar value to the best non-rotating KM models despite having larger ζ^2 values. However, as can be seen from Fig. 3.8 of Fischer *et al.* (1992b) the rotating models have a wider ζ^2 distribution. Furthermore, from simulations of this data set, the ζ^2 tend to be biased too high when the rotation is overestimated and too low when rotation is underestimated. The rotating models have masses (and M/L's) which are marginally lower than the non-rotating models. Fig. 4.15 exhibits plots of the velocity differences vs. axis position angle for the original and rotation-subtracted data. Column 7 of Table 4.10 is the amplitude of the best-fit sine curves for each case. One can see that the amplitude decreases for the rotation subtracted data with increasing ϵ. It does not, however, decrease smoothly to zero and one can see that

for the $\epsilon = 0.3$ case there is a residual trend in the data which does not disappear for higher ellipticities. This probably results from some type of model mismatch which may be a result of the model itself or might be due to a poorly determined rotation axis position angle or an inclination of less than $90°$. We changed the rotation axis position angle by plus and minus $20°$ but found that the residual velocities did not improve. Another possibility is that the characteristic rotational signature arises from the interaction between the two binary cluster components. The resulting stellar motions might in such a case have a similar appearance to rotation.

Table 4.10
Rotating Ellipsoidal Models

ϵ	Mass $(10^4 \ M_\odot)$	M/L_B $(M_\odot/L_{B\odot})$	M/L_V $(M_\odot/L_{V\odot})$	ζ^2	$P(|\zeta^2 - N|)$	A $(km \ s^{-1})$
0.1	5.5 ± 0.2	0.02 ± 0.01	0.04 ± 0.02	37.47	0.56	0.9
0.2	5.6 ± 0.2	0.02 ± 0.01	0.04 ± 0.02	38.76	0.39	0.5
0.3	5.5 ± 0.2	0.02 ± 0.01	0.04 ± 0.02	40.58	0.24	0.3

4.5   CONSTRAINTS ON THE MASS FUNCTION

The cluster M/L estimate can be used to constrain the slope of the initial mass function (IMF). In this study we used an IMF of the form

$$\phi(m) = m^{-(x+1)} \ dm \qquad m \geq m_d, \qquad (4.15)$$

$$\phi(m) = m \ dm \qquad m < m_d, \qquad (4.16),$$

which gives a drop-off at the faint end similar to what is seen in the solar neighborhood (Miller & Scalo 1979).

The theoretical cluster M/L is given by

$$\frac{M}{L} = \frac{\int_{m_l}^{m_u} m\phi(m)dm}{\int_{m_l}^{m_u} l(m)\phi(m)dm}, \qquad (4.17)$$

where $l(m)$ is the luminosity of a star of mass m given by a theoretical mass-luminosity relationship for main-sequence and evolved stars. We used the mass-luminosity relationship of Mermilliod (1992), supplemented with the Bergbusch & Vandenberg (1992) values in the range $0.15 \leq m$ ($M_\odot$) ≤ 0.9, with the cluster parameters determined in §4.2.2. The initial mass of a star now at the end of the asymptotic giant branch is approximately 5.4 $M_\odot$. We have adopted the treatment of Pryor *et al.* 1986 to deal with remnants: stars with initial masses of 5.4 - 8.0 $M_\odot$ become white dwarfs with masses of 1.2 $M_\odot$ and stars with initial masses greater than 8 $M_\odot$ are assumed to be ejected from the cluster as is consistent with the high velocities seen for pulsars in the disk (Gunn and Griffin 1979). Therefore, the choice of m_u is not important except for estimating the amount of mass lost from the cluster due to stellar evolution.

Table 4.11 shows the derived values of x (column 3 and 5) for 3 different m_l (column 1), and 5 different m_d (column 2). Columns 4 and 6 contain the implied mean stellar mass for the given model. The values of x correspond to the B and V M/L's indicated at the top of the table. Although the values corresponding to the B and V M/L's are consistent within the uncertainty, the B-band x's are systematically lower. It appears that for a given set of assumptions the V-band M/L constrains the mass function slope somewhat more tightly than the B-band. Furthermore, the V-band is also less sensitive to the assumed cluster age although one finds that the both the slopes steepen for a younger assumed age and flatten for older (this has not been accounted for in the uncertainty). The B-band has one advantage in that it appears to be less sensitive to the low mass cut-off. Both sets of slopes are substantially shallower than was seen for the young LMC cluster NGC 1866 (Fischer *et al.* 1992a), which had an average slope (i.e. as determined without

Table 4.11
Mass Functions

M/L =		0.02 ± 0.01 M$_\odot$/L$_{B\odot}$		0.05 ± 0.02 M$_\odot$/L$_{V\odot}$	
m_l	m_d	x	$<m>$	x	$<m>$
(M$_\odot$)	(M$_\odot$)		(M$_\odot$)		(M$_\odot$)
0.05	0.0	0.29 $^{+0.3}_{-0.8}$	0.75	0.71 $^{+0.2}_{-0.4}$	0.37
0.05	0.3	0.31 $^{+0.3}_{-0.8}$	0.83	0.79 $^{+0.2}_{-0.4}$	0.50
0.05	0.5	0.32 $^{+0.3}_{-0.9}$	0.87	0.85 $^{+0.3}_{-0.5}$	0.57
0.05	1.0	0.38 $^{+0.5}_{-1.0}$	0.93	1.04 $^{+0.4}_{-0.6}$	0.69
0.05	1.5	0.46 $^{+0.5}_{-1.2}$	0.97	1.28 $^{+0.5}_{-0.8}$	0.77
0.1	0.0	0.32 $^{+0.3}_{-0.8}$	0.93	0.77 $^{+0.2}_{-0.4}$	0.54
0.1	0.3	0.33 $^{+0.3}_{-0.8}$	0.98	0.81 $^{+0.2}_{-0.4}$	0.62
0.1	0.5	0.35 $^{+0.4}_{-0.9}$	1.01	0.88 $^{+0.3}_{-0.5}$	0.69
0.1	1.0	0.41 $^{+0.5}_{-1.0}$	1.08	1.06 $^{+0.4}_{-0.6}$	0.82
0.1	1.5	0.48 $^{+0.6}_{-1.2}$	1.13	1.30 $^{+0.5}_{-0.8}$	0.90
0.15	0.0	0.34 $^{+0.3}_{-0.8}$	1.06	0.81 $^{+0.2}_{-0.4}$	0.66
0.15	0.3	0.35 $^{+0.3}_{-0.8}$	1.08	0.84 $^{+0.2}_{-0.5}$	0.71
0.15	0.5	0.37 $^{+0.4}_{-0.9}$	1.12	0.90 $^{+0.3}_{-0.5}$	0.78
0.15	1.0	0.43 $^{+0.4}_{-1.0}$	1.19	1.08 $^{+0.4}_{-0.6}$	0.91
0.15	1.5	0.51 $^{+0.6}_{-0.2}$	1.23	1.32 $^{+0.5}_{-0.8}$	1.00

employing a drop-off in the mass function) of between $x = 1.35$ ±0.1 and $x = 1.82$ ±0.1 (depending on adopted age) for $m_l = 0.1$.

4.6   EVOLUTIONARY TIMESCALES

The stars with measured velocities are all supergiants, with relatively large masses. If equipartition of energy has occurred these stars, being the most massive, would have a velocity dispersion below the mean value for all mass classes. Therefore, in order to justify the use of single-mass models we must demonstrate 'hat the cluster is sufficiently young such that equipartition and mass segregation have not had enough time to become significant effects. Two important timescales are the

central relaxation time

$$
t_{ro} = (1.55 \times 10^7 \mathrm{yr}) \left(\frac{r_s}{\mathrm{pc}} \right)^2 \left(\frac{v_s}{\mathrm{km\ s}^{-1}} \right) \left(\frac{M_\odot}{\langle m \rangle} \right) [\log(0.5 M / \langle m \rangle)]^{-1}
$$
$$
= 0.4 - 2.2 \times 10^8 \mathrm{yr} \tag{4.18}
$$

(Lightman and Shapiro 1978) and the half mass relaxation time

$$
t_{rh} = (8.92 \times 10^8 \mathrm{yr}) \left(\frac{M}{10^6 M_\odot} \right)^{1/2} \left(\frac{r_h}{\mathrm{pc}} \right)^{3/2} \left(\frac{M_\odot}{\langle m \rangle} \right) [\log(0.4 M / \langle m \rangle)]^{-1}
$$
$$
= 1.5 - 5.3 \times 10^9 \mathrm{yr} \tag{4.19}
$$

(Spitzer and Hart 1971). The parameters in these equations have all been discussed previously except for the half mass radius, $r_h \simeq 11$ pc. Aside from the inner core the cluster is in a dynamically unevolved state and, therefore, we do not expect substantial energy transfer to have occurred. We conclude that no large systematic errors are being introduced into the velocity dispersions.

Another possible problem is primordial mass segregation. This would occur if star formation in the dense core region favored a different ratio of high-to-low mass stars than at larger radii. While this should not affect the velocity dispersion greatly, it would mean that the assumption of a uniform M/L is incorrect. Consequently the derived luminosity density profiles would not be an adequate representation of the mass density profile. One should be able to construct luminosity functions at different projected cluster radii and hence search for a gradient in mass function. In practice, owing to the very crowded nature of the inner cluster regions and the high surface density of non-member stars present on the frame this would be difficult to accomplish in a convincing manner and we have not attempted it.

4.7   CONCLUSIONS

In this paper we have examined the age and internal dynamics of the young binary LMC cluster NGC 1850 using BV CCD images and echelle spectra of 52 supergiants.

1) A BV CMD was constructed for the field surrounding the cluster and was found to contain 3 distinct populations of stars. The first was a very young population of age $\tau = 6 \pm 5$ Myr belonging primarily to the smaller member of the binary system located $30''$ west of the larger member. This young population allowed for an accurate reddening estimate of E(B-V) = 0.17 $\pm$0.03 mag. The second, slightly older population, belongs primarily to the the larger cluster and has an age of $\tau = 90 \pm 30$ Myr. The third population was older and mainly comprised of LMC field stars.

2) Attempts were made to determine ellipticity parameters for the cluster using star-subtracted, median filtered BV images. This was greatly complicated by the presence of extremely bright young resolved stars and the binary nature of the cluster and no meaningful shape parameters were derived.

3) BV luminosity profiles were constructed out to projected radii of R > 40 pc. Single component King-Michie (KM) models were applied to this data in order to determine the most favorable value for the anisotropy radius and the total cluster luminosity. The luminosity varied from $L_B = 2.60 - 2.65 \pm 0.2 \times 10^6$ $L_{B\odot}$ and $L_V = 1.25 - 1.35 \pm 0.1 \times 10^6$ $L_{V\odot}$ as r_a went from to infinity to $3r_s$. The fitted and derived KM parameters for both bandpasses were consistent and the isotropic models provided the best agreement with the data.

4) To test for the presence of a tidal cut-off in the luminosity profile, a power-law model without truncation was applied to the data. This model was found to

provide marginally worse fits than the KM models giving some indication that the cluster density distribution is truncated.

5) Of the 52 stars with echelle spectra, a subset of 36 were used to study the cluster dynamics. The KM radial velocity distributions were fitted to these velocities yielding scale velocities of $v_s = 2.2 - 2.3 \pm 0.5$ km s^{-1} for the r_a range employed. The total cluster mass was 5.4 - 5.9 $\pm 2.4 \times 10^4$ M$_\odot$ corresponding to M/L$_B = 0.02 \pm 0.01$ M$_\odot$/L$_{B\odot}$ or M/L$_V = 0.05 \pm 0.02$ M$_\odot$/L$_{V\odot}$. The mean cluster velocity is $\overline{V} = 251.4 \pm 2.0$ km s^{-1}.

6) A rotational signal in the radial velocities has been detected at the 93% confidence level implying a rotation axis at a position angle of $100° \pm 40°$. A variety of rotating models were fit to the velocity data assuming $\epsilon = 0.1 - 0.3$. These models provided slightly better agreement with the radial velocity data than the KM models and had masses that were systematically lower by a few percent.

7) Values for the slope of the mass function were determined using the derived M/L, theoretical mass-luminosity relationships, and several forms for the IMF. The preferred value for the slope of a power-law IMF is a relatively shallow, $x = 0.29$ $^{+0.3}_{-0.8}$ assuming the B-band M/L or $x = 0.71$ $^{+0.2}_{-0.4}$ for the V-band.

8) The current cluster age is similar to its central relaxation time but about 2 orders of magnitude less than its half-mass relaxation time. Therefore, aside from in the inner core the cluster is in a dynamically unevolved state and we expect that equipartition has not yet occurred in any substantial way.

ACKNOWLEDGEMENTS

Reprints of this paper are available through mail or anonymous FTP. Contact Fischer@crocus.physics.mcmaster.ca for information.

Chapter 5

We have included conclusion sections at the end of Chapters 2, 3, and 4 for the three clusters NGC 1866, NGC 1978, and NGC 1866, respectively. Here we will discuss some highlights and some general conclusions regarding the dynamics of the three studied LMC clusters.

1) In all three cases, the cluster kinematics were most consistent with isotropic stellar orbits, however, the size of the radial velocity samples did not allow us to place very strong constraints on the orbital parameters. The surface density profiles (SDPs) of NGC 1850 and NGC 1978 tended to agree with the

kinematics and favor isotropic orbits. The SDP of NGC 1866, however, gave the best agreement with highly anisotropic orbits. The stellar orbits in this cluster may, in fact be anisotropic. It is, after all, considerably younger than its half-mass relaxation time and the velocities do not agree particularly well with the isotropic model. It is also possible, however, that this cluster possesses an unbound halo of stars formed either at the time of the initial molecular cloud collapse or as a result of early stellar mass loss. This halo would tend to give the cluster a more extended appearance and hence give the false impression that the stars have more radial orbits.

2) The two youngest clusters, NGC 1850 and NGC 1866 have much higher values of v_0/σ than is seen for any GGCs. This probably indicates that clusters tend to shed their angular momentum (i.e. through preferential stellar evaporation) as they evolve. The result that NGC 1978 is probably not rotating is one of the major surprises of this thesis. The question arises as to whether other flattened intermediate-age and old Magellanic Cloud (MC) clusters are similarly non-rotating.

3) The cluster mass-to-light ratios (M/L) derived in this thesis correspond to power-law mass function slopes contained within the range of slopes seen for the Galactic globular clusters (GGCs). The one possible exception to this statement is NGC 1978. One way to reconcile the M/L of NGC 1978 with the single-mass models is to invoke an extremely high low-mass cut-off (i.e. 0.8 $M_\odot$, assuming a simple power-law mass function). This is, of course, completely inconsistent with the GGCs where the tip of the main sequence is typically around this value and stars with masses as low as 0.12 $M_\odot$ have been observed. It is, however, possible to obtain good agreement with the population and dynamical M/L if one invokes multi-mass models. Alternatively, one can adopt

a more complex form of the mass function, presumably with a flattening at the low mass end to explain the low M/L. On the more speculative side, it is possible that the degree of flattening and loss-rate of low-mass stars are related.

There are two related projects that I would like to pursue:

1) Dynamics of old and intermediate age elliptical MC clusters. This is motivated by the intriguing results for NGC 1978. Do the other clusters exhibit similar dynamics or are they rotationally supported? At a recent conference (The Globular Cluster - Galaxy Connection) Dr. M. Weinberg claimed that any initial cluster ellipticity would rapidly disappear due to the parent galaxy's tidal field. The presence of highly elliptical old clusters in the MC (i.e. NGC 121) seems to contradict this hypothesis. If, however, the ellipticity is a result of a recent merger then the theory may not be threatened.

2) Hubble Space Telescope luminosity functions for the young LMC clusters. High angular resolution photometry is desperately needed to study the luminosity/mass functions of the young clusters. These will enable us to measure the upper end of the mass function directly, which is only possible to do reliably in the MC clusters (open clusters tend to be too sparse so membership is a problem). Furthermore, with the upper end tied down, it will be possible to construct much more reliable dynamical models and thus constrain the stellar remnants and the low mass end of the mass function more effectively. It would also be very interesting to obtain a luminosity function for NGC 1978 to see if one could reconcile the population and dynamical M/L without requiring the large amounts of mass segregation needed with a simple power-law mass function.

APPENDIX

King-Michie Multi-Mass Models

In this appendix we will give further details of the KM multi-mass models which were used in chapter 3 to fit the surface brightness profiles of NGC 1978. The models are based on the anisotropic single-mass KM models of King (1966) and Michie (1962) and are an approximate solution to the spherical steady-state Fokker-Planck equation. Early on it was recognized that the central relaxation times of most globular clusters were sufficiently short that equipartition of energy between stars of different mass would have occurred (Spitzer 1969). The models were first extended into the multi-mass regime by Da Costa & Freeman (1976) for the isotropic case, and by Gunn & Griffin (1979) for the anisotropic case. Below we describe these models including a test run of a model with a specified parameter set showing several iterations of the model through to convergence. This will be a useful means of testing newly coded models.

The stellar mass spectrum is sub-divided into mass classes; six will be used in this example (see Table A.1). All the stars in mass class i are assumed to have masses equal to the mean mass within that class, m_i. Mass class i has an energy per unit mass $[E = 1/2v^2 + W(r)$, where r is the distance from the center] and angular momentum per unit mass ($J = v^2 r^2 \sin^2 \theta$, where θ is the angle from the given position to the usual z-axis) per unit mass distribution function given by:

$$f_i(E, J) = f_i(r, \theta, v, W(r)) = \qquad (A.1)$$

$$C_i \exp\left(\frac{-1}{2} \frac{m_i}{\overline{m}} \frac{v^2}{v_s^2} \frac{r^2}{r_a^2} \sin^2 \theta\right) \left\{ \exp\left[\frac{-1}{2} \frac{m_i}{\overline{m}} \frac{v^2}{v_s^2} + \frac{m_i}{\overline{m}} W(r)\right] - 1 \right\},$$

and the density of mass class i at a radius r' is given by:

$$\rho_i(r') = 2\pi C_i \int_{-\sqrt{2W(r')}}^{\sqrt{2W(r')}} \int_0^\pi f_i[r = r', \theta, v, W = W(r')]v^2 \sin\theta d\theta dv \qquad (A.2)$$

where ρ_0 and ρ_{i0} are the total central density and central density of mass class i, respectively. The variable $\overline{m}$ is the mean mass of all the mass classes at the center (r=0), v_s is the scale velocity determined by scaling the model velocities until agreement with the measured radial velocities is achieved, r_a is the anisotropy radius beyond which the stellar orbits become increasingly radial, and $W(r)$ is the reduced potential, equal to W_0 at the center and zero at the cluster edge. The C_i are given by the condition.

$$\rho_{i0} = 4\pi C_i \int_{-\sqrt{2W_0}}^{\sqrt{2W_0}} f_i(r = 0, \theta, v, W = W_0)v^2 dv \qquad (A.3)$$

The goal is to solve for the density structure of all the mass classes in a self-consistent manner. In order to achieve this one must use Poisson's equation to solve for the potential. It can be expressed as two linear, coupled differential equations:

$$H = \frac{\partial W(r/r_s)}{\partial(r/r_s)}, \qquad (A.4)$$

and

$$\frac{\partial H}{\partial(r/r_s)} = \frac{-2H}{(r/r_s)} - 9\frac{\rho}{\rho_0}, \qquad (A.5)$$

where r_s is determined by scaling the model to fit the data and we have assumed that $\nabla^2 W(r = 0) = -9$ in order to make r_s approximately equal to the core radius for the isotropic $(r_a = \infty)$ models.

The boundary conditions are $W(r = 0) = W_0$, and $\partial W(r = 0)/\partial(r/r_s) = 0$. Through use of a power-series expansion one can show that

$$\lim_{r \to 0} \frac{2}{r/r_s} \frac{\partial W(r = 0)}{\partial(r/r_s)} = -6. \qquad (A.6)$$

We will now construct a multi-mass KM model with $W_0 = 5.0$ and a mass function given by:

$$\phi(m) = m^{-(x+1)} \; dm \qquad m \geq 0.30 M_\odot,$$

$$\phi(m) = m \; dm \qquad 0.15 < m < 0.30 M_\odot, \qquad (A.7)$$

$$\phi(m) = 0 \; dm \qquad m < 0.15 M_\odot,$$

with $x = 1.35$ (Salpeter). Remnants are treated as follows: stars with initial masses of 0.80 - 1.5 $M_\odot$, 1.5 - 4.0 $M_\odot$, and 4.0 - 8.0 $M_\odot$ become white dwarfs with masses of 0.5 $M_\odot$, 0.7 $M_\odot$, and 1.2 $M_\odot$, respectively. These objects are added to the corresponding mass classes which are described in Table A.1. Column 1 is the mass class, columns 2 and 3 are the minimum and maximum masses, respectively, and column 4 is the mean mass of the mass class. Column 5 is the total mass in each mass class normalized such that the sum of all the classes is unity. It is also the first guess at the relative central mass density (see below).

Table A.1
Mass Bins

Bin	m_{min} ($M_\odot$)	m_{max} ($M_\odot$)	$\overline{m}$ ($M_\odot$)	$M(x = 1.35)$
1	0.15	0.30	0.22	0.29
2	0.30	0.45	0.36	0.22
3	0.45	0.60	0.51	0.25
4	0.60	0.75	0.68	0.18
5	0.75	0.80	0.77	0.03
6	4.00	8.00	1.20	0.03

In order to solve Poisson's equation for the potential we need to know the density of each mass class at the center. Clearly, we do not know this *a priori*, and, in fact, it is one of the things we are trying to determine. Therefore, we first assume values for these central densities, and then use an iterative approach until the total mass in each mass class converges to the expected mass $[M_i(x = 1.35)]$. For our first

guesses we assume no mass segregation (i.e. all mass classes distributed identically) and determine the relative central densities directly from the mass function (column 5 of Table A.1). Table A.2 shows the model radius, $W(r)$, and the densities of mass classes 1 through 6 after the first iteration. At the bottom of Table A.2 we have tabulated four values: 1) C_i from Eqn. A.3, 2) the percentage of the total mass in the given mass class (M_i), 3) the percentage difference of the total mass from the expected mass based on the mass function

$$\delta_i = \frac{M_i - M_i(x = 1.35)}{M_i(x = 1.35)}, \qquad (A.8)$$

and 4) the new relative central density for the next iteration given by:

$$\rho_{0i}(\text{new}) = \rho_{0i} \left[\frac{M_i(x = 1.35)}{M_i} \right]. \qquad (A.9)$$

With the $\rho_{0i}(\text{new})$ now determined, $\overline{m}$ and C_i can be recalculated and the next iteration can proceed. Tables A.3 - A.6 are similar to Table A.2 but are subsequent iterations. One can see that the $\rho_{0i}(\text{new})$'s tend to be over-corrected causing the M_i's to fluctuate above and below their expected value. This suggests that a smaller correction might be more appropriate. However, the model does converge, where the convergence criterion is that each M_i must be within 2% of the corresponding $M_i(x = 1.35)$.

The next step is to convert the mass densities into observables. This can take one of two forms: 1) surface density profiles, or surface brightness profiles. In the case of the former, the mass density profiles must be converted to number density profiles corresponding to the mass range that was used to construct the surface density profile. In the latter case, one must use a mass-luminosity relationship for each mass class based on stellar models. The spatial densities (either number or brightness) must be projected on to the observational plane to yield a surface density:

$$\mu(R) = \int_R^{r_t} \sum_{i=1}^{n} \rho_i(r')dr', \qquad (A.10)$$

where R is the projected distance from the center, r_t is the tidal radius, the point where both the potential and density are equal to zero, and n is number of mass classes. The final step is to scale in both the radial and density dimensions in order to obtain the best fit to the data.

Table A.2
Density Profiles - Iteration 1

r (r_s)	W	ρ_1	ρ_2	ρ_3	ρ_4	ρ_5	ρ_6
0.00	5.00	0.29119681	0.22014990	0.24771061	0.18220735	0.02696875	0.03176658
0.07	4.99	0.28951276	0.21849554	0.24531527	0.17991580	0.02658612	0.03107335
0.14	4.97	0.28572116	0.21478412	0.23996329	0.17482171	0.02573787	0.02955595
0.22	4.93	0.27756291	0.20686144	0.22864041	0.16416473	0.02397395	0.02648782
0.32	4.85	0.26206173	0.19204765	0.20784985	0.14503715	0.02084639	0.02134808
0.47	4.70	0.23576774	0.16765374	0.17474378	0.11583492	0.01617811	0.01443999
0.66	4.46	0.19671240	0.13319205	0.13055968	0.07955146	0.01059622	0.00752651
0.86	4.17	0.15757517	0.10090736	0.09223485	0.05101219	0.00643158	0.00349669
1.06	3.87	0.12376348	0.07496931	0.06391463	0.03206899	0.00382391	0.00157928
1.26	3.57	0.09623570	0.05530820	0.04415342	0.02019533	0.00228262	0.00072125
1.46	3.29	0.07453349	0.04081790	0.03068743	0.01289262	0.00138677	0.00034054
1.66	3.03	0.05770417	0.03025604	0.02155617	0.00839062	0.00086295	0.00016804
1.86	2.78	0.04474965	0.02256940	0.01533167	0.00557720	0.00055113	0.00008698
2.06	2.55	0.03479839	0.01695469	0.01104416	0.00378534	0.00036110	0.00004722
2.26	2.34	0.02714641	0.01282724	0.00805301	0.00261992	0.00024231	0.00002681
2.46	2.15	0.02124634	0.00976996	0.00593805	0.00184578	0.00016616	0.00001587
2.66	1.97	0.01668048	0.00748721	0.00442274	0.00132105	0.00011614	0.00000974
2.86	1.81	0.01313278	0.00576925	0.00332336	0.00095863	0.00008256	0.00000618
3.06	1.66	0.01036476	0.00446659	0.00251645	0.00070399	0.00005955	0.00000404
3.26	1.53	0.00819636	0.00347188	0.00191789	0.00052228	0.00004348	0.00000270
3.46	1.40	0.00649123	0.00270745	0.00146965	0.00039081	0.00003209	0.00000185
3.66	1.29	0.00514571	0.00211659	0.00113109	0.00029452	0.00002389	0.00000129
3.86	1.18	0.00408066	0.00165754	0.00087347	0.00022322	0.00001791	0.00000091
4.06	1.08	0.00323536	0.00129930	0.00067613	0.00016993	0.00001351	0.00000065
4.26	0.99	0.00256296	0.00101868	0.00052412	0.00012978	0.00001023	0.00000047
4.46	0.91	0.00202715	0.00079816	0.00040647	0.00009931	0.00000777	0.00000034
4.66	0.83	0.00159966	0.00062444	0.00031506	0.00007605	0.00000591	0.00000025
4.86	0.76	0.00125835	0.00048735	0.00024382	0.00005822	0.00000449	0.00000019
5.06	0.69	0.00098584	0.00037906	0.00018818	0.00004449	0.00000342	0.00000014
5.26	0.63	0.00076839	0.00029349	0.00014468	0.00003390	0.00000259	0.00000010
5.46	0.57	0.00059511	0.00022591	0.00011064	0.00002571	0.00000195	0.00000007
5.66	0.51	0.00045733	0.00017262	0.00008404	0.00001939	0.00000147	0.00000005
5.86	0.46	0.00034813	0.00013071	0.00006329	0.00001450	0.00000109	0.00000004
6.06	0.41	0.00026196	0.00009788	0.00004715	0.00001073	0.00000081	0.00000003
6.26	0.37	0.00019436	0.00007229	0.00003466	0.00000784	0.00000059	0.00000002
6.46	0.32	0.00014172	0.00005249	0.00002506	0.00000564	0.00000042	0.00000001
6.66	0.28	0.00010114	0.00003731	0.00001774	0.00000397	0.00000030	0.00000001
6.86	0.25	0.00007025	0.00002582	0.00001223	0.00000273	0.00000020	0.00000001
7.06	0.21	0.00004713	0.00001726	0.00000815	0.00000181	0.00000013	0.00000000
7.26	0.18	0.00003019	0.00001102	0.00000519	0.00000115	0.00000008	0.00000000
7.46	0.14	0.00001817	0.00000661	0.00000310	0.00000068	0.00000005	0.00000000
7.66	0.11	0.00000999	0.00000362	0.00000169	0.00000037	0.00000003	0.00000000
7.86	0.08	0.00000477	0.00000173	0.00000081	0.00000018	0.00000001	0.00000000
8.06	0.06	0.00000178	0.00000064	0.00000030	0.00000007	0.00000000	0.00000000
8.26	0.03	0.00000038	0.00000014	0.00000006	0.00000001	0.00000000	0.00000000
8.46	0.01	0.00000001	0.00000000	0.00000000	0.00000000	0.00000000	0.00000000
C_i =		0.00631224	0.00135055	0.00044575	0.00007204	0.00000465	0.00000010
M_i =		0.49734834	0.24721955	0.17298181	0.07125876	0.00789724	0.00329430
δ_i =		0.70794571	0.12296006	-0.30167783	-0.60891389	-0.70717069	-0.89629679
ρ_{0i}(new) =		0.10752855	0.12364183	0.22371753	0.29383581	0.05808413	0.19319215

Table A.3
Density Profiles - Iteration 2

r (r_s)	W	ρ_1	ρ_2	ρ_3	ρ_4	ρ_5	ρ_6
0.00	5.00	0.10752855	0.12364183	0.22371753	0.29383581	0.05808413	0.19319215
0.07	4.99	0.10697408	0.12288441	0.22207760	0.29118142	0.05750180	0.19028298
0.14	4.97	0.10572395	0.12118036	0.21839721	0.28524374	0.05620152	0.18384296
0.22	4.93	0.10302580	0.11751981	0.21053444	0.27264945	0.05345448	0.17049422
0.32	4.85	0.09786721	0.11058771	0.19580894	0.24940425	0.04842503	0.14698060
0.47	4.70	0.08901641	0.09890199	0.17148961	0.21203540	0.04045943	0.11230820
0.66	4.46	0.07561514	0.08172815	0.13696672	0.16135436	0.02992619	0.07170166
0.86	4.17	0.06183609	0.06476240	0.10441394	0.11642367	0.02090382	0.04225764
1.06	3.87	0.04959628	0.05032727	0.07807241	0.08241613	0.01432621	0.02438937
1.26	3.58	0.03935200	0.03874734	0.05795872	0.05810739	0.00979636	0.01415220
1.46	3.29	0.03105962	0.02974206	0.04302786	0.04115381	0.00674690	0.00837610
1.66	3.03	0.02446888	0.02284443	0.03206992	0.02940557	0.00470167	0.00509079
1.86	2.78	0.01927948	0.01759292	0.02404359	0.02123622	0.00332105	0.00318381
2.06	2.56	0.01521006	0.01359782	0.01814582	0.01550664	0.00237822	0.00204789
2.26	2.35	0.01202175	0.01055192	0.01378659	0.01144403	0.00172540	0.00135225
2.46	2.16	0.00952135	0.00822091	0.01054147	0.00852937	0.00126684	0.00091437
2.66	1.98	0.00755640	0.00642886	0.00810738	0.00641369	0.00094017	0.00063145
2.86	1.82	0.00600820	0.00504444	0.00626787	0.00486074	0.00070435	0.00044420
3.06	1.67	0.00478484	0.00396973	0.00486767	0.00370891	0.00053200	0.00031750
3.26	1.53	0.00381535	0.00313156	0.00379470	0.00284643	0.00040463	0.00023007
3.46	1.41	0.00304490	0.00247501	0.00296741	0.00219502	0.00030955	0.00016867
3.66	1.29	0.00243102	0.00195869	0.00232600	0.00169922	0.00023794	0.00012486
3.86	1.19	0.00194075	0.00155120	0.00182624	0.00131928	0.00018357	0.00009317
4.06	1.09	0.00154841	0.00122861	0.00143518	0.00102638	0.00014200	0.00006997
4.26	1.00	0.00123392	0.00097257	0.00112804	0.00079942	0.00011004	0.00005280
4.46	0.91	0.00098152	0.00076892	0.00088608	0.00062279	0.00008533	0.00003999
4.66	0.84	0.00077879	0.00060669	0.00069501	0.00048485	0.00006616	0.00003035
4.86	0.76	0.00061591	0.00047733	0.00054386	0.00037683	0.00005123	0.00002305
5.06	0.70	0.00048506	0.00037414	0.00042418	0.00029208	0.00003957	0.00001750
5.26	0.63	0.00038005	0.00029186	0.00032938	0.00022551	0.00003045	0.00001326
5.46	0.57	0.00029590	0.00022631	0.00025434	0.00017322	0.00002333	0.00001001
5.66	0.52	0.00022863	0.00017420	0.00019501	0.00013218	0.00001775	0.00000752
5.86	0.47	0.00017502	0.00013289	0.00014822	0.00010002	0.00001340	0.00000561
6.06	0.42	0.00013249	0.00010026	0.00011146	0.00007490	0.00001001	0.00000415
6.26	0.37	0.00009894	0.00007464	0.00008272	0.00005538	0.00000739	0.00000303
6.46	0.33	0.00007266	0.00005467	0.00006040	0.00004029	0.00000537	0.00000218
6.66	0.29	0.00005228	0.00003923	0.00004323	0.00002874	0.00000382	0.00000154
6.86	0.25	0.00003666	0.00002744	0.00003016	0.00001999	0.00000265	0.00000106
7.06	0.22	0.00002488	0.00001858	0.00002037	0.00001346	0.00000178	0.00000071
7.26	0.18	0.00001617	0.00001205	0.00001318	0.00000869	0.00000115	0.00000045
7.46	0.15	0.00000992	0.00000738	0.00000805	0.00000530	0.00000070	0.00000027
7.66	0.12	0.00000561	0.00000416	0.00000453	0.00000297	0.00000039	0.00000015
7.86	0.09	0.00000279	0.00000207	0.00000225	0.00000147	0.00000019	0.00000008
8.06	0.06	0.00000113	0.00000083	0.00000090	0.00000059	0.00000008	0.00000003
8.26	0.04	0.00000029	0.00000022	0.00000024	0.00000015	0.00000002	0.00000001
8.46	0.01	0.00000002	0.00000001	0.00000001	0.00000001	0.00000000	0.00000000
C_i =		0.00455276	0.00199758	0.00154095	0.00074695	0.00008647	0.00002122
M_i =		0.21835031	0.19482106	0.26369950	0.23630123	0.03781852	0.04900938
δ_i =		-0.25016244	-0.11505272	0.06454664	0.29688094	0.40230911	0.54279698
ρ_{0i}(new) =		0.16176516	0.15760733	0.23706296	0.25558361	0.04672423	0.14125671

Table A.4
Density Profiles - Iteration 3

r (r_s)	W	ρ_1	ρ_2	ρ_3	ρ_4	ρ_5	ρ_6
0.00	5.00	0.16176516	0.15760733	0.23706296	0.25558361	0.04672423	0.14125671
0.07	4.99	0.16090790	0.15659269	0.23519959	0.25306453	0.04621002	0.13889676
0.14	4.97	0.15897577	0.15431150	0.23102222	0.24743811	0.04506387	0.13368706
0.22	4.93	0.15480887	0.14941859	0.22211868	0.23554409	0.04265183	0.12295444
0.32	4.85	0.14685425	0.14018072	0.20552273	0.21373967	0.03827012	0.10428132
0.47	4.70	0.13324293	0.12469314	0.17834971	0.17911957	0.03142933	0.07736530
0.66	4.46	0.11272204	0.10213577	0.14032503	0.13313375	0.02259914	0.04702953
0.86	4.17	0.09173728	0.08011229	0.10514678	0.09349249	0.01527880	0.02616626
1.06	3.87	0.07320253	0.06160694	0.07725809	0.06439018	0.01012959	0.01422882
1.26	3.57	0.05777725	0.04694476	0.05639195	0.04421326	0.00670870	0.00778784
1.46	3.29	0.04536066	0.03567798	0.04120207	0.03054902	0.00448441	0.00436104
1.66	3.02	0.03554622	0.02714561	0.03025689	0.02133831	0.00304063	0.00251804
1.86	2.78	0.02786026	0.02071866	0.02237556	0.01509526	0.00209513	0.00150294
2.06	2.55	0.02186502	0.01587825	0.01667483	0.01081821	0.00146714	0.00092689
2.26	2.34	0.01719230	0.01222252	0.01252185	0.00784971	0.00104319	0.00058942
2.46	2.15	0.01354644	0.00944947	0.00947120	0.00576103	0.00075215	0.00038540
2.66	1.97	0.01069567	0.00733527	0.00721091	0.00427150	0.00054908	0.00025831
2.86	1.81	0.00846057	0.00571479	0.00552200	0.00319563	0.00040523	0.00017693
3.06	1.66	0.00670301	0.00446620	0.00424992	0.00240933	0.00030189	0.00012348
3.26	1.52	0.00531689	0.00349930	0.00328465	0.00182845	0.00022671	0.00008758
3.46	1.39	0.00422059	0.00274714	0.00254724	0.00139517	0.00017138	0.00006297
3.66	1.28	0.00335125	0.00215950	0.00198048	0.00106920	0.00013026	0.00004579
3.86	1.17	0.00266029	0.00169871	0.00154254	0.00082208	0.00009942	0.00003361
4.06	1.07	0.00211003	0.00133623	0.00120258	0.00063352	0.00007612	0.00002486
4.26	0.98	0.00167112	0.00105031	0.00093763	0.00048882	0.00005839	0.00001849
4.46	0.90	0.00132064	0.00082432	0.00073049	0.00037726	0.00004482	0.00001381
4.66	0.82	0.00104060	0.00064542	0.00056813	0.00029091	0.00003440	0.00001035
4.86	0.74	0.00081682	0.00050369	0.00044066	0.00022390	0.00002636	0.00000776
5.06	0.68	0.00063810	0.00039138	0.00034049	0.00017178	0.00002015	0.00000581
5.26	0.61	0.00049552	0.00030243	0.00026175	0.00013121	0.00001533	0.00000434
5.46	0.55	0.00038202	0.00023210	0.00019993	0.00009962	0.00001160	0.00000323
5.66	0.50	0.00029192	0.00017661	0.00015146	0.00007507	0.00000872	0.00000239
5.86	0.45	0.00022069	0.00013299	0.00011359	0.00005602	0.00000649	0.00000176
6.06	0.40	0.00016467	0.00009887	0.00008413	0.00004130	0.00000477	0.00000128
6.26	0.35	0.00012092	0.00007236	0.00006136	0.00002999	0.00000346	0.00000091
6.46	0.31	0.00008706	0.00005193	0.00004389	0.00002137	0.00000246	0.00000064
6.66	0.27	0.00006114	0.00003636	0.00003064	0.00001486	0.00000171	0.00000044
6.86	0.23	0.00004161	0.00002468	0.00002074	0.00001002	0.00000115	0.00000030
7.06	0.20	0.00002718	0.00001608	0.00001347	0.00000649	0.00000074	0.00000019
7.26	0.16	0.00001680	0.00000991	0.00000828	0.00000398	0.00000045	0.00000011
7.46	0.13	0.00000960	0.00000565	0.00000471	0.00000226	0.00000026	0.00000006
7.66	0.10	0.00000488	0.00000287	0.00000239	0.00000114	0.00000013	0.00000003
7.86	0.07	0.00000204	0.00000120	0.00000099	0.00000047	0.00000005	0.00000001
8.06	0.04	0.00000058	0.00000034	0.00000028	0.00000013	0.00000002	0.00000000
8.26	0.02	0.00000005	0.00000003	0.00000002	0.00000001	0.00000000	0.00000000
C_i	=	0.00575112	0.00199868	0.00117822	0.00041631	0.00004160	0.00000656
M_i	=	0.30937545	0.22549247	0.24311587	0.16991525	0.02456246	0.02753850
δ_i	=	0.06242732	0.02426787	-0.01854883	-0.06746212	-0.08922505	-0.13309844
ρ_{0i}(new)	=	0.14696971	0.14852685	0.23315091	0.26455052	0.04951915	0.15728286

Table A.5
Density Profiles - Iteration 4

r (r_s)	W	ρ_1	ρ_2	ρ_3	ρ_4	ρ_5	ρ_6
0.00	5.00	0.14696971	0.14852685	0.23315091	0.26455052	0.04951915	0.15728286
0.07	4.99	0.14619745	0.14758527	0.23135721	0.26201131	0.04898935	0.15473541
0.14	4.97	0.14445672	0.14546790	0.22733473	0.25633728	0.04780780	0.14910697
0.22	4.93	0.14070172	0.14092424	0.21875507	0.24433018	0.04531830	0.13748985
0.32	4.85	0.13353011	0.13233779	0.20273946	0.22227237	0.04078496	0.11720079
0.47	4.70	0.12124851	0.11791785	0.17644633	0.18711501	0.03367595	0.08774985
0.66	4.46	0.10270735	0.09685613	0.13948751	0.14011187	0.02443047	0.05416089
0.86	4.17	0.08371373	0.07621584	0.10508917	0.09923608	0.01668714	0.03067794
1.06	3.87	0.06690607	0.05880283	0.07764067	0.06893770	0.01117889	0.01699349
1.26	3.57	0.05289167	0.04495086	0.05697038	0.04772825	0.00747789	0.00947090
1.46	3.29	0.04158984	0.03426569	0.04182944	0.03323116	0.00504510	0.00539503
1.66	3.03	0.03264049	0.02614443	0.03085606	0.02337397	0.00344975	0.00316463
1.86	2.78	0.02561995	0.02000653	0.02291210	0.01663922	0.00239508	0.00191612
2.06	2.55	0.02013477	0.01536943	0.01713799	0.01199169	0.00168854	0.00119699
2.26	2.34	0.01585293	0.01185720	0.01291287	0.00874481	0.00120783	0.00076993
2.46	2.15	0.01250712	0.00918600	0.00979675	0.00644672	0.00087552	0.00050855
2.66	1.97	0.00988730	0.00714451	0.00747951	0.00479912	0.00064219	0.00034392
2.86	1.81	0.00783052	0.00557625	0.00574232	0.00360337	0.00047597	0.00023744
3.06	1.66	0.00621114	0.00436538	0.00442991	0.00272567	0.00035596	0.00016688
3.26	1.52	0.00493242	0.00342592	0.00343129	0.00207474	0.00026824	0.00011909
3.46	1.40	0.00391988	0.00269373	0.00266646	0.00158748	0.00020342	0.00008610
3.66	1.28	0.00311605	0.00212074	0.00207724	0.00121970	0.00015507	0.00006293
3.86	1.17	0.00247644	0.00167071	0.00162095	0.00094007	0.00011868	0.00004640
4.06	1.07	0.00196652	0.00131615	0.00126601	0.00072610	0.00009109	0.00003446
4.26	0.98	0.00155934	0.00103606	0.00098886	0.00056149	0.00007005	0.00002573
4.46	0.90	0.00123386	0.00081436	0.00077176	0.00043427	0.00005390	0.00001929
4.66	0.82	0.00097350	0.00063860	0.00060131	0.00033559	0.00004146	0.00001449
4.86	0.75	0.00076522	0.00049916	0.00046724	0.00025883	0.00003185	0.00001090
5.06	0.68	0.00059868	0.00038851	0.00036170	0.00019900	0.00002439	0.00000819
5.26	0.62	0.00046567	0.00030076	0.00027861	0.00015234	0.00001861	0.00000614
5.46	0.56	0.00035965	0.00023126	0.00021325	0.00011594	0.00001412	0.00000459
5.66	0.50	0.00027537	0.00017635	0.00016193	0.00008757	0.00001063	0.00000341
5.86	0.45	0.00020865	0.00013311	0.00012175	0.00006552	0.00000794	0.00000251
6.06	0.40	0.00015609	0.00009922	0.00009043	0.00004845	0.00000585	0.00000183
6.26	0.36	0.00011496	0.00007284	0.00006616	0.00003530	0.00000426	0.00000132
6.46	0.31	0.00008306	0.00005246	0.00004750	0.00002525	0.00000304	0.00000093
6.66	0.27	0.00005859	0.00003690	0.00003331	0.00001764	0.00000212	0.00000064
6.86	0.23	0.00004009	0.00002518	0.00002267	0.00001197	0.00000143	0.00000043
7.06	0.20	0.00002637	0.00001652	0.00001483	0.00000781	0.00000093	0.00000028
7.26	0.16	0.00001645	0.00001028	0.00000921	0.00000483	0.00000058	0.00000017
7.46	0.13	0.00000953	0.00000594	0.00000531	0.00000278	0.00000033	0.00000010
7.66	0.10	0.00000494	0.00000308	0.00000274	0.00000143	0.00000017	0.00000005
7.86	0.07	0.00000214	0.00000133	0.00000118	0.00000062	0.00000007	0.00000002
8.06	0.05	0.00000066	0.00000041	0.00000036	0.00000019	0.00000002	0.00000001
8.26	0.02	0.00000008	0.00000005	0.00000004	0.00000002	0.00000000	0.00000000
C_i =		0.00550941	0.00202861	0.00128160	0.00049472	0.00005172	0.00000955
M_i =		0.28551865	0.21839005	0.24907549	0.18614212	0.02774819	0.03312551
δ_i =		-0.01949940	-0.00799389	0.00550997	0.02155503	0.02890147	0.04277859
ρ_{0i}(new) =		0.15149741	0.15132679	0.23435592	0.26173094	0.04864347	0.15244547

Table A.6
Density Profiles - Iteration 5

r (r_s)	W	ρ_1	ρ_2	ρ_3	ρ_4	ρ_5	ρ_6
0.00	5.00	0.15149741	0.15132679	0.23435592	0.26173094	0.04864347	0.15244547
0.07	4.99	0.15069934	0.15036305	0.23254137	0.25919875	0.04811862	0.14995319
0.14	4.97	0.14890049	0.14819600	0.22847249	0.25354121	0.04694829	0.14444807
0.22	4.93	0.14502040	0.14354636	0.21979577	0.24157270	0.04448329	0.13309187
0.32	4.85	0.13761091	0.13476205	0.20360601	0.21959949	0.03990780	0.11328098
0.47	4.70	0.12492503	0.12001730	0.17704814	0.18461705	0.03297313	0.08458417
0.66	4.46	0.10578121	0.09849917	0.13976687	0.13793780	0.02385769	0.05197081
0.86	4.17	0.08618036	0.07743490	0.10513014	0.09744942	0.01624641	0.02928110
1.06	3.87	0.06884491	0.05968527	0.07754460	0.06752359	0.01085011	0.01613070
1.26	3.57	0.05439842	0.04558216	0.05681087	0.04663467	0.00723647	0.00894171
1.46	3.29	0.04275446	0.03471558	0.04165132	0.03239583	0.00486878	0.00506768
1.66	3.03	0.03353908	0.02646530	0.03068333	0.02273911	0.00332083	0.00295865
1.86	2.78	0.02631352	0.02023611	0.02275587	0.01615698	0.00230037	0.00178376
2.06	2.55	0.02067093	0.01553439	0.01700211	0.01162458	0.00161849	0.00111003
2.26	2.34	0.01626829	0.01197629	0.01279747	0.00846434	0.00115564	0.00071156
2.46	2.15	0.01282961	0.00927234	0.00970017	0.00623152	0.00083634	0.00046857
2.66	1.97	0.01013824	0.00720733	0.00739946	0.00463326	0.00061257	0.00031603
2.86	1.81	0.00802616	0.00562209	0.00567639	0.00347500	0.00045343	0.00021767
3.06	1.66	0.00636389	0.00439889	0.00437584	0.00262592	0.00033870	0.00015266
3.26	1.52	0.00505182	0.00345042	0.00338708	0.00199696	0.00025496	0.00010874
3.46	1.40	0.00401325	0.00271163	0.00263038	0.00152665	0.00019317	0.00007849
3.66	1.28	0.00318906	0.00213378	0.00204786	0.00117202	0.00014711	0.00005727
3.86	1.17	0.00253349	0.00168017	0.00159706	0.00090263	0.00011249	0.00004217
4.06	1.07	0.00201102	0.00132295	0.00124662	0.00069668	0.00008628	0.00003128
4.26	0.98	0.00159398	0.00104090	0.00097314	0.00053836	0.00006629	0.00002333
4.46	0.90	0.00126072	0.00081775	0.00075906	0.00041609	0.00005097	0.00001747
4.66	0.82	0.00099424	0.00064094	0.00059106	0.00032132	0.00003918	0.00001311
4.86	0.75	0.00078115	0.00050072	0.00045900	0.00024765	0.00003007	0.00000985
5.06	0.68	0.00061082	0.00038950	0.00035510	0.00019028	0.00002302	0.00000740
5.26	0.61	0.00047485	0.00030133	0.00027334	0.00014555	0.00001755	0.00000554
5.46	0.56	0.00036651	0.00023155	0.00020907	0.00011068	0.00001330	0.00000413
5.66	0.50	0.00028043	0.00017644	0.00015863	0.00008353	0.00001001	0.00000307
5.86	0.45	0.00021231	0.00013307	0.00011916	0.00006245	0.00000746	0.00000226
6.06	0.40	0.00015869	0.00009910	0.00008842	0.00004613	0.00000550	0.00000164
6.26	0.35	0.00011675	0.00007267	0.00006462	0.00003357	0.00000399	0.00000118
6.46	0.31	0.00008425	0.00005227	0.00004633	0.00002398	0.00000285	0.00000083
6.66	0.27	0.00005934	0.00003671	0.00003244	0.00001673	0.00000198	0.00000057
6.86	0.23	0.00004052	0.00002500	0.00002203	0.00001132	0.00000134	0.00000038
7.06	0.20	0.00002659	0.00001636	0.00001438	0.00000737	0.00000087	0.00000025
7.26	0.16	0.00001653	0.00001015	0.00000890	0.00000455	0.00000054	0.00000015
7.46	0.13	0.00000953	0.00000584	0.00000511	0.00000260	0.00000031	0.00000009
7.66	0.10	0.00000491	0.00000300	0.00000262	0.00000133	0.00000016	0.00000004
7.86	0.07	0.00000210	0.00000128	0.00000112	0.00000057	0.00000007	0.00000002
8.06	0.04	0.00000063	0.00000038	0.00000033	0.00000017	0.00000002	0.00000001
8.26	0.02	0.00000007	0.00000004	0.00000004	0.00000002	0.00000000	0.00000000
C_i	=	0.00558967	0.00202154	0.00125012	0.00046974	0.00004845	0.00000855
M_i	=	0.29288638	0.22066538	0.24729835	0.13104541	0.02673936	0.03136513
δ_i	=	0.00580214	0.00234146	-0.00166429	-0.00637698	-0.00850596	-0.01263743

BIBLIOGRAPHY

Alcaino, G., & Liller, W. 1987, *AJ*, **94**, 372.

Alcaino, G., & Liller, W. 1982, *A&A*, **114**, 213.

Bailey, S. I. 1915, *Ann. Harvard Coll. Obs*, **76**, No. 4.

Baird, S. R. & Flower, P. J. 1987, *AJ*, **93**, 851.

Bergbusch, P. & Vandenberg, D. A., 1992, *ApJS*, **81**, 161.

Bertelli, G., Betto, R., Bressan A., Chiosi C., Nasi, E., & Vallenari A. 1990, *A&AS*, **85**, 845.

Bhatia, R. K., & Hatzidimitriou D. 1988, *MNRAS*, **230**, 215.

Bhatia, R. K., & MacGillivray, H. T., 1987, ESO Conference Workshop Proceedings No. 27, p. 485.

Bica, E., Claria, J. J., & Dottori, H. 1992, *AJ*, **103**, 1859.

Binney J. J. 1978, *MNRAS*, **183**, 501.

Binney J. J. 1980, *MNRAS*, **190**, 873.

Binney J., & Tremaine, S. 1987, in *Galactic Dynamics*, (Princeton: Princeton University Press).

Brocato E., Buonanno R., Castellani V., & Walker A. R. 1989, *ApJS*, **71**, 25.

Chiosi C., Bertelli G., Meylan G., & Ortolani S., 1989, *A&A*, **219**, 167.

Cohen, J. G., Frogel, J. A., Persson, S. E., & Elias, J. H. 1981, *ApJ*, **249**, 481.

Côté P., Welch, D. L., Mateo M., Fischer P., & Madore, B. F. 1991, *AJ*, **101**, 1681.

Côté P., Welch, D. L., Fischer P., & Irwin, M. J. 1993 in preparation.

Cudworth, K. M., & Monet, D. G. 1979, *AJ*, **84**, 744.

Da Costa, G. S., Tamblyn, P., Seitzer, P., Cohn, H., & Lugger, P. 1993 in *Dynamics of Globular Clusters*, ASP CS.

Da Costa, G. S., Freeman, K. C., Kalnajs, A. J., Rodgers, A. W., & Stapinski, T. E. 1977, *AJ*, **82**, 810.

Da Costa, G. S., Freeman, K. C. 1976, *ApJ*, **206**, 128.

de Zeeuw, T., Reijns, R., Freeman, K. C., Seitzer. P. O., & Le Poole in *The Globular Cluster - Galaxy Connection*, ASP CS.

Dickens, R. J., & Woolley, R. 1967, in *Royal Observatory Bulletin, No. 128*, London.

Djorgovski S. 1988, in *The Harlow-Shapley Symposium on Globular Cluster Systems in Galaxies (IAU Symposium No. 126)*, eds. J. E. Grindlay and A. G. Davis Philip, (Dordrecht: Reidel), p. 333.

Drukier, G. A., Fahlman, G. G., and Richer, H. B. 1992, *ApJ*, **386**, 106.

Dubath, P., Meylan, G., Mayor, M., & Magain, P. 1991, *A&A*, **239**, 142.

Elson, R. A. W., & Freeman, K. C. 1985, *ApJ*, **288**, 521.

Elson, R. A. W., Fall, S. M., & Freeman, K. C. 1987, *ApJ*, **323**, 54.

Elson, R. A. W., Fall, S. M., & Freeman, K. C. 1989, *ApJ*, **336**, 734.

Elson, R. A. W. 1991, *ApJS*, **76**, 185.

Feast, M. W. & Thackeray, A. D. 1960, *MNRAS*, **120**, 463.

Fischer, P, Welch, D. L., Côté, P., Mateo, M., & Madore, B. F. 1992a, *AJ*, **103**, 857.

Fischer, P, Welch, D. L., & Mateo, M. 1992b, *AJ*, **104**, 1086.

Fischer, P, Welch, D. L., & Mateo, M. 1993, to appear in the AJ.

Frenk, C. S. & Fall, M. F. 1982, *MNRAS*, **199**, 565.

Gebhardt, K. Pryor, C., Williams, T. B., & Hesser. J. E. 1993, in *Dynamics of Globular Clusters*, ASP CS.

Geisler, D., & Hodge, P. 1980, *ApJ*, **242**, 66.

Grabhorn, R. P., Cohn, H. N., Lugger, P. M., & Murphy, B. W. 1992, *ApJ*, **392**, 86.

Gunn, J. E. & Griffin, R. F. 1979, *AJ*, **84**, 752.

Graham, J.A. 1982, *PASP*, **94**, 244.

Grebel, E. K., Richtler, T., de Boer, K. S. 1992 presented at the Heidelberg Conference on the LMC.

Hodge, P. 1983, *ApJ*, **264**, 470.

Illingworth, G. D. 1976, *ApJ*, **204**, 73.

Inagaki, S. & Saslaw, W. C. 1985, *ApJ*, **292**, 339.

Jeans, J. H. 1916, *MNRAS*, **76**, 567.

Jedrzejewski, 1987, *MNRAS*, **226**, 747.

Jenkner, H., Lasker, B. M., Sturch, C. R., McLean, B. J., Shara, M. M., & Russell, J. L. 1990, *AJ*, **99**, 2019.

King, I. R. 1966, *AJ*, **71**, 64.

Lasker, B. M., Sturch, C. R., McLean, B. J., Russell, J. L., Jenkner, H., & Shara, M. M. 1990, *AJ*, **99**, 2019.

Lee, M. G. 1990, Ph.D. Thesis, University of Washington.

Leonard, P. J. T., Richer, H. B., & Fahlman, G. G. 1992, Los Alamos Preprint.

Lightman, A. P. & Shapiro, S. L. 1978, *Rev. Mod. Phys.*, **50**, 437.

Lupton, R. H. & Gunn, J. E. 1987, *AJ*, **93**, 1106.

Lupton, R. H., Gunn, J. E. & Griffin, R. F. 1987b, *AJ*, **93**, 1114.

Lupton, R. H., Fall, S. M., Freeman, K. C., & Elson, R. A. W. 1989, *ApJ*, **347**, 201.

Maeder, A., & Mermilliod, J. C. 1981, *A&A*, **93**, 136.

Mateo, M., Welch, D. L., & Fischer, P. 1991 in *IAU Symposium 148, The Magellanic Clouds*, (Dordrecht: Reidel), p. 191.

Mateo, M., & Schechter, P. 1989, *Proceedings of the 1ST ESO Data Analysis Workshop*, eds. P. J. Grosbol, F. Murtagh, & R. H. Warmels (European Southern Observatory: Garching).

Mateo, M. 1990, in *Physical Processes in Fragmentation and Star Formation*, eds. R. Capuzzo-Dolcetta, C. Chiosi, and A. di Fazio, (Dordrerht: Kluwer), p. 401.

Menzies, J. W., Cousins, A. W. J., Banfield, R. M., & Laing, J. D. 1989, South African Astron. Obs. Circulars, 13, 1.

Mermilliod, J.C., Meynet, G., & Maeder, A.. 1992. In Preparation.

Merritt, D. 1985, *AJ*, **90**, 1027.

Meylan, G 1987, *A&A*, **184**, 144.

Meylan, G 1988, *A&A*, **191**, 215.

Meylan, G., Dubath, P., & Mayor, M. 1991 in *IAU Symposium 148: The Magellanic Clouds*, p. 211, eds. R. Haynes and D. Milne, (Kluwer: Dordrecht).

Meylan, G. & Mayor, M. 1986, *A&A*, **166**, 122.

Meylan, G. & Mayor, M 1991, *A&A*, **250**, 113.

Michie, R. W. 1963, *MNRAS*, **126**, 499.

Mihalas, D., & Binney, J. 1981 in *Galactic Astronomy* (W. H. Freeman and Company: New York).

Miller, G. E. & Scalo, J. M. 1979, *ApJS*, **41**, 513.

Mould, J. R., & Da Costa, G. S. 1988, in *Progress and Opportunities in Southern Hemisphere Optical Astronomy*, ASP Conference Series Vol. 1, eds. V.M. Blanco and M.M. Phillips. p. 197.

Murai & Fujimoto 1980, , , .

Olszewski, E. W. 1984, *ApJ*, **284**, 108.

Olszewski, E. W., Schommer, R. A., Suntzeff, N. B., & Harris, H. C. 1991, *AJ*, **101**, 515.

Persson, S. E., Aaronson, M., Cohen, J. G., Frogel, J. A., & Matthews, K. 1983, *ApJ*, **266**, 105.

Peterson, R. C. & Latham, D. W. 1986, *ApJ*, **305**, 645.

Peterson, R. C., Seitzer, P., & Cudworth, K. M. 1989, *ApJ*, **347**, 251.

Pryor, C., McClure, R. D., Fletcher, J. M., & Hartwick, F. D. A., & Kormendy J. 1986. *AJ*, **91**, 546.

Pryor, C., McClure, R. D., Fletcher, J. M., & Hesser, J. E. 1989, *AJ*, **98**, 596.

Pryor, C., McClure, R. D., Fletcher, J. M., & Hesser, J. E. 1991, *AJ*, **102**, 1026.

Rogers, F. J. & Iglesias, C. A. 1991, *ApJS*, **79**, 507.

Russell, J. L., Lasker, B. M., McLean, B. J., Sturch, C. R., & Jenkner, H. 1990, *AJ*, **99**, 2059.

Robertson, J. W. 1974, *A&A*, **15**, 261.

Schaller,G., Schaerer, D., Meynet,G., & Maeder, A. 1992, A&AS, submitted.

Schommer R. A., & Geisler, D. 1988, in *The Harlow-Shapley Symposium on Globular Cluster Systems in Galaxies (IAU Symposium No. 126)*, eds. J. E. Grindlay and A. G. Davis Philip, (Dordrecht: Reidel), p. 577.

Schwarzschild & Bernstein 1955, , , .

Seitzer. P. O. 1983, Ph.D. Thesis, University of Virginia.

Seitzer, P. O., 1991 in *IAU Symposium 148: The Magellanic Clouds*, p. 213, eds. R. Haynes and D. Milne, (Kluwer: Dordrecht).

Spitzer, L. 1969, *ApJ*, **158**, L139.

Spitzer, L. & Hart, M. H. 1971, *ApJ*, **164**, 399.

Spitzer, L. & Thuan, T. X. 1972, *ApJ*, **175**, 31.

Stetson, P. B. 1987, *PASP*, **99**, 191.

Tifft, W.G., & Snell, C. M. 1971, *MNRAS*, **151**, 365.

Tifft, W. G., & Connoly, L. P. 1973, *MNRAS*, **163**, 93.

Tody, D. 1986 in *The IRAF Data Reduction and Analysis System, Instrumentation in Astronomy VI*, ed. D. L. Crawford, Proc. SPIE, p. 713.

Tonry, J., & Davis, M. 1979, *AJ*, **84**, 1511.

Vandenberg, D.A. 1985, *ApJS*, **58**, 711.

Welch, D. L., Mateo, M., Côté P., Fischer, P., & Madore, B. F. 1991, *AJ*, **101**, 490.

Welch, D. L., Fischer, P., & Mateo, M., 1993, in preparation.

Welch, D. L. 1992, Private Communication.

Welch, D. L., & Stetson, P. B. 1993 AJ in prep..

Wilson, O. C., & Coffeen, M. F. 1954, *ApJ*, **119**, 197.